INFORMATION TO USERS

This manuscript has been reproduced from the microfilm master. UMI films the text directly from the original or copy submitted. Thus, some thesis and dissertation copies are in typewriter face, while others may be from any type of computer printer.

The quality of this reproduction is dependent upon the quality of the copy submitted. Broken or indistinct print, colored or poor quality illustrations and photographs, print bleedthrough, substandard margins, and improper alignment can adversely affect reproduction.

In the unlikely event that the author did not send UMI a complete manuscript and there are missing pages, these will be noted. Also, if unauthorized copyright material had to be removed, a note will indicate the deletion.

Oversize materials (e.g., maps, drawings, charts) are reproduced by sectioning the original, beginning at the upper left-hand corner and continuing from left to right in equal sections with small overlaps. Each original is also photographed in one exposure and is included in reduced form at the back of the book.

Photographs included in the original manuscript have been reproduced xerographically in this copy. Higher quality 6" x 9" black and white photographic prints are available for any photographs or illustrations appearing in this copy for an additional charge. Contact UMI directly to order.

UMI

A Bell & Howell Information Company
300 North Zeeb Road, Ann Arbor MI 48106-1346 USA
313/761-4700 800/521-0600

Influences of mean shear in the Florida Current on turbulent production by internal waves

by

David Patrick Winkel

A dissertation submitted in partial fulfillment
of the requirements for the degree of

Doctor of Philosophy

University of Washington

1998

Approved by Michael C. Gregg
(Chairperson of Supervisory Committee)

Program Authorized
to Offer Degree Oceanography

Date 5 June, 1998

In presenting this dissertation in partial fulfillment of the requirements for the Doctoral degree at the University of Washington, I agree that the Library shall make its copies freely available for inspection. I further agree that extensive copying of this dissertation is allowable only for scholarly purposes, consistent with "fair use" as prescribed in the U.S. Copyright Law. Requests for copying or reproduction of this dissertation may be referred to University Microfilms, 1490 Eisenhower Place, P. O. Box 975, Ann Arbor, MI 48106, to whom the author has granted "the right to reproduce and sell (a) copies of the manuscript in microform and/or (b) printed copies of the manuscript made from microform."

Signature David R. Bikel

Date 5 June, 1998

University of Washington

Abstract

Influences of mean shear in the Florida Current on turbulent production by internal waves

by David Patrick Winkel

Chairperson of Supervisory Committee: *Professor Michael C. Gregg*
School of Oceanography

Observations of shear finestructure and turbulence in the Florida Current are analyzed to assess whether internal wave parameterizations can predict viscous dissipation rates in a vertically sheared background. Measurements by the Multi-Scale Profiler (MSP) at seven stations spanning the Straits of Florida characterize levels and patterns of internal wave activity and mixing.

Turbulent diffusivity over the section is moderate, at a decade above oceanic background levels. Strong mixing occurs within 100 m of the channel bottom, in turbulent stratified boundary layers. Weak background-level mixing occupies the high velocity core of the current. Mean shear is highest west of the core, but it is stabilized by strong stratification. Moderately strong mean shear found deep at midchannel weakens toward the surface. Fluctuating shear spectra are 1 to 4 times the oceanic reference, and typically appear anisotropic and asymmetric. Distortion of the mean shear by internal waves contributes to clockwise variance, and there are signs of near-critical reflection off the east channel wall.

By using total rather than fluctuating shear variance or spectra in existing finescale parameterizations, observed dissipation is predicted within a factor of

two for most of this dataset. This accounts for the mean shear contribution, as it supplements large-scale internal waves in setting the cutoff past which instability transfers energy toward turbulence. Overall, interactions affecting smaller waves seem to proceed at anticipated rates, regardless of how much asymmetry, anisotropy, or subinertial vs internal wave shear is present at larger scales, even for flow with squared mean Froude up to 0.5.

For regions of strong turbulence or high mean shear that are limited in extent, finescale shear variance for use in the parameterizations should be estimated spatially rather than spectrally. Spectral windows that isolate such features may yield inadequate resolution or representation of important contributions of larger-scale shear. The cutoff wavenumber corresponding to the onset of instability is then overestimated, leading to underestimated dissipation rates.

TABLE OF CONTENTS

LIST OF FIGURES

LIST OF TABLES

ACKNOWLEDGMENTS

I wish to express my gratitude to my advisor, Mike Gregg, who showed boundless patience in guiding me through to the completion of this project. Appreciation for Tom Sanford is twofold, both for his timely encouragement and for his lead of the MSP team—Jim Carlson, Bob Drever, Bill Hess, Earl Krause and Pat McKeown. Without their tireless efforts both at sea and ashore, this work would not have been possible. I thank Ren-Chieh Lien and Harvey Seim for beneficial discussions regarding internal waves and turbulence. Much assistance has come from numerous undergraduate helpers, fellow graduate students, and Ocean Physics Department staff during my journey, and I thank them all. Finally, for their support through these difficult years, I thank my close friends and family, especially my dear, sweet wife, Laurie, my greatest source of comfort.

Chapter 1

INTRODUCTION

Interactions within the internal wave field are thought to be responsible for turbulent production throughout most of the midlatitude pycnocline. Energy is introduced at near-inertial or tidal frequencies and at large to intermediate scales, and is steadily transfered toward dissipative scales. Thus, finescale shear variance can be a good indicator of turbulent dissipation, as demonstrated by *Gregg* [1989] and *Polzin et al.* [1995] with their parameterizations derived from the eikonal calculations and analytic model of *Henyey et al.* [1986].

Microstructure observations in oceanic environments with background-level internal wave spectra yield turbulent diffusivities that are ten times lower than the canonical 10^{-4} m^2 s^{-1} of *Munk* [1966]. Stronger mixing may occur in settings where internal wave variance is elevated or where energy cascades more quickly through internal wave scales. Among the mechanisms that could produce such effects are near-critical reflection off of sloping topography, generation by flow over topography, near-inertial trapping in mesoscale fronts and rings, and critical layer interactions in a vertical shear flow.

This study investigates how a subinertial background with vertical shear influences internal waves and mixing. Profile measurements from such an environment are compared with those from other oceanic settings to search for variations in the relationships between finescale shear and turbulent dissipation. Mean shear can affect mixing indirectly by altering the internal wave field, it can enhance

turbulent production by supplementing internal wave shear, or it can itself be unstable.

Because of its persistence, predictable position, and spatially varying mean shear, the Florida Current was chosen for observation. Measurements in June of 1990 spanned the Straits of Florida at 27° N, where the current transports 30 Sv northward through a channel 80-km wide and 800-m deep. The flow is fastest up near the surface and slows to nearly zero at the bottom. High mean shear occurs near the high-velocity core, which is consistently on the west side of the channel. The speed and the shear of the current diminish steadily toward the east. With the strong flow, vertical and lateral shear, and local and upstream topography, this environment for internal waves and mixing is in sharp contrast to the quiet background of the open ocean pycnocline.

Observations were made at seven stations with the freely-falling Multi-Scale Profiler (MSP), which measures simultaneously fine- and microstructure of density and horizontal velocity [*Winkel et al.*, 1996]. Previous studies have used MSP data to test an internal wave parameterization of kinetic energy dissipation [*Gregg*, 1989] and to investigate the various levels and shapes of fully resolved oceanic shear and strain spectra [*Gregg et al.*, 1993, 1996].

Analyses of these data address issues from two perspectives. First, what can be learned from this environment about oceanic internal waves and mixing in general? Second, what are the characteristics of internal waves and turbulence specific to this location?

Mean shear effects are, by design, the primary focus of this study. Is the internal wave field influenced by the background shear such that dissipation rates are enhanced? Are there variations in the level, shape or composition of internal-wave vertical wavenumber spectra that can be associated with subinertial vertical shear? Is the mean shear unstable enough anywhere to generate turbulence

directly, and is there any consistency with results from the Pacific Equatorial Undercurrent?

To characterize the turbulent nature of the Florida Current, patterns of dissipation and finescale variance are examined. How strong is mixing in this environment, and how is it distributed throughout the channel? Where is turbulent mixing driven by (a) internal wave interactions, either in isolation or under the influence of mean shear or topography, (b) instability of the background shear, (c) boundary layer processes or (d) other subinertial processes?

Chapter 2 reviews observations and understanding of mixing—in terms of turbulent diffusivities—and internal waves in the open ocean, as well as in more vigorous settings. Chapter 3 summarizes historical observations of the flow structure and hydrography of the Florida Current, then describes the subinertial environment during the MSP survey, which includes an offshore shift of the current's axis. The potential influences of this background flow and topographic setting on internal wave propagation are considered. Chapter 4 discusses MSP's measurements and data processing used in estimating the subinertial flow and in computing internal wave and mixing statistics for each station. Chapter 5 examines patterns across the channel of turbulent activity and of finescale shear, Froude and strain variance, and compares existing finescale parameterizations of dissipation to observed values. The data suggest five mixing regimes, which are further distinguished with a more focussed examination of their background, internal wave, and turbulent characteristics. Chapter 6 presents finescale spectra from the various regimes, and compares Froude spectra to a refined canonical form incorporating the internal wave scalings of dissipation. Chapter 7 examines coherences among velocity and density perturbations, and interprets their cross spectra in terms of propagating internal waves. Chapter 8 summarizes the interaction in each regime of the subinertial environment, internal waves, and

turbulent mixing. Appendix A lists notation and abbreviations used in the text. Appendix B specifies Garrett-Munk (GM76) shear, Froude and strain spectra. Appendix C examines the vertical structures of perturbations produced by internal waves propagating in a uniform shear flow, and presents the resulting current-displacement ellipses for interpreting cross spectra in Chapter 7.

Chapter 2

REVIEW OF OCEANIC MIXING AND INTERNAL WAVES

To provide context for the Florida Current survey, previous observations of turbulence and finescale variance in the ocean are summarized. Mixing is typically quantified in terms of vertical or diapycnal diffusivity, which is estimated from turbulent dissipation rates inferred from microscale measurements. To describe the background environment and the strength and content of the internal wave field, finescale measurements are made with vertical profilers, and temporal variations are sampled from moorings or through frequent profiling. Understanding of the processes driving turbulent mixing is gained by measuring the full range of scales concurrently.

2.1 Turbulent Diffusivity

Mixing is associated with the irreversible diapycnal buoyancy flux, which is parameterized by the diapycnal diffusivity

$$K_\rho = \gamma_m \frac{\varepsilon}{N^2} \qquad (\mathrm{m^2\ s^{-1}}) \tag{2.1}$$

for viscous dissipation rate ε, background stratification N^2, and mixing efficiency $\gamma_m \leq 0.2$ [*Osborn*, 1980]. The derivation of K_ρ assumes that turbulent production—from internal wave or steady mean shear—is locally balanced by

dissipation and buoyancy flux. Another approach estimates the turbulent heat flux by computing

$$K_T = \frac{\chi}{2\langle d\theta/dz\rangle^2} \qquad (\mathrm{m^2\ s^{-1}}) \tag{2.2}$$

from the diffusive dissipation rate χ and a well-defined background temperature gradient $\langle d\theta/dz\rangle$ [*Osborn and Cox*, 1972]. The dissipation method yields the eddy viscosity

$$K_m = \frac{\varepsilon}{\langle dU/dz\rangle^2} \qquad (\mathrm{m^2\ s^{-1}}) \tag{2.3}$$

for turbulence produced by a steady background shear, $\langle dU/dz\rangle$; however, this technique is not generally applicable for the ocean pycnocline, where shear comes primarily from internal waves [*Gregg*, 1987].

Throughout much of the ocean, observed K_ρ are far below the canonical 10^{-4} m^2 s^{-1} required by *Munk* [1966] for downward heat diffusion to balance advective cooling from upwelling abyssal waters. *Gregg and Sanford* [1988] detected $K_\rho = 4.3 \times 10^{-6}$ m^2 s^{-1} from MSP profiles in the midlatitude Pacific pycnocline during the Patches Experiment (PATCHEX). In the North Atlantic Tracer Release Experiment (NATRE), microscale measurements of *Schmitt et al.* [1994] yielded $K_\rho = 1.1 \times 10^{-5}$ m^2 s^{-1}, consistent with the observed spreading of tracer streaks at the site [*Ledwell et al.*, 1994].

Higher diffusivities occur as mesoscale features or topography elevate the internal wave field above the background level present during PATCHEX and NATRE. For instance, beneath a coastal jet off northern California—but well away from direct influences of topography, background shear, or atmosphere—MSP drops comprising the PATCHEX North dataset yielded $K_\rho = 3.9 \times 10^{-5}$ m^2 s^{-1}. Near the steep slope of Fieberling Guyot between 700 m and 1300 m, *Polzin et al.* [1995] found near-canonical values of $K_\rho = (6.7 - 12.4) \times 10^{-5}$ m^2 s^{-1}, ten times greater than those at similar depths further from the guyot. Stronger

topographic effects can lead to extreme values, such as $K_T = 2.5 \times 10^{-3}$ m^2 s^{-1} in the Denmark Straits [*Oakey and Elliott*, 1980] and $K_\rho = 5.5 \times 10^{-2}$ m^2 s^{-1} in the hydraulically controlled flow through the Strait of Gibraltar [*Wesson and Gregg*, 1994].

Above the core of the Equatorial Undercurrent (EUC) in the central Pacific, high mean shear often dominates turbulent production. *Peters et al.* [1988] report diffusivities from around 10^{-4} m^2 s^{-1} to over 10^{-3} m^2 s^{-1}, with high correlation of K_ρ, K_m and somewhat lower K_T. Parameterizations of diffusivities in terms of the mean Richardson number, $Ri = N^2/\langle dU/dz \rangle^2$, accounted for much of their variability, particularly in the most unstable waters where $Ri < 0.4$. However, when the same site was reoccupied over two years later, mean shear was weaker and was exceeded by internal wave shear, and dissipation rates and diffusivities were ten times lower [*Peters et al.*, 1994] and were correlated to total rather than mean shear [*Peters et al.*, 1995].

Turbulence produced by internal wave interactions is quantified by the parameterizations of *Gregg* [1989] and *Polzin et al.* [1995] ($\varepsilon_{\mathrm{iwG}}$ and $\varepsilon_{\mathrm{iwP}}$, respectively). Both predict dissipation rates that scale as $(S^2)^2 N^2$, where S^2 is the internal wave shear variance computed over an appropriate scale and N^2 is the background stratification. *Gregg* [1989] compares $\varepsilon_{\mathrm{iwG}}$ to observed ε from diverse sites—representing a factor-of-50 range in K_ρ—and finds that they agree to within a factor of 2. *Polzin et al.* [1995] estimate S^2 spectrally—a more consistent approach than the 10-m first differencing used for $\varepsilon_{\mathrm{iwG}}$—and consider dependence related to internal wave frequency content. Using measurements that comprise a wider range of N^2 and shear spectral levels than those of *Gregg* [1989], they demonstrate that dissipation does vary as $(S^2)^2 N^2$. For internal wave activity at oceanic background levels both scalings predict $K_\rho \approx 5 \times 10^{-6}$ m^2 s^{-1}.

2.2 Internal Wave Field

The content of the oceanic internal wave field is often compared to the Garrett-Munk spectrum [*Garrett and Munk*, 1972, 1975], which is based on observations collected through the early 1970's. Subsequent findings by *Cairns and Williams* [1976] regarding frequency and by *Gregg* [1977] and *Gargett et al.* [1981] regarding vertical wavenumber brought about modifications, resulting in the present GM76 form. *Gregg and Kunze* [1991] specify the GM76 vertical wavenumber spectra for horizontal velocity and vertical displacement, such that the corresponding gradient spectra of shear and strain conform to historical observations (thereby correcting an inadvertent inconsistency in the formulation of *Munk* [1981]). The GM76 spectrum represents the background state of a weakly forced pycnocline perturbed by random internal wave fluctuations. Measured spectra often deviate from GM76 near the inertial frequency, f, near N, and at tidal frequencies.

Because dissipation and mixing result from the cascade of energy through internal wave scales, the focus here is on vertical wavenumber spectra of shear and strain. The GM76 gradient spectra are fairly flat at low wavenumbers, k_3, until rolling off as k_3^{-1} past 0.1 cpm (cycles per meter). Shear spectral levels increase in proportion to the background N^2 (Appendix B); strain spectra lie a factor of 3 below the N^2-scaled shear spectra. At low wavenumbers, observed shear spectra, Φ_{Sh}, or Froude spectra, $\Phi_{\mathrm{Fr}} = \Phi_{\mathrm{Sh}}/N^2$, often exceed GM76 levels and exhibit various and irregular shapes [e.g., *Duda and Cox*, 1989; *Gregg et al.*, 1993]. However, the k_3^{-1} rolloff is observed in many spectra, sometimes beginning at wavenumbers lower than 0.1 cpm. Steeper rolloffs are also observed, particularly for data collected in the tropical Pacific [*Gregg et al.*, 1996], inside a warm ring [*Polzin et al.*, 1995], and through energetic near-inertial features [*Duda and Cox*, 1989]. As illustrated by the composite spectra of *Gregg* [1977] and *Gargett et al.*

[1981], levels flatten out or rise at higher wavenumbers owing to turbulence, until falling again at viscous or diffusive cutoffs.

Finescale shear variance is an indicator of the intensity of internal wave activity. Whether computed spectrally by integrating Φ_{Sh} or Φ_{Fr} over some wavenumber band, or spatially from smoothed and differentiated velocity profiles, the observed variance can be gauged relative to its GM76 counterpart. Further discussion of such computations is deferred to the Measurement and Data Processing chapter.

The GM76 model assumes an internal wave field that is horizontally isotropic and vertically symmetric, and whose wavenumber and frequency dependencies are separable. These assumptions break down for near-inertial frequencies, where relatively narrow-banded waves are often observed [*Leaman and Sanford*, 1976; *Duda and Cox*, 1989]. Deviations from the GM76 assumptions are expected near topography, fronts, and other mesoscale features that force or influence internal waves toward prefered orientations, scales, or frequencies.

The Florida Current is certainly an environment in which an internal wave field unlike GM76 should be expected. The current flows energetically through surrounding topography, with considerable vertical and lateral shear. The next chapter describes the subinertial background at the experiment site, emphasizing features that are relevant to internal wave activity and turbulent production. Although portions of the current are as highly sheared as the EUC, here they are stabilized by stronger stratification. More characteristic of this flow is persistent, moderately strong shear. How such a background affects internal waves and the downscale cascade to dissipation and mixing are issues addressed in subsequent chapters.

Chapter 3

SUBINERTIAL ENVIRONMENT: THE FLORIDA CURRENT

The experiment surveyed the Florida Current at 27° N, where it is confined to an 80-km wide, 800-m deep channel between Florida and Little Bahama Bank (Figure 3.1). *Leaman et al.* [1987] report a northward transport at this site of 31.7 ± 3 Sv, with peak speeds around 1.8 m s^{-1}. Most of the flow comes through the deeper passages of the Caribbean and into the Gulf of Mexico before entering the western Straits of Florida north of Cuba. Minor contributions may bypass this route, including 1.9 Sv entering between Cuba and Great Bahama Bank through Old Bahama Channel [*Atkinson et al.*, 1995] and 1.2 Sv entering just south of the survey site through Northwest Providence Channel [*Leaman et al.*, 1995]. North of the straits, the Florida Current and the Antilles Current join to form the Gulf Stream, which transports around 90 Sv as it passes Cape Hatteras near 36° N.

The measurements were collected from the *R/V Endeavor* between the 3rd and 17th of June 1990. The analyses consider data taken by MSP, which was deployed during daylight hours, from 0700 to 1900 local time (1100 to 2300 utc). Most of the 82 MSP drops were made at seven stations spanning the channel at 27° N (Table 3.1 and Figure 3.2). Profiling routinely came to within 5–15 meters of the bottom. Time between drops was 1.5 to 3 hours, depending on station depth. Supplementing the MSP data are nighttime measurements by a

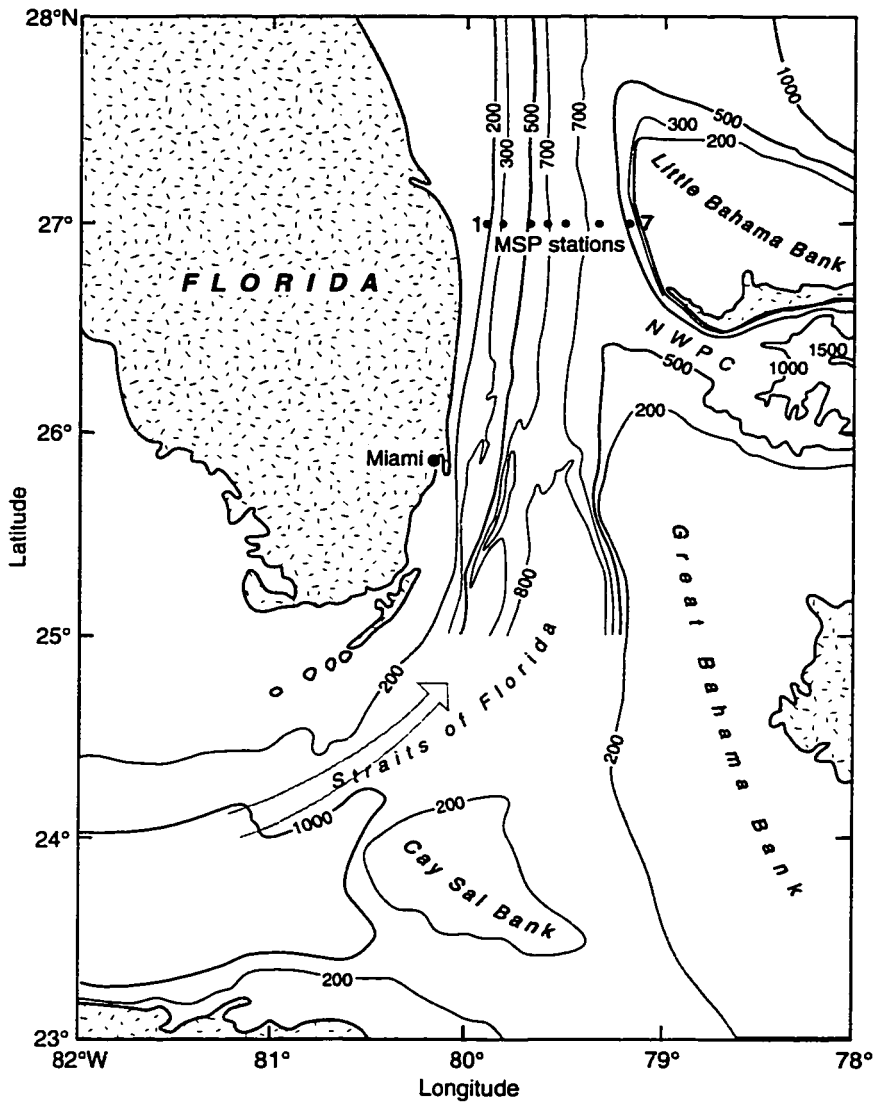

Figure 3.1: Map of Straits of Florida. Dots mark the 7 MSP stations. Channel bathymetry is shown with finer resolution north of 25°N than to the south. The three labeled banks rise steeply to depths shallower than 10 m within a few km of their 200-m contours.

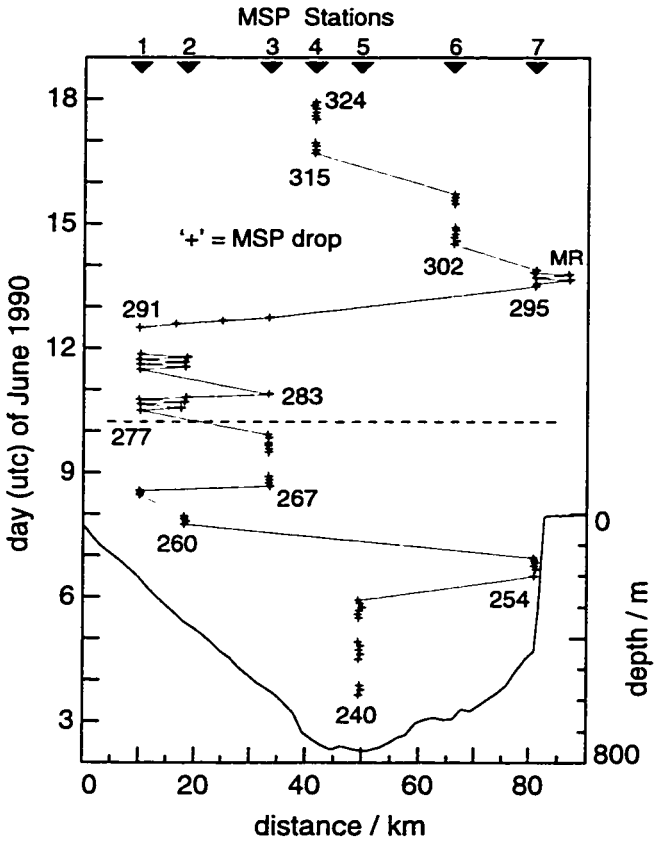

Figure 3.2: Time and location of MSP drops in the Straits of Florida along 27° N. Distance is eastward from the origin at 80° W. The start of each day (i.e., 0000 utc) is marked; local time is utc − 4 hours. A dashed line indicates when an apparent shift of the current's axis occurred, prior to drops on June 10th. Some drop numbers are shown for reference. Two drops were made near Memory Rock (MR), 8 km southeast of station 7. Channel depth is plotted atop the shading.

Table 3.1: MSP stations along 27° N. Total number of MSP drops are indicated.

Stn	Location	Depth [m]	Drops
1	79° 54′ W	202	11
2	79° 49′ W	346	10
3	79° 40′ W	562	12
4	79° 35′ W	725	10
5	79° 30′ W	762	14
6	79° 20′ W	660	10
7	79° 11′ W	440	11

SeaBird CTD and continuous velocity profiles from the vessel's RDI ADCP. Although the sampling is hardly synoptic, station mean profiles are consistent with historical observations, and will be used to illustrate the subinertial background. For contour plots of mean hydrographic fields, CTD averages at 5-km intervals are included between MSP stations.

3.1 Historical Observations

The Florida Current flows persistently through the survey site, but exhibits considerable variability in its strength and its structure. The Subtropical Atlantic Climate Studies (STACS) program employed a wide variety of measurement systems to monitor the current's heat and volume transport past this location [*Molinari*, 1985a]. Volume transport was estimated from moored current meter records [*Lee et al.*, 1985], cross-stream voltages over submarine cables [*Larsen and Sanford*, 1985], and PEGASUS dropsonde profiles [*Leaman et al.*, 1987]. All three

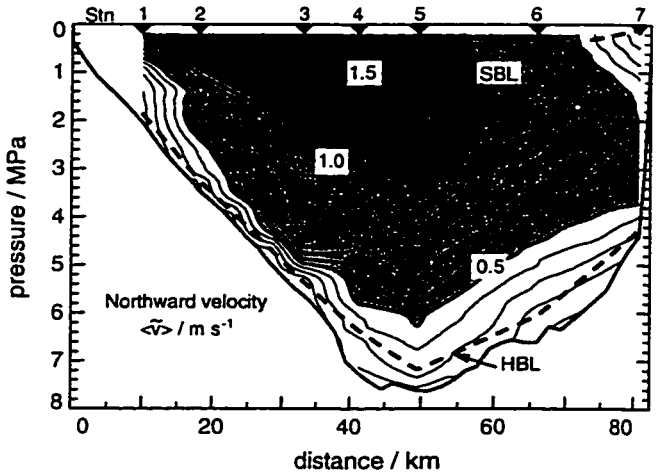

Figure 3.3: Mean northward velocity. Also indicated are maximum penetration of surface (SBL) and bottom (HBL) homogeneous layers. Note that, in subsequent figures, the 1.2-m s^{-1} isotach delineates the core of the current.

techniques yield similar results. In particular, it was noted that transport fluctuations on weekly scales are comparable to the yearly variation of 4 Sv. Velocity and temperature vary most strongly on the west side of the channel (near MSP stations 1 and 2), often in association with meandering of the current core [*Leaman et al.*, 1987].

3.1.1 Velocity structure

The high velocity core of the current is near the surface on the channel's west side, where northward speeds exceeding 1.6 m s^{-1} are attained (Figure 3.3). The velocity maximum stays near the surface to the west, but deepens eastward. Vertical shear is highest at the base of the core and on its west side. Toward the east, shear is more uniform but diminished in the deeper waters; above 150 m, its sense is negative.

The axis of the current divides anticyclonic flow on its east from cyclonic flow on its west. It runs from the center of the core down toward midchannel near

the bottom (as shown in Figure 2b of *Leaman et al.* [1987]). The lateral shear is characterized by the Rossby number, $Ro = \partial_x\langle\bar{v}\rangle/f$, where $f = 6.6 \times 10^{-5}$ s^{-1} at 27° N. The cyclonic side has the highest magnitudes, with Ro varying from 0.7 to over 1 in the upper 100 m. On the anticyclonic side Ro is negative, with magnitude diminishing from 0.5 at the surface to 0.1–0.2 at depth. By definition, $Ro = 0$ at the current axis.

3.1.2 Hydrography

Mean isotherms and isopycnals slope up toward the west (Figure 3.4), in the proper sense for thermal wind balance with the vertical shear. At a given depth, the east side of the current is warmer than the west side. A salinity maximum occurs between 100 m and 200 m (1 MPa and 2 MPa), and is saltier toward the east. Water colder than $\theta = 6$ °C or denser than $\sigma_\theta = 27.5$ kg m^{-3} seldom penetrates the Straits of Florida north of Miami.

The temperature-salinity relation varies across the channel, with relatively fresher water at a given density on the west side (Figure 3.5). *Schmitz and Richardson* [1991] find that the fresher water, including that overlying the salinity maximum, originates in the equatorial or southern Atlantic; the higher salinities are traced to subtropical water from the North Atlantic, which subducts under the southern water mass as they collide in the northern tropics before entering the deeper passages of the Caribbean. For the 12–24 °C temperature range, most of the transport originates in the North Atlantic, including a thick layer of 18 °C water. *Leaman et al.* [1995] conclude that excess 18 °C water enters through Northwest Providence Channel (NWPC) and through Santaren Channel (east of Cal Say Bank; Figure 3.1) via Old Bahama Channel, bypassing the Caribbean route argued by *Schmitz and Richardson* [1991]. Deeper, most of the water colder than 12 °C comes from the South Atlantic, with the notable freshening influence

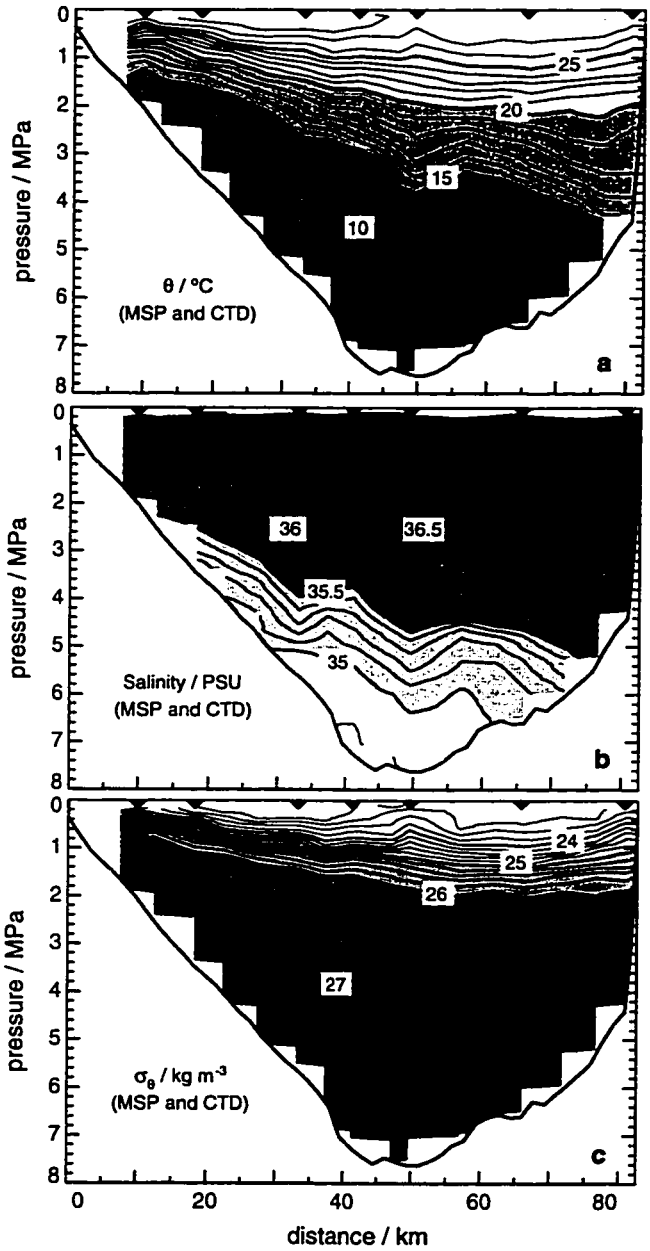

Figure 3.4: Mean hydrographic data, with regions between MSP stations supplemented by nighttime CTD data: (a) potential temperature, θ; (b) salinity; (c) potential density, σ_θ.

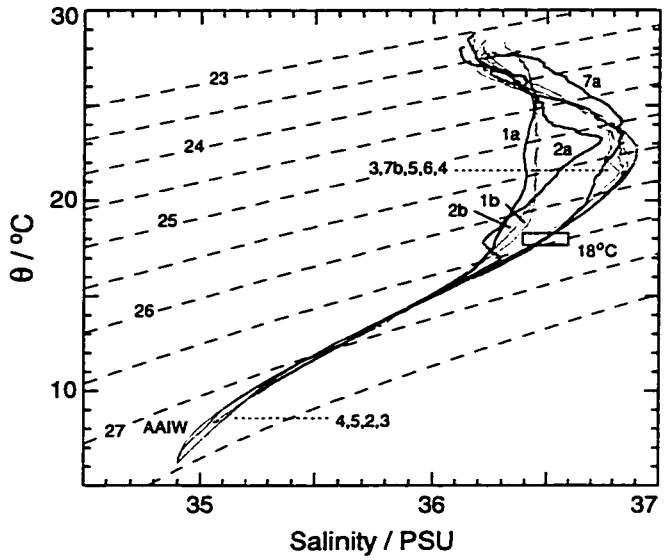

Figure 3.5: Mean $\theta - S$ relations by station. Heavier lines—labeled 1a, 2a and 7a—distinguish the first occupations of those stations (prior to June 10th) from the second ones—labeled 1b, 2b and 7b. Dotted lines connect station numbers and correspondingly ordered $\theta - S$ curves. Lines of constant σ_θ are dashed. The small box bounds North Atlantic 18° Water.

of Antarctic Intermediate Water (AAIW) in midchannel.

3.2 Topography

On the channel's west side, the bottom is smooth and even, with isobaths running essentially parallel to the northward flowing current along a gentle slope of 0.015 (Figures 3.1 and 3.2). Upstream, at the Miami Terrace 120 km to the south, the channel drops more steeply from a 350-m deep plateau to over 800 m in just 10 km. The channel shoals northward, from 800 m off Miami to 740 m at the terminus of the straits, 40 km north of the survey site. At 27° N, depths below 750 m are attained in a relatively concave section about 10-km wide. East of midchannel, the topography extends more from NWPC than from Great Bahama Bank; the bottom is bumpy and uneven as it rises from 720 m to 620 m, after which it is

fairly smooth and increasing in slope from 0.015 at 600 m to 0.025 at 500 m. The east bank rises sharply from 450 m, initially sloping up at 0.11 and reaching 0.32 toward the surface. The strait narrows from the south with the steep wall of Little Bahama Bank oriented 20° west of north, resulting in convergence in the cross-channel flow [*Leaman et al.*, 1987].

3.3 Conditions During MSP Survey

The subinertial background specific to this study, as extracted from the MSP profiles, exhibits features not evident in the historical observations. Some of this is due to the finer vertical resolution than in previous measurements, but mostly it relates to the established variability of the current. Of particular relevance is an eastward shift in the current's axis that evolved throughout the occupations of the three western stations. Some aspects of the hydrography that were affected will be described before discussing the meandering.

3.3.1 Interleaving

Interleaving of the fresher western water with the saltier midchannel water is evident near the salinity maximum, between 1 MPa and 1.5 MPa, in many drops at stations 2 and 3. Centered about local minima in salinity profiles are layers 5-m to 20-m thick, which appear in $\theta-S$ plots between the characteristic western and central-to-eastern water masses (as for station 2a in Figure 3.5). Weaker intermingling is found above 1 MPa at all stations. Well below the salinity maximum, intrusions of slightly saltier water occur at various depths in drops of stations 3 through 5. The deepest of these involve Antarctic Intermediate Water as the fresher water mass, especially at station 5.

3.3.2 Boundary layers

Homogeneous or minimally stratified boundary layers extend down from near the surface in all drops. The maximum penetration varies with station (and drop) from 10 m to 55 m (Figure 3.3). Data from these layers are excluded from much of the subsequent analyses.

Bottom homogeneous boundary layers (HBLs) are found in many drops, but not all. Because MSP profiles stop 5 m to 15 m above the bottom, the thicknesses of these layers—and whether they extend entirely to the bottom—are unknown. At a given station, the pressure at the top of a HBL does vary from drop to drop, and the shallowest encounter is indicated on Figure 3.3. At stations 1 and 7, little if any HBL is apparent, as stratification reaches the bottom of all but a few drops. Station 2 has HBLs in some drops, but they seem thinner than those at stations 3 through 5; the thickest, at over 60 m, occur at station 4.

A CTD survey during the experiment reveals a benthic front between stations 2 and 3, where the density of the HBL jumps abruptly by 0.2 kg m^{-3} [*Seim et al.*, 1998]. The downslope jump in HBL density and thickness is suggestive of model results of *Seim and Gawarkiewicz* [1997], in which a barotropically forced flow passes through a channel with a sloping sidewall. The modeled front occurs where denser water carried upslope by a bottom Ekman layer meets lighter water of a shallower arrested boundary layer regime. Above the denser HBL, return flow toward midchannel completes a secondary circulation cell (in the model).

Atop many of the observed HBLs are turbulent layers or interfaces, which are typically more stratified and sheared than the water above (and below). These turbulent stratified boundary layers (TSBLs) account for much of the mixing in the channel, as will be demonstrated later. The strongest occur at station 3 within the deep shear region evident on Figure 3.3, and at station 7 at the base

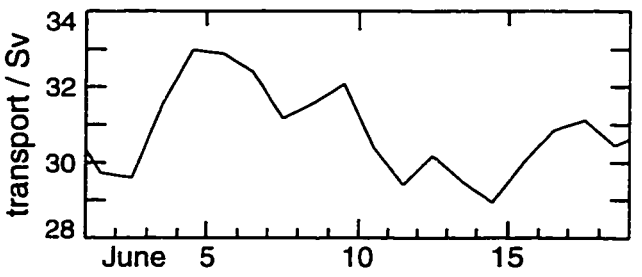

Figure 3.6: Transports inferred from voltages across the Jupiter-Settlement Point submarine cable for June 1–19, 1990 (courtesy J. Larsen).

of the east channel wall.

3.3.3 Shift of current axis

Midway through the MSP cruise, from June 9th to June 11th, the current underwent a 2-Sv drop in transport while its core moved 10 km east toward midchannel. According to submarine cable monitoring, transport averaged around 32 Sv just before the shift and 30 Sv just after (Figure 3.6). Transects made while approaching or departing the three western MSP stations yield ADCP profiles that show the position of the stream and the surrounding velocity structure (Figure 3.7). Focussing on the 1.5-m s^{-1} velocity contour, within which the flow is relatively plug-like, one can see that the core is near station 2 on June 7th, and has moved east of station 3 by June 11th. Between these dates, variations are evident in the shear structure at and below the base of the core.

The evolving subinertial flow complicates the separation of data from the western stations into background and internal wave components. Forming two sets of mean profiles for stations 1 and 2—one for drops before June 10th and another for those on or after June 10th (Figure 3.2)—removes much of the variability. Most dramatic is the change in northward velocity at station 2 (Figure 3.8); although

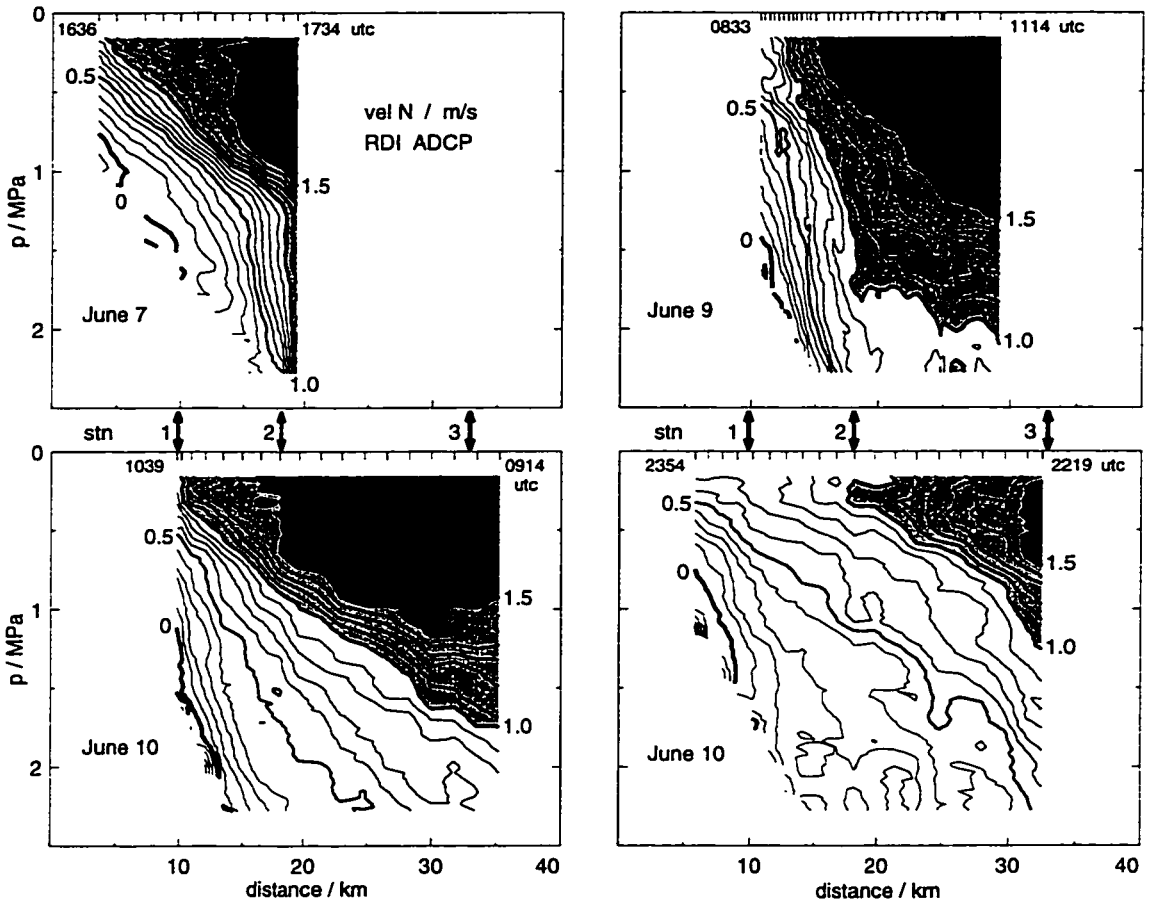

Figure 3.7: Cross-channel structure of northward velocity from RDI ADCP transects, nominally along 27° N. Bottom tracking was used to form absolute velocities. Indicated near the top of each panel are transect stop and start times and the profile locations (5-minute averages). MSP stations are marked.

the flow was still evolving during the second occupation, the profiles are much more similar to one another than to those of the first occupation. Regarding station 3, the two drops made after June 10th—and nearly two days apart—provide a contrast to the earlier drops, but are not suitable for forming mean profiles. In those two drops, the deep shear and TSBL found in the earlier ten drops are absent.

Changes in density profiles and $\theta - S$ relations are consistent with the eastward shift. Over most of the water column at stations 1 through 3, later profiles (individual or mean) are denser at a given depth than earlier profiles, as if the background structure has translated offshore. The later $\theta - S$ relation for station 2 conforms to that characteristic of the west Florida Current [*Schmitz and Richardson*, 1991], whereas the earlier drops exhibited considerable interleaving with the saltier midchannel waters (Figure 3.5). After June 10th, such interleaving is found at station 3 where $\theta - S$ curves from both of the later drops zigzag between the western fresh and the central salty characteristics.

Conditions also changed at eastern station 7 in the week between its two occupations. Mean density and velocity profiles differ, and water fresher near the surface and saltier at middepth is found the second time around. As will be shown later, mixing and internal wave activity above this station's TSBL are much stronger after June 10th. There is no evidence to establish whether these changes are directly linked to the shift in the current, or instead to unrelated variability near Little Bahama Bank [see *Leaman and Molinari*, 1987].

3.4 Interactions with Internal Waves

The Florida Current presents an extreme environment for internal waves. Propagation is influenced by strong vertical and horizontal subinertial shear, and by

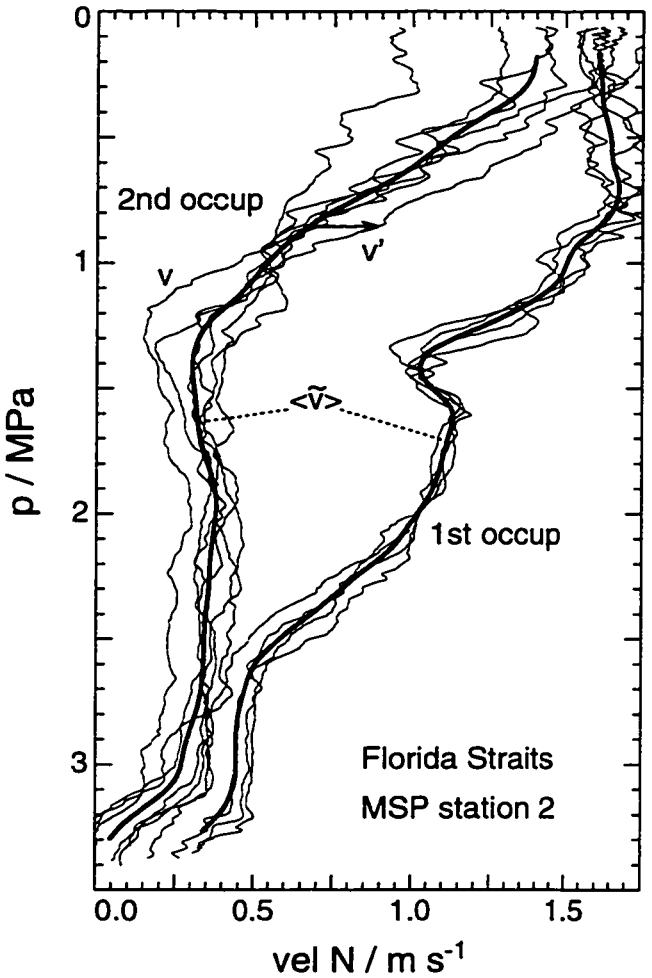

Figure 3.8: Northward velocity at station 2. Heavy lines are mean profiles, $\langle\tilde{v}\rangle$, and light lines are drop profiles, v. One mean is computed for drops of June 7th, the other for drops of June 10th and 11th. Fluctuation velocity, $v' = v - \langle\tilde{v}\rangle$, is indicated.

sloping sidewalls. Generation or scattering can occur off topography, and from fluctuations and instabilities of the energetic flow. Furthermore, internal waves can distort the background velocity and density fields to produce finescale perturbations.

To anticipate interactions with the subinertial flow, results from WKB theory will be reviewed. Effects on propagating wave packets are considered, where a packet is a localized disturbance with a dominant frequency and wavenumber; a packet propagates through the water according to its group velocity. Although the current varies with small scales and large amplitudes that violate WKB assumptions, the exercise provides useful insight into possible internal wave behavior.

3.4.1 Vertical shear

An internal wave packet propagating in a vertical shear may encounter a critical level, where its intrinsic frequency is Doppler shifted to the lower limit, f [*Jones*, 1967]. In the northward Florida Current, this may occur for wave packets propagating into the flow and down (upward phase) or with the flow and up (downward phase). Approaching a critical level from above (below), the wave's vertical wavelength shrinks and, by conservation of wave action, its shear increases; the clockwise (anticlockwise) rotation with depth of its horizontal velocity vector becomes more circular owing to the diminishing intrinsic frequency. Ultimately, the growing shear should cause a breakdown into turbulence before the packet stalls at the critical level [*Booker and Bretherton*, 1967].

Turning levels are possible for packets propagating opposite of those above, that is, with the flow and down or against it and up. In such cases, the Doppler shift is toward the upper limit, N. The wave turns around (reflects) as its vertical wavenumber—and thus, group velocity—changes sign. A similar effect occurs when a wave propagates in a still background down into weaker stratification

where its frequency exceeds N [*Desaubies*, 1973]. Near the turning depth, the solution takes the form of an Airy function.

An internal wave propagating across the channel, normal to the flow, is not affected by northward vertical shear. However, superimposed on the wave's along-channel (minor axis) velocity are perturbations caused by the wave's straining of the background flow. This kinematic effect, discussed in a later chapter and Appendix C, can lead to instability by locally enhancing the finescale shear.

3.4.2 Lateral shear

The lateral shear in the Florida Current leads to variation of the effective inertial frequency, $f_{\text{eff}} = f(1 + Ro/2)$, the lower limit for internal waves [*Kunze*, 1985]. Near-inertial waves propagating across such a background can be horizontally reflected (i.e., turned) as they approach regions of higher f_{eff} where the wave would be subinertial. Thus, waves from the anticyclonic (east) side of the channel may be repelled as they approach the current's axis, while those from the cyclonic (west) side are free to propagate to the eastern wall. The largest increases in f_{eff} are encountered by waves travelling toward the core from the eastern shallow anticyclonic zone, and by waves from the core attempting to penetrate the highly cyclonic region to its west. *Lee and Eriksen* [1997] analyze how such reflected waves alter spatial coherences in the horizontal, for comparison with observations at a subtropical front.

A near-inertial wave may reach a critical level if it propagates down (or up) to depths of higher f_{eff} [*Kunze*, 1985]; instead of the wave being Doppler shifted toward f, the background f_{eff} approaches the wave's intrinsic frequency. *Kunze et al.* [1995] detect such occurrences near the base of a warm-core ring, but involving radially-trapped rather than freely propagating waves. Waves originating in the anticyclonic region east of the Florida Current's core encounter increasing

f_{eff} as they propagate into deeper water, regardless of their orientation to the flow. Overall, however, vertical shear is the more likely agent for critical levels in this environment.

3.4.3 Topography

Flow over irregular topography can generate internal waves with phase propagation downward and opposing the current. For a flow of uniform speed and stratification, U and N, and bathymetric undulations of horizontal wavenumber k_{bot}, waves of flow-relative frequency $\omega = Uk_{\text{bot}}$ and horizontal phase speed $c = -\omega/k_{\text{bot}} = -U$ result. Energy propagation requires $f < \omega < N$, which occurs only if $f/U < k_{\text{bot}} < N/U$; disturbances are trapped close to the bottom for $k_{\text{bot}} > N/U$ [*Gill*, 1982, Ch. 6 and 8]. The vertical wavenumber is the negative root of $m^2 = k_{\text{bot}}^2(N^2-\omega^2)/(\omega^2-f^2)$. Topography of amplitude h_0 induces horizontal velocity fluctuations of $u_0 = Uh_0m$. Although a wave's phase lines appear frozen in place relative to the ground ($U + c = 0$), its perturbations are carried downstream because the horizontal group velocity of the upward packet is less than U.

To estimate generation by the Florida Current, assume near-bottom values of $U = 0.2$ m s^{-1} and $N = 0.0045$ s^{-1}. Propagation requires $k_{\text{bot}} < 0.023$ m^{-1} (radians per meter), so topography with undulations longer than about 300 m can contribute. High resolution charts show features in midchannel 2-km to 10-km long and others upstream of station 6 around 10-km long (with h_0 between 10 m and 30 m). Frequencies between $2f$ and $10f$ are anticipated, with vertical wavelengths of 250 m to 300 m and velocity perturbations around 0.12 m s^{-1}. As a generated packet propagates up, it may be reflected back down by the background shear (if $U(z) > N/k_{\text{bot}}$ at some depth).

The Miami Terrace to the south and Little Bahama Bank on the east are

assumed to be further internal wave sources, but no quantitative estimates are offered owing to their more complex topography. Effects of a flow along a slope with topography are addressed by *Thorpe* [1992, 1996].

Reflection off of a sloping boundary redistributes internal wave shear within the vertical wavenumber spectrum. Depending on the geometry, a packet's vertical wavenumber may increase or decrease on reflection. Consider the simple case of no flow, constant N, and a sloping planar surface at angle α to the horizontal, where $0 < \alpha < \pi/2$ and slope $s = \tan\alpha$. The critical frequency, $\omega_c^2 = (N^2 s^2 + f^2)/(1+s^2)$, is such that packets with $\omega > \omega_c$ reflect vertically and those with $\omega < \omega_c$ reflect horizontally [*Eriksen*, 1982]. When a reflected packet travels nearer the slope than the incident, it attains the higher wavenumber, energy density and, therefore, shear variance. This mechanism represents an abrupt downscale transfer of variance, especially near the critical frequency. *Eriksen* [1982] shows frequency spectra intensified near ω_c, with associated current ellipses that are oriented preferentially across-slope, consistent with the expected change in wave azimuth upon reflection.

The critical frequency for the east channel wall is much higher than that for the western slope. Ignore mean flow effects and assume $N = 0.0045$ s^{-1} as before. The east wall slope of 0.11 to 0.32 implies that ω_c falls between $0.1N$ and $0.3N$, while the west slope of 0.015 yields $\omega_c = 1.4f$; east channel slopes near 0.025 have $\omega_c = 2f$. Consequently, for waves incident from midchannel, all but near-inertial waves are trapped by the west slope as they continue shoreward. Conversely, all but relatively high frequency waves bounce westward off the east wall. Downward propagating packets are intensified upon reflection off the wall, and those with $\omega > (0.1-0.3)N$ are trapped; lower frequency packets continue down, until reflecting off the lesser slopes toward midchannel.

Fluctuations observed at the survey site come from internal waves that were

influenced by conditions upstream, at distances that depend on the mean flow speed and the characteristics of a given wavepacket. For instance, high wavenumber, high frequency waves do not propagate very far in the few days that it takes for the flow to transit the Straits of Florida, and the further from any boundaries they are observed, the further downsteam was their interaction with topography.

3.4.4 Turning latitude

Near-inertial wave packets from lower latitudes are turned equatorward as they approach higher f. However, the southward group velocity of most waves is exceeded by the northward flow of the Florida Current, which carries packets into an environment where they become subinertial. Whether such waves are fated for turbulent breakdown or absorption into the background flow is unknown.

Chapter 4

MEASUREMENTS AND DATA PROCESSING

In this study, mixing and internal waves in the Florida Current are investigated using measurements from the Multi-Scale Profiler (MSP). The background hydrography and flow are estimated by station averages of individual drop profiles, and fluctuations from these mean profiles are attributed to internal wave perturbations.

The capabilities of MSP's sensor systems are summarized, with particular attention paid to the production of horizontal velocity profiles. Specifications are given regarding computation of station mean profiles, statistics, and spectra.

4.1 MSP Measured Profiles

Several sensors are carried by MSP to measure finestructure and microstructure, and to detect platform motion and position. A pressure sensor monitors MSP's depth, a magnetometer its azimuthal orientation, and a pair of accelerometers its tilt. An acoustic current meter (ACM) detects horizontal flow relative to MSP, and an electromagnetic current meter (ECM) measures the large scale structure of the ocean's horizontal velocity. A ducted and pumped pair of SeaBird sensors sample temperature and conductivity, and a FP07 glass bead thermistor extends the temperature resolution. A second FP07 thermistor focusses on temperature microstructure, and a pair of airfoil probes detect velocity microstructure. *Winkel et al.* [1996] discuss the treatment and quality of the velocity and shear measure-

ments, and *Winkel et al.* [1994] provide specifications of the sensor systems and further details of the data processing.

During the Florida Straits experiment, MSP fell at 0.31 ± 0.02 m s^{-1} and rotated once every 23 ± 2 m during its free-fall descent. Drops ended when the ballast release was triggered at a programmed pressure, or when the return from an onboard continuous acoustic transmission indicated proximity to the bottom. Profiles routinely came to within 5 m to 15 m of the bottom, judging (roughly) from telemetry pinged to the ship to track and recover MSP.

For each MSP drop, standard processing generates profiles of horizontal velocity (u and v), potential temperature (θ), salinity (S), and potential density (σ_θ) on 1-kPa pressure grids (nearly equivalent to 0.1-m depth grids). Dissipation rates (ε and χ) are estimated every 20 kPa (2 m), for data within 24-kPa windows centered at each grid point. Sample profiles—from drop 0267 at station 3—are shown in Figure 4.1.

4.1.1 Velocity

Resolution of horizontal velocity at finescales—from the channel depth down to 0.5 m—relies on the ACM owing to its low-noise data. Orthogonal components u and v are oriented east and north (x and y), that is, essentially cross- and along-channel (less so near the east side). Because the ACM detects only relative flow, the platform motion must be reproduced to yield oceanic velocity. Tilt oscillation is inferred from accelerometer data, and the vehicle's gross horizontal motion—as a point mass—is simulated with a numerical model forced by the relative flow. *Winkel et al.* [1996] describe the technique, and assess uncertainties in the measured or modeled components. Although ECM velocities are nearly insensitive to MSP's motion, they are unreliable at scales smaller than the rotation length. They are essential, however, for validating the large-scale, model-corrected ACM

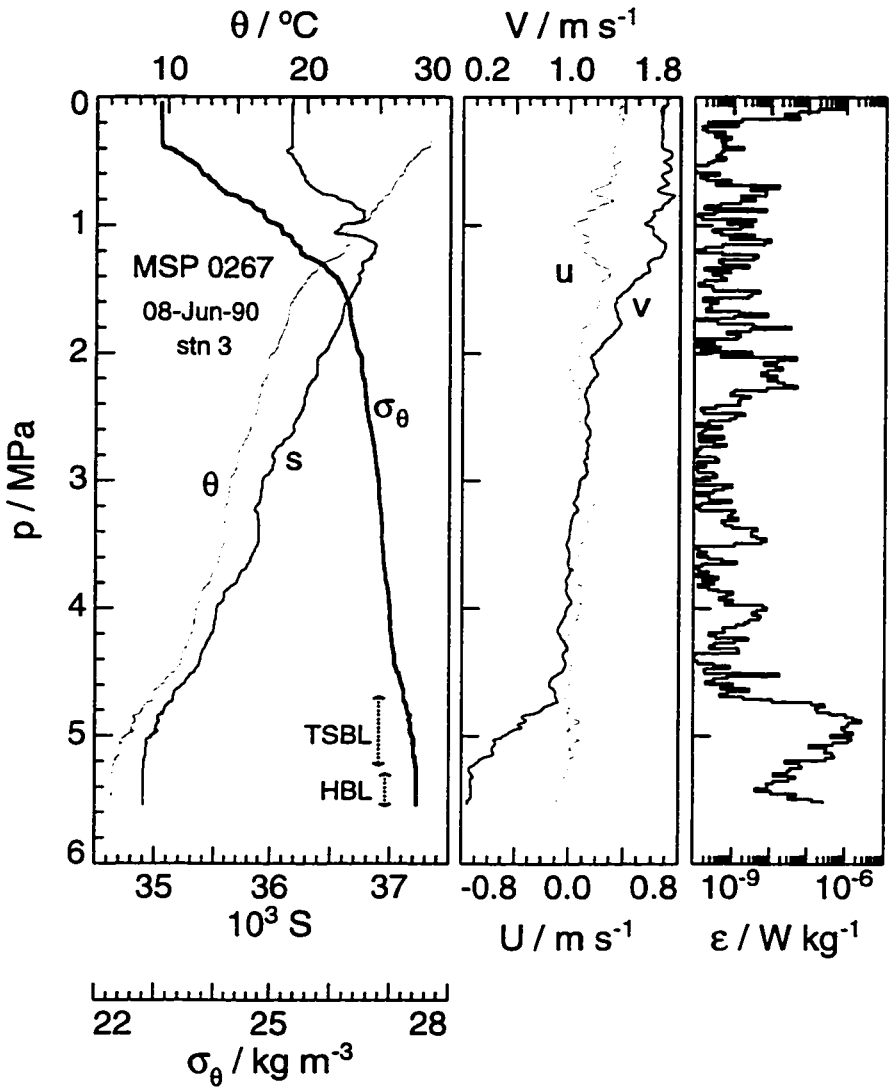

Figure 4.1: Profiles from standard processing, MSP drop 0267 at station 3. Pressure limits of the turbulent stratified boundary layer (TSBL) and the homogeneous boundary layer (HBL) are shown.

velocities.

Velocity profiles based on either ACM or ECM data contain unknown, depth-independent offsets. Through comparisons with concurrent ADCP profiles, corrected for ship motion, the offsets can be estimated to produce absolute velocities. This is most successful at stations 1, 2 and 7, where ADCP bottom tracking was reliable. At each of the other stations (3 through 6), the ship's velocity is estimated from GPS fixes for a few drops, but poor daytime GPS coverage prevents such efforts for most drops. Another option uses the ECM data to find a rough estimate of absolute velocity: MSP's rotation causes the ECM signals to oscillate with varying amplitude [*Winkel et al.*, 1996], which reaches a near-zero minimum somewhere in every Florida Straits profile. At each station, this minimal signal is assumed to correspond to a fixed water velocity—inferred from the GPS-corrected profiles—to which the uncorrected profiles are offset. Overall, absolute velocities are assumed accurate to within 0.1 to 0.2 m s^{-1}, although those relying on the ECM technique may be farther off. Some profiles come closer than 0.1 m s^{-1}, especially those corrected using bottom-tracked ADCP profiles with steady ship velocity. For mean velocity profiles, all drops at a station are included in computing the baroclinic structure, but those drops that rely on the ECM correction are excluded in estimating the absolute velocity.

Winkel et al. [1996] analyze uncertainties in the motion-corrected ACM profiles to show that they resolve shear variance and spectral levels to within 10%–15% at most scales exceeding 1 m. Uncertainties could be up to 25% at the rotation scale (23 ± 2 m) and at 5-m and 2–3-m scales.

4.1.2 Dissipation rates

Viscous dissipation rates, ε, are estimated every 0.02 MPa (2-m) by integrating shear spectra from the airfoil probes. *Winkel et al.* [1994] detail the corrections

made to raw spectra for probe and MSP circuit responses, and explain how noise contributions are avoided in the spectral integration (also, compare *Moum et al.* [1995]). Arithmetic averages of ε are taken in 0.1-MPa windows, centered every 0.1 MPa, to form drop profiles ε_{10} for further computations of diffusivities and station means.

Winkel et al. [1996] offer evidence that MSP airfoil probe spectra from warm, turbulent waters sometimes overestimate microscale shear variance by more than a factor of 2. Close examination of Florida Straits measurements reveals isolated occurrences of such amplification; while this behavior slightly influences some station statistics and spectra, it is inconsequential to ensuing analyses and conclusions. The conventional factor-of-two uncertainty in ε is seldom exceeded.

Diffusive dissipation rates, χ, are computed on a 0.02-MPa grid from microscale temperature gradient spectra, and are also averaged over 0.1-MPa intervals (χ_{10}), but they are not included in this study.

4.1.3 Interleaving and boundary layers

Drop 0267 in Figure 4.1 contains several relevant features. Homogeneous or weakly stratified boundary layers are evident below 5.25 MPa extending 25 m toward the bottom (the HBL) and from surface down to 0.4 MPa (the SBL). The turbulent stratified boundary layer (TBSL)—between 4.65 MPa and 5.20 MPa—is highly energetic, with ε sometimes exceeding 10^{-6} W kg^{-1}, strong northward shear, and locally elevated stratification. Water mass interleaving is indicated by local extrema in salinty at 1.1 MPa (minimum) and at 3.4 MPa (weak maximum); these appear as irregularities in the drop's $\theta - S$ plot.

Boundary layers are identified by visually inspecting each drop. Layer attributes (thickness, temperature, shear, dissipation, etc.) vary with station, and even from drop to drop at a given station. For analysis, data within boundary

layers are generally segregated from those of the more interior stratified waters.

4.2 Station Mean Profiles and Statistics

Finescale velocity and density profiles are assumed to represent internal wave fluctuations superimposed on a subinertial background. Because most stations were occupied for just a few days during which around 10 drops were made (Figure 3.2), simply averaging the drop profiles together does not produce an adequate representation of the background. Owing to the previously described subinertial variability, even fewer drops spanning less time are included in the separate averages—one for before June 10th and another for after June 9th—for stations 1, 2 and 7. By vertically smoothing the drop profiles before they are averaged, smaller scale fluctuations are removed from the station mean profiles.

In the following discussion of station mean profiles and statistics, angle brackets indicate time-averaged profiles (of a set of drops) and a tilde over a quantity indicates a vertically smoothed profile. These operators and other relevant quantities are described in Appendix A.

4.2.1 Density, displacement and strain

Two versions of background density profiles are computed. The first averages pressure-gridded densities to form $\langle\sigma_\theta\rangle$. For the second, the depths of specified isopycnals, $z(\sigma_\theta)$, are found for each drop, and are then averaged to form $\langle z(\sigma_\theta)\rangle$. The first is the smoother version, while the second seeks to retain finestructure that may be subinertial. Fluctuations from the mean profiles are attributed to internal wave displacements, which are estimated both linearly as $\eta_p = -\sigma'_\theta/(d\langle\sigma_\theta\rangle/dz)$ and directly as $\eta_\sigma = z(\sigma_\theta) - \langle z(\sigma_\theta)\rangle$. Isopycnal displacements η_σ are first-differenced at 10-m intervals to form strain estimates St_{10}. The

resulting station strain variances, $\langle St_{10}^2 \rangle$, tend to be similar to or smaller than those computed from linear displacements η_p.

4.2.2 Buoyancy frequency

The background stratification is estimated by averaging together drop profiles of N_{10}^2, which are computed from temperature and salinity profiles over 10-m intervals. In some cases, particularly at station 7, resulting $\langle N_{10}^2 \rangle$ profiles exhibit structures that are, perhaps, too small in scale to be part of the background. Such fluctuations are smoothed out in $\langle \widetilde{N_{10}^2} \rangle$, which is computed from drop profiles of N_{10}^2 after they are passed through a 0.125 MPa (12.5-m) boxcar filter. Relative to the unsmoothed $d\langle \sigma_\theta \rangle / dz$, the mean density gradient implied by $\langle \widetilde{N_{10}^2} \rangle$ has half as much variance in its 33-m fluctuations, and less than a tenth for those 20 m or smaller.

4.2.3 Velocity, shear and Froude numbers

The background flow is represented by $\langle \tilde{u} \rangle$ and $\langle \tilde{v} \rangle$, the time-mean of velocities smoothed with a 0.22-MPa Bartlett window (to achieve the same scale attentuation as for $\langle \widetilde{N_{10}^2} \rangle$). Smoothed drop profiles $\tilde{u}$ and $\tilde{v}$ are differentiated, then station means of these shear profiles are integrated and offset to the absolute velocities estimated from the most reliable ADCP comparisons. Fluctuations $u' = u - \langle \tilde{u} \rangle$ and $v' = v - \langle \tilde{v} \rangle$ (Figure 3.8) are first-differenced to form 10-m shear profiles S'_{10x} and S'_{10y}; similarly, total and mean 10-m shear vector components are computed from u and v and from $\langle \tilde{u} \rangle$ and $\langle \tilde{v} \rangle$. The squared magnitudes of the total and fluctuating vectors are averaged to yield station variances $\langle S_{10}^2 \rangle$ and $\langle S_{10}'^2 \rangle$, respectively. The 10-m shear vector of the mean velocity has squared amplitude $\langle \tilde{S}_{10} \rangle^2$, to which eastward as well as northward flow contributes.

Squared Froude numbers and Froude variances are computed by dividing the shear counterparts by $\langle \widetilde{N^2_{10}} \rangle$. Total and fluctuating 10-m Froude variances are denoted $\langle Fr^2_{10} \rangle$ and $\langle Fr'^2_{10} \rangle$, and the 10-m mean squared Froude number is $\langle \widetilde{Fr}_{10} \rangle^2$.

4.2.4 GM76 variances

For comparison with measured 10-m strain and shear variances, GM76 spectra are multiplied by the transform of a 10-m boxcar filter, and then are integrated to yield $St^2_{10_{GM}}=0.11$, $S^2_{10_{GM}}=0.33\langle \widetilde{N^2_{10}} \rangle$, and $Fr^2_{10_{GM}}=0.33$ (Appendix B).

4.2.5 Diffusivity

For each drop, diapycnal diffusivities are computed at 0.1-MPa intervals as $K_\rho = 0.2\varepsilon_{10}/\langle N^2_{10} \rangle$. Thus, station mean profiles are $\langle K_\rho \rangle = 0.2\langle \varepsilon_{10} \rangle / \langle N^2_{10} \rangle$. These estimates are altered only slightly (generally, by 15% or less) when computed with the smoother $\langle \widetilde{N^2_{10}} \rangle$; a notable exception occurs near 2.2 MPa in the later drops of station 7, where $\langle \widetilde{N^2_{10}} \rangle$ reduces the extreme $\langle K_\rho \rangle = 5.9 \times 10^{-4}$ m^2 s^{-1} by 75%.

4.3 Finescale Spectra

Power spectra are computed for total velocity from u and v, for fluctuating velocity from u' and v', and for vertical displacement from η_σ (and from η_p for comparison). Data within selected pressure bounds are pre-whitened by first differencing, Fourier transforms are computed for records of thickness Δz, and the resulting spectra are re-colored. Individual drop spectra are ensemble averaged to form station spectra. Spectral units are given in terms of cycles per meter (cpm), including the vertical wavenumber k_3. Spectral estimates occur at positive multiples of the fundamental wavenumber $\Delta k_3 = 1/\Delta z$.

Velocity and displacement spectra are multiplied by $(2\pi k_3)^2$ to produce shear spectra, $\Phi_{\rm Sh}$, and strain spectra, $\Phi_{\rm St}$. Because density-based $\Phi_{\rm St}$ are affected by sensor response and noise past 0.2 cpm or so, the thermistor-based form $\Phi_{\rm TG}/\langle d\theta/dz\rangle^2$ may better represent strain variance between 0.2 cpm and 1 cpm. Froude spectra are computed as $\Phi_{\rm Fr} = \Phi_{\rm Sh}/\overline{\langle N_{10}^2\rangle}$, where the vertical average $\overline{\langle N_{10}^2\rangle}$ reflects the mean stratification over the interval. Shear and Froude spectra combine autospectra of Cartesian components (east and north) or of rotary components (clockwise and anticlockwise) viewed from above in the oceanographic convention [*Gonella*, 1972]. Plotted spectra are smoothed by band averaging every two estimates from 0.11 cpm to 0.3 cpm, then four up to 0.7 cpm, and eight beyond 0.7 cpm.

Finescale variances are computed by integrating spectra over a specified wavenumber band. Froude functions $Fr'^2(k_{\rm up})$ and $Fr^2(k_{\rm up})$ accumulate, respectively, fluctuating and total spectral variance for all $k_3 \le k_{\rm up}$. Specifically, given partial sums to $k_{\rm up} = (N+\frac{1}{2})\Delta k_3$ for each $N > 0$ of $Fr'^2(k_{\rm up}) = \sum_{i=1}^{N} \Phi_{\rm Fr}(i\Delta k_3)\Delta k_3$, interpolation yields variances at other wavenumbers (down to the lower limit of $Fr'^2(\Delta k_3/2) = 0$). For the dissipation scaling $\varepsilon_{\rm iwP}$ of *Polzin et al.* [1995], the cutoff k_c is found such that $Fr'^2(k_c) = 0.7$ (corresponding to the 0.1-cpm cutoff of GM76).

Cross spectra of u and v provide coherence and phase relations as well as spectral levels. Such relations are also computed between velocity components and displacement to analyze the consistency of the fluctuations with internal wave perturbations. Results vary somewhat with use of u' and v' rather than u and v, and with the version—η_σ, η_p, or unfiltered σ_θ—of displacement selected. Cross spectra of strain and Froude components are computed from numerically differentiated displacement and velocity profiles, with shear components normalized by either $\widetilde{\langle N_{10}^2\rangle}^{1/2}$ at each grid point or by $(\overline{\langle N_{10}^2\rangle})^{1/2}$ over an entire interval.

4.4 Comments

The separation of internal wave perturbations from the subinertial background in this dataset is problematic. Fluctuations attributed to internal waves may actually be manifestations of the varying background, particularly at the western stations; conversely, structures attributed to the background may actually be aliased large-scale internal waves, particularly for cross-stream shear. Scales smaller than 20–30 m—excluded from the background by smoothing—may contain subinertial as well as internal wave contributions. Conclusions involving finescale shear and strain are tempered by their inherent uncertainties.

Cross-channel patterns of turbulent activity and finescale variance are illustrated by contouring mean profiles from the seven MSP stations. For stations 1, 2 and 7, paired mean profiles are averaged together—weighted by the number of drops included—to form a single profile for plotting. West of station 5, the interpolation scheme induces inter-station contours to follow closer to the sloping isopycnals than to the flatter isobars.

Chapter 5

PATTERNS OF TURBULENCE AND FINESCALE VARIANCE

Turbulent mixing in the Florida Current is represented by vertical diffusivities computed from MSP measurements of dissipation and stratification. Distributions of the relevant quantities are presented by contouring their station average profiles across the channel. General tendencies are noted, and areas of exceptionally strong or weak activity are emphasized. Patterns of turbulence are compared to those of finescale shear components to understand which processes are at work. Contributions could come from instability of the background subinertial flow, interactions within the internal wave field, interactions of internal waves with the subinertial flow, and boundary layer or topographic effects.

Over much of the section, mixing seems to be driven by the internal wave field, based on the similarity of observed dissipation rates with those predicted by the scalings of *Gregg* [1989] and *Polzin et al.* [1995]. West of the core, the maximal mean shear is stabilized by high stratification, but it does influence turbulent production. Topography appears to affect internal waves and enhance mixing at the easternmost station. Diffusivities are highest near the channel bottom and lowest in the core of the current.

5.1 *Vertical Diffusivity and Turbulent Dissipation*

Averaged over all MSP stations, $K_\rho = 6.7 \times 10^{-5}$ m^2 s^{-1}, including turbulent stratified boundary layers (TSBLs) near the bottom, and avoiding homogeneous boundary layers at the surface and bottom. Such diffusivity implies moderate but not strong mixing by oceanic standards. It is decade above that expected for the quiet midlatitude pycnocline with GM76-level internal waves, and a factor of 5 above the background $K_\rho = (1 - 2) \times 10^{-5}$ m^2 s^{-1} observed in the North Atlantic [*Schmitt et al.*, 1994; *Ledwell et al.*, 1994].

Turbulence is not distributed uniformly across the MSP section. Most of the high diffusivities occur in the TSBLs, which occupy only 7% of the total record; their average $K_\rho = 4.2 \times 10^{-4}$ m^2 s^{-1} is ten times the average in the remainder of the stratified water. Further variability is revealed in cross-sectional contour plots.

The highest diffusivities, $\langle K_\rho \rangle > 10^{-4}$ m^2 s^{-1}, are mainly within 100 m of the channel bottom, but are also scattered at lesser depths (Figure 5.1a). They are associated with intervals of elevated dissipation, $\langle \varepsilon_{10} \rangle > 10^{-8}$ W kg^{-1}, found below 2 MPa within moderate stratification of $\langle N^2_{10} \rangle < 10^{-4}$ s^{-2} (Figures 5.1b,c). Similar high $\langle \varepsilon_{10} \rangle$ occur in the upper 2 MPa outside the current core, but result in $\langle K_\rho \rangle$ of only $(1 - 10) \times 10^{-5}$ m^2 s^{-1} owing to the stronger $\langle N^2_{10} \rangle > 10^{-4}$ s^{-2}. Lower $\langle \varepsilon_{10} \rangle$ inside the current core at stations 3 and 4 yield minimal diffusivities of $(0.7 - 7) \times 10^{-6}$ m^2 s^{-1}. Elsewhere, at intermediate depths, weak-to-moderate $\langle K_\rho \rangle$ of $(0.4 - 10) \times 10^{-5}$ m^2 s^{-1} tend to follow patterns of $\langle \varepsilon_{10} \rangle$, which range from 5×10^{-10} W kg^{-1} up to 10^{-8} W kg^{-1}.

The high $\langle K_\rho \rangle$ and $\langle \varepsilon_{10} \rangle$ near the bottom reflect the influence of TSBLs, which vary in character and thickness with station and from drop to drop. Some lie atop homogeneous bottom boundary layers (HBLs), others extend at least to

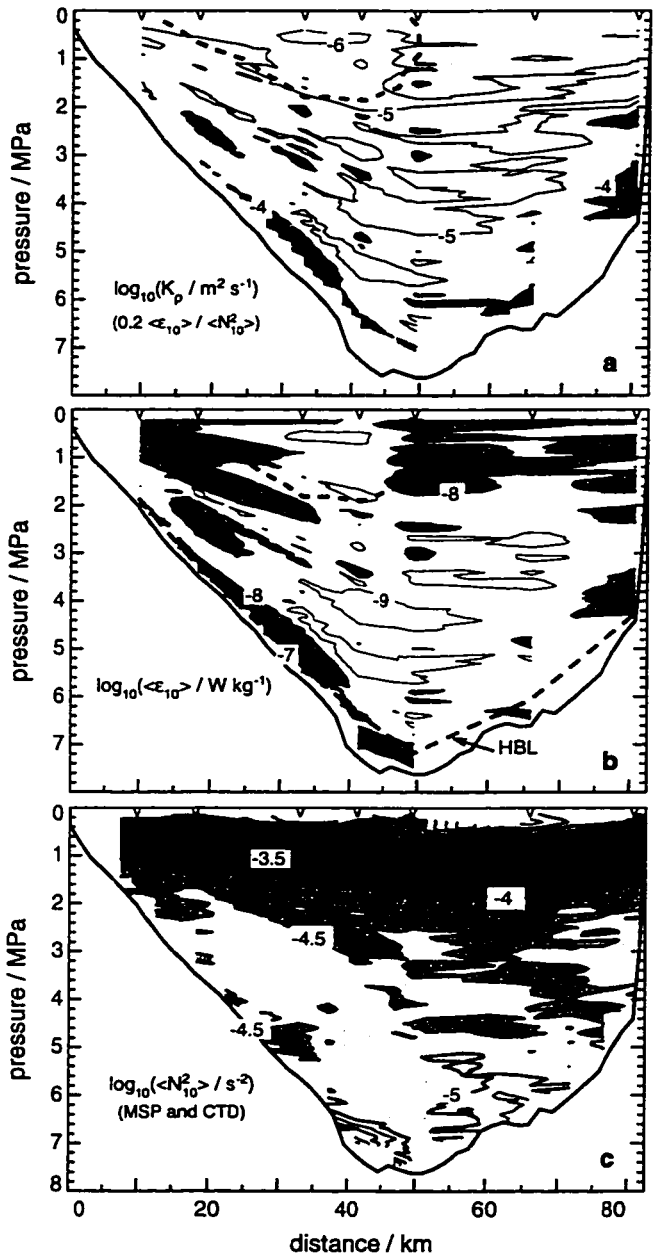

Figure 5.1: Patterns of mixing and stratification, from station mean profiles gridded at 0.1-MPa intervals: (a) diffusivity $\langle K_\rho \rangle$, homogeneous boundary layers excluded; (b) dissipation $\langle \varepsilon_{10} \rangle$; (c) squared buoyancy frequency $\langle N_{10}^2 \rangle$. Shades darken at half-decade ($10^{1/2}$) intervals. The current core and its western high shear region are represented by the dashed 1.2-m s^{-1} isotach.

the bottom of the drop. The strongest are marked by shear, stratification, and especially dissipation that are elevated in contrast to waters immediately above. Those of stations 3 and 7 are 30–70 m thick, such as the vigorous example shown in Figure 4.1. At station 2, they appear as 2–15-m interfaces that cap mixed or weakly stratified bottom layers (i.e., where $N < 0.002$ s^{-1}); the few detected at station 1 are similar, but thinner. At stations 4 through 6, TSBLs tend to be 10–30 m thick, lying atop HBLs that are up to 60 m thick. Section maxima of $\langle \varepsilon_{10} \rangle > 10^{-7}$ W kg^{-1} occur in the HBLs of stations 4 and 5 and in the TSBL of station 3 (Figure 5.1b). For an individual drop, $\overline{K_\rho}$ is computed with layer-averaged $\bar{\varepsilon}$ and $\overline{N^2}$; a few such $\overline{K_\rho}$ exceed 10^{-3} m^2 s^{-1} for drops of stations 3, 5 and 7. These extreme values are smeared out in $\langle K_\rho \rangle$ profiles, which are computed from station averages on fixed intervals.

Note that Figure 5.1 accurately portrays mean turbulent quantities at each station, but that patterns between the widely spaced stations may be artifacts of the contouring interpolation scheme and, therefore, should be interpreted cautiously. This also applies to subsequent figures of finescale variance.

5.2 Finescale Shear and Strain

Patterns of finescale variance are examined as a necessary step in understanding the observed distribution of turbulence and mixing. The subinertial background shear, $\langle \widetilde{S}_{10} \rangle^2$, can generate turbulence directly, or it can affect the downscale transfer by altering or reinforcing the internal wave field. Internal wave levels are represented by the fluctuating shear variance, $\langle S'^2_{10} \rangle$, and its stratification-scaled counterpart, $\langle Fr'^2_{10} \rangle$. Further insight into the composition of the internal wave field comes from the strain variance, $\langle St^2_{10} \rangle$.

5.2.1 Mean shear

The highest $\langle \tilde{S}_{10} \rangle^2$, in excess of 10^{-4} s^{-2}, are found above 1.5 MPa adjacent to the west side of the current core at stations 1 and 2, and in the TSBL of station 3 (Figure 5.2a). For these regions, and also for the local maximum near 2.2 MPa at station 2, the northward component dominates the eastward. The maximum mean shears of 0.01–0.018 s^{-1} are comparable to those in the Gulf Stream off New England [*Gregg and Sanford*, 1980] and to those above and below the Equatorial Undercurrent in the Pacific [*Peters et al.*, 1995]. Lesser $\langle \tilde{S}_{10} \rangle^2$ of $(1-10)\times 10^{-5}$ s^{-2} occur deeper at stations 1 and 2, within and under the central core, and at station 7 near the surface and the bottom; in the latter two areas, the east mean component contributes significantly. A vast region of $\langle \tilde{S}_{10} \rangle^2 < 10^{-5}$ s^{-2} covers much of stations 4 through 7. Minima less than 10^{-6} s^{-2} lie half way between the core and the bottom at stations 3 and 4.

Areas of $\langle \widetilde{Fr}_{10} \rangle^2 > 0.5$ are of limited extent: the base of the shallow high $\langle \tilde{S}_{10} \rangle^2$ of stations 1 and 2, within the deeper high $\langle \tilde{S}_{10} \rangle^2$ of stations 2 and 3, deep at stations 4 and 6, and immediately below the central core (Figure 5.3a). Maxima exceeding 1 occupy TSBLs at stations 3 and 4. Moderate $\langle \widetilde{Fr}_{10} \rangle^2$ of 0.2 to 0.5 occur over most of stations 1 and 2 (throughout much of the upper high shear zone), in the lower 100 to 200 m of stations 4 through 7, and at middepths of stations 3 and 4. Most of the upper waters of the three easternmost stations—and the highly stratified core—have $\langle \widetilde{Fr}_{10} \rangle^2 < 0.2$, including large areas with 0.05 or less.

5.2.2 Fluctuating shear variance

The basic pattern in Figure 5.2b is that $\langle S'^2_{10} \rangle > 3 \times 10^{-5}$ s^{-2} above 2 MPa and $\langle S'^2_{10} \rangle < 3 \times 10^{-5}$ s^{-2} below 2 MPa. Exceptions are in the TSBL of station 3

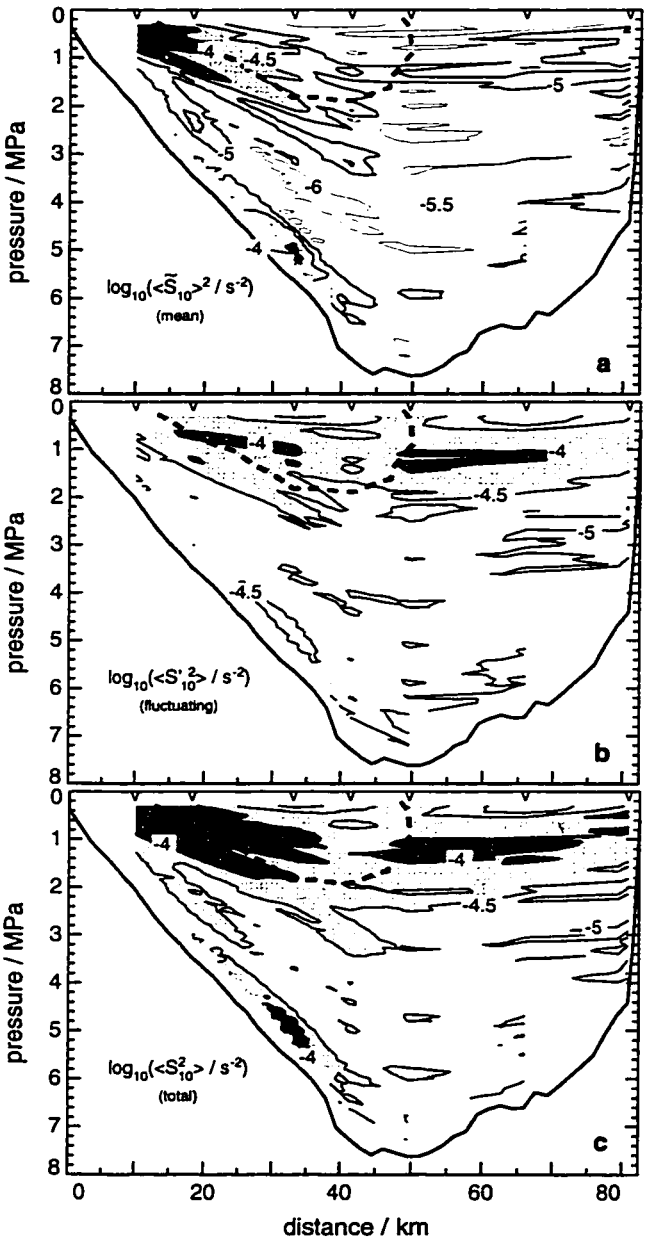

Figure 5.2: Patterns of 10-m first-differenced shear (east and north components combined): $\log_{10}$ contours of (a) mean squared $\langle \tilde{S}_{10} \rangle^2$; (b) fluctuating variance $\langle S'^2_{10} \rangle$; (c) total variance $\langle S^2_{10} \rangle$. Dashed line is 1.2-m s^{-1} isotach.

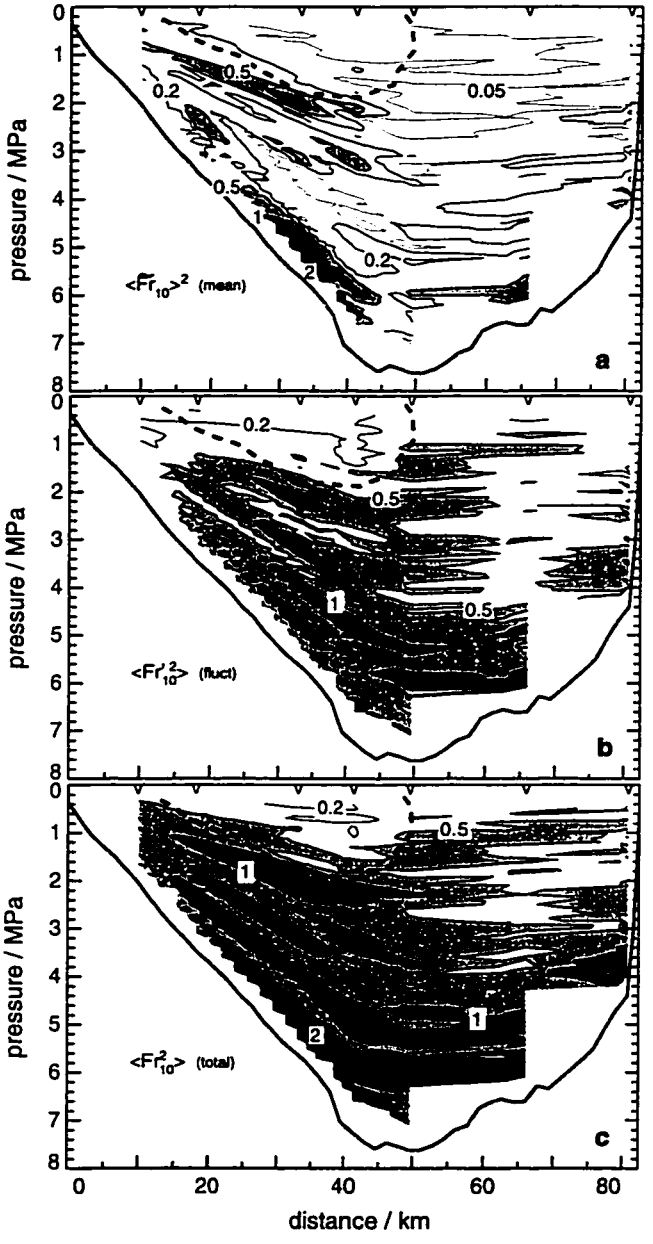

Figure 5.3: Patterns of 10-m first-differenced Froude numbers, exclusive of homogeneous boundary layers: linear contours of (a) mean squared $\langle \widetilde{Fr}_{10} \rangle^2$; (b) fluctuating variance $\langle Fr'^2_{10} \rangle$; (c) total variance $\langle Fr^2_{10} \rangle$. For GM76, $\langle Fr^2_{10} \rangle = \langle Fr'^2_{10} \rangle = 0.33$. Dashed line is 1.2-m s^{-1} isotach.

and in the core at station 4, which have $\langle S_{10}'^2 \rangle$ respectively higher and lower than those nearby. Minima of less than 10^{-5} s^{-2} occur deep at station 6 and above the TSBL of station 7. Over most of the section, $\langle S_{10}'^2 \rangle$ is at least twice the mean component; only in western station regions of $\langle \tilde{S}_{10} \rangle^2 > 3 \times 10^{-5}$ s^{-2} does the mean exceed $\langle S_{10}'^2 \rangle$.

Contouring $\langle Fr_{10}'^2 \rangle$ reveals the relative strength of the fluctuating shear by removing the dependence on mean stratification (Figure 5.3b). Maxima exceeding 1 lie beneath the core, and deep at stations 3 through 6. Moderate $\langle Fr_{10}'^2 \rangle$ of 0.5 to 1 cover most of stations 2 through 5 below 1.5–2 MPa, and the lower 100–200 m of stations 6 and 7. Weaker $\langle Fr_{10}'^2 \rangle$ of 0.2 to 0.5 occur at stations 6 and 7 away from the bottom, and within and west of the lower core. The lowest values, less than 0.2, are in the upper core, reminiscent of the minimal diffusivity there (Figure 5.1a). Note also similar middepth patterns of west-to-east weakening in $\langle Fr_{10}'^2 \rangle$ and $\langle K_\rho \rangle$.

5.2.3 Total shear variance

Patterns of total shear variance (Figure 5.2c) are similar to those of the fluctuating component, except where mean shear is high. The most notable difference is the larger expanse of $\langle S_{10}^2 \rangle > 10^{-4}$ s^{-2}, including the high-$\langle \tilde{S}_{10} \rangle^2$ regions west of the core and deep at station 3. Thick intervals of $\langle Fr_{10}^2 \rangle > 1$ appear under the core and deep at stations 2 through 7 (Figure 5.3c). Over most of the section, $0.5 < \langle Fr_{10}^2 \rangle < 1$. Minima of $\langle Fr_{10}^2 \rangle < 0.5$ occupy only the upper core and some upper waters of stations 6 and 7.

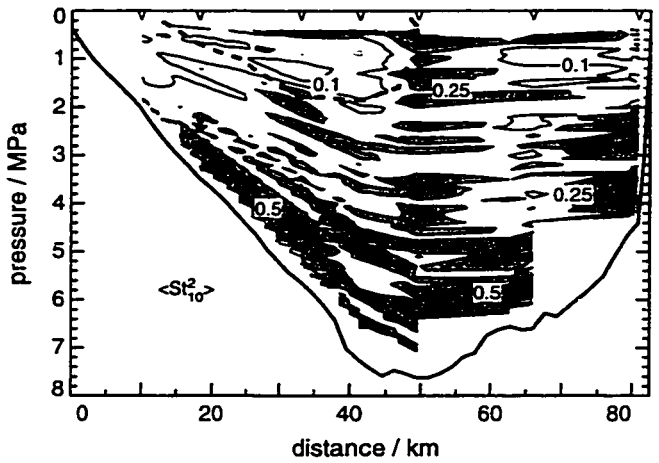

Figure 5.4: Pattern of 10-m first-differenced strain variance, based on displacements of isopycnals from their mean depths. For GM76, $\langle St_{10}^2 \rangle = 0.11$. Dashed line is 1.2-m s^{-1} isotach.

5.2.4 Strain variance

Determination of strain variance in these data is problematic, owing to uncertainty in the background density field related to subinertial variability and to lateral interleaving and intrusions. Strain estimates are most questionable in the upper 100 to 150 m of stations 1 through 3, where $\theta - S$ plots reveal considerable interleaving. Also suspect are strains from station 7, where the density finestructure is particularly steppy. The most reliable estimates are those for stations 3 through 6, below 2 MPa and above the bottom 100 m.

Patterns of strain variance are more irregular than those of $\langle Fr_{10}'^2 \rangle$ (Figure 5.4). Regions of $\langle St_{10}^2 \rangle > 0.25$ appear fairly deep at stations 2 through 7, at middepths of especially stations 5 and 7, and in the upper 200 m of station 5, with isolated maxima over 0.5 deep in midchannel, near middepth of station 7, and above 1.5 MPa at station 5. Values between 0.1 and 0.25 span the channel at intermediate depths. Minimal $\langle St_{10}^2 \rangle$ are found in the core, in the shallow zone of high mean shear, and around 1 MPa at stations 6 and 7.

5.2.5 Comparison to GM76

Fluctuating shear variance in these data is, generally, 1.5 to 3 times the GM76 counterpart of $Fr^2_{10_{GM}} = 0.33$, while strain variance is up to 4 times the GM76 value of $St^2_{10_{GM}} = 0.11$. The greatest excesses lie under the central core and deep in midchannel, although $\langle St^2_{10} \rangle$ is also high in the lower 200 m of station 7. Only in the current core are variances below GM76 levels.

The shear appears to deviate from the GM76 assumptions of vertical symmetry and horizontal isotropy. Clockwise variance is 2 to 4 times the anticlockwise component over much of the section, and is the lesser only in the upper portion of station 7 (Figure 5.5). This suggests that more energy is propagating down than up, although such an interpretation is blurred by limited knowledge of the frequency content and by influences of subinertial background shear. Cross-channel shear variance is more than twice along-channel in the upper 200 m of stations 5 and 6, and particularly at station 7 where it is up to 4 times higher. There are regions where along-channel shear variance is greater than cross-channel, but only in the TSBL of station 3 is it twice as high.

5.3 Internal Wave Scalings of Dissipation

Similarities in the patterns of $\langle K_\rho \rangle$ and $\langle Fr'^2_{10} \rangle$ suggest that dissipation rates are modulated by the strength of the internal wave field. To quantify this perceived relationship, observed ε are compared to parameterizations that extend predictions of the eikonal calculations and analytic model of *Henyey et al.* [1986] beyond Garrett-Munk conditions. Both *Gregg* [1989] and *Polzin et al.* [1995] account for deviations in low-wavenumber shear levels, and the latter also allows for variations in frequency content. Neither parameterization considers internal waves interacting within a background that includes significant subinertial shear. How-

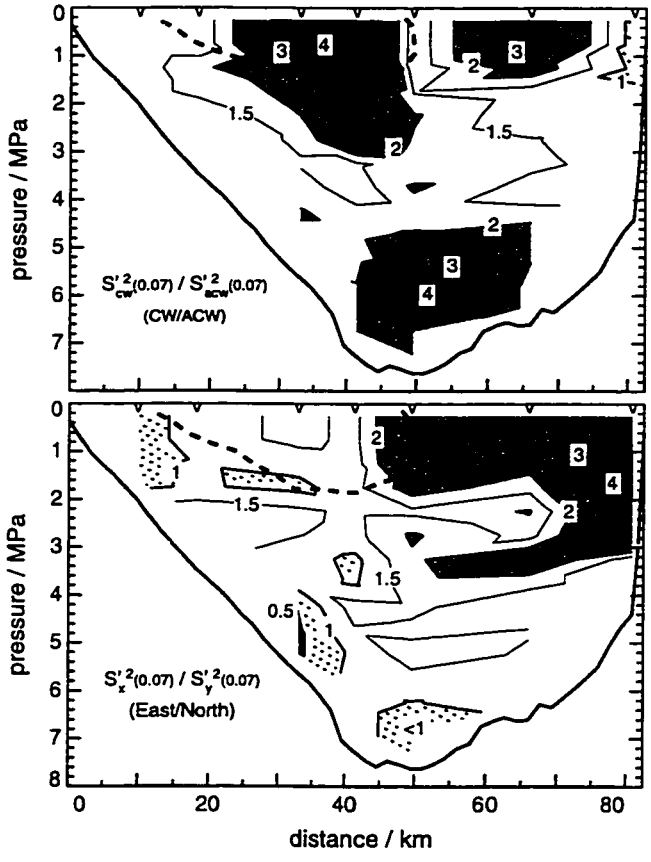

Figure 5.5: Patterns for ratios of indicated components of fluctuating shear variance, summed from 0.02 to 0.07 cpm for 1-MPa spectral windows centered every 0.5 MPa (starting at 0.75 MPa).

ever, *Polzin et al.* [1996] conclude that mean shear effects should be considered when the mean Fr^2 exceeds 0.05 (i.e., $Ri < 20$). It will be demonstrated with the Florida Straits data that the influence of mean shear on turbulent production by internal waves can be accounted for, empirically, simply by using total rather than fluctuating shear in the existing parameterizations.

5.3.1 Model formulation

The model of *Henyey et al.* [1986] equates turbulent dissipation to the downscale energy flux of internal waves—at GM levels of *Munk* [1981]—as they evolve within a background flow consisting only of larger-scale internal waves. Specifically,

$$\varepsilon(m) = \left\langle \frac{dE}{dt} \right\rangle = \left\langle \frac{dE}{dm}\frac{dm}{dt} \right\rangle = \left\langle \frac{dE}{dm} \right\rangle \left\langle \left| \frac{dm}{dt} \right| \right\rangle \frac{1 - r(m)}{1 + r(m)} \qquad (\mathrm{m^2\ s^{-3}}) \qquad (5.1)$$

is the net flux past vertical wavenumber m to higher wavenumbers. For this discussion, the angle brackets combine contributions from wave packets of various horizontal wavenumbers k_h and azimuths ϕ. Doppler shifting by the background flow induces wavenumbers to increase in some packets ($dm/dt > 0$) and to decrease in others ($dm/dt < 0$); $r(m)$ is the ratio of down-to-up-wavenumber energy flux magnitudes. The total energy density at m is

$$\left\langle \frac{dE}{dm} \right\rangle = \frac{\alpha\, \Phi_{\mathrm{Sh}}(m)}{2\, m^2} \qquad (\mathrm{m^3\ s^{-2}}) \qquad (5.2)$$

where Φ_{Sh} is the shear spectral density and α is the ratio of total energy to horizontal kinetic energy [*Polzin et al.*, 1995]. The eikonal calculations support

the form

$$\left\langle \left| \frac{dm}{dt} \right| \right\rangle = \langle S'^2(m)\, k_h^2 \cos^2\phi \rangle^{1/2} = [S'^2(m)]^{1/2}\, \frac{m}{2^{1/2}} \left\langle \frac{\omega^2 - f^2}{N^2 - \omega^2} \right\rangle^{1/2} \qquad (\mathrm{m^{-1}\ s^{-1}}) \tag{5.3}$$

for the Doppler shift term, where $S'^2(m)$ is the cumulative background shear variance up to m [*Henyey et al.*, 1986]; substitution for k_h via the dispersion relation, along with the assumption of isotropy, leads to the rightmost expression [*Polzin et al.*, 1995]. Substitution of (5.2) and (5.3) into (5.1) yields

$$\varepsilon(m) = \frac{\alpha\, \Phi_{\mathrm{Fr}}(m)\, N^3}{2.83\ m}\, [Fr'^2(m)]^{1/2} \left\langle \frac{\omega^2 - f^2}{N^2 - \omega^2} \right\rangle^{1/2} \frac{1 - r(m)}{1 + r(m)} \tag{5.4}$$

in terms of Froude spectral level and variance. *Henyey et al.* [1986] attain $\varepsilon(m)$ consistent with their eikonal results by setting $r(m) = 0.4$ while evaluating (5.4) at $m = 1.26$ rad m^{-1} (0.2 cpm) for the GM spectrum specified by *Munk* [1981].

The GM76 spectrum is such that $\alpha = \alpha_{\mathrm{GM}} = 4/3$ and

$$\left\langle \frac{\omega^2 - f^2}{N^2 - \omega^2} \right\rangle_{\mathrm{GM}}^{1/2} = \frac{f}{N} \cosh^{-1}(N/f) \tag{5.5}$$

at any m, and that $\Phi_{\mathrm{Fr}}(m) \approx 0.56$ rad^{-1} m and $Fr'^2(m) \approx 1.19$ at $m = 1.26$ rad m^{-1} (Appendix B). Substituting (5.5) into (5.4) and evaluating with these spectral values and $r(m) = 0.4$ yields

$$\varepsilon_{\mathrm{GM}} = \varepsilon_{\mathrm{GM0}}\, \frac{N^2}{N_0^2}\, \frac{f}{f_0}\, \frac{\cosh^{-1}(N/f)}{\cosh^{-1}(N_0/f_0)} \tag{5.6}$$

as the anticipated dissipation rate for GM76. The reference $\varepsilon_{\mathrm{GM0}} = 8.9 \times 10^{-10}$ W kg^{-1}, computed for $N_0 = 0.00524$ s^{-1} and $f_0 = 6.6 \times 10^{-5}$ s^{-1}, slightly exceeds that employed by the upcoming parameterizations owing, in part, to dif-

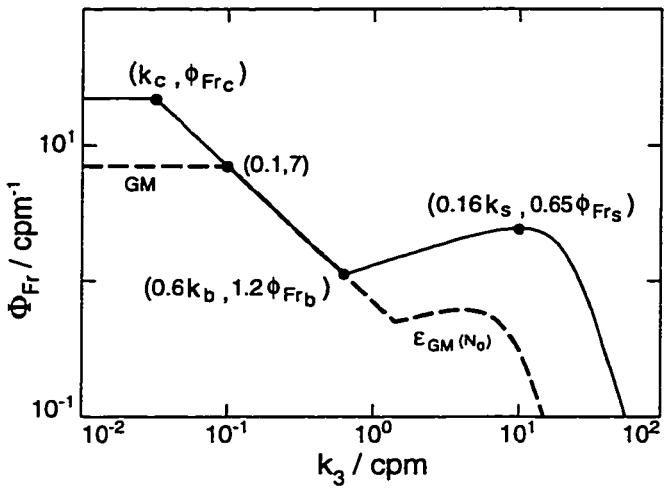

Figure 5.6: Model composite Froude spectrum. Solid line: Model corresponding to $N = 2N_0$ and $\varepsilon = 40\varepsilon_{0P} = 2.7 \times 10^{-8}$ W kg^{-1}, so that $k_c = 0.32k_{cGM}$ by (5.7) or (6.2) given $R_\omega = 3$. Labeled points delineate four spectral bands. Dashed line: Model approximation of GM76 for $N = N_0$ and, thus, $\varepsilon = \varepsilon_{0P}$. Viscous scales are computed with $\nu = 10^{-6}$ m^2 s^{-1}.

fering spectral approximations. For a spectrum in equilbrium with the modeled downscale transfer, $\varepsilon(m)$ should be independent of m, which suggests by (5.4) that $r(m)$ varies with m. Specifically, $r(0.1 \text{ cpm}) = 0.75$ and $r(0.05 \text{ cpm}) = 0.82$ for GM76.

5.3.2 Parameterizations

Both parameterizations extend the model to internal wave fields that deviate from GM76 spectral levels, but only ε_{iwP} considers non-GM76 frequency distributions. *Polzin et al.* [1995] assume Froude spectra that are constant at $\Phi_{\text{Fr}} = \phi_{\text{Frc}}$ for $k_3 \leq k_c$ and that roll off as $\Phi_{\text{Fr}} = \phi_{\text{Frc}}(k_3/k_c)^{-1}$ for $k_3 > k_c$ (their Figure 1a). With $k_c = 0.1$ cpm and $\phi_{\text{Frc}} = 7$ cpm^{-1}, this approximates the GM76 spectrum (Appendix B). It is assumed that $Fr'^2(k_c) = k_c\phi_{\text{Frc}} = 0.7$, and so all such spectra roll off along an extension of the GM76 k_3^{-1} range (Figure 5.6). This

pattern roughly describes many observed spectra, including those over much of this Florida Current survey (see the Vertical Wavenumber Spectra chapter).

Comparison to GM76 focusses on spectral attributes in the low wavenumber band up to k_c, the point at which $Fr'^2(k_c)=0.7$ in the fluctuation spectrum. To provide a more stable estimate of the spectral level, the average $\phi_{\mathrm{Fr}c} = 0.7/k_c$ is used in place of $\Phi_{\mathrm{Fr}}(k_c)$ [*Polzin et al.*, 1995]. The shear-to-strain ratio, $R_\omega = Fr'^2(k_c)/St^2(k_c)$, characterizes the frequency content near k_c, in that R_ω is also the ratio of horizontal kinetic energy to potential energy for a single wave of frequency

$$\omega_c \approx \left(\frac{R_\omega + 1}{R_\omega - 1}\right)^{1/2} f$$

provided $\omega_c \ll N$ [*Kunze et al.*, 1990]; for $R_\omega < 1.1$, higher order terms are necessary [see *Polzin et al.*, 1995]. Values for GM76 are $R_\omega=3$ and $\omega_c = 2^{1/2} f$. Adjustments for non-GM76 frequency content are $\alpha = 1+R_\omega^{-1}$ in (5.2) for energy density and

$$\left\langle \frac{\omega^2-f^2}{N^2-\omega^2} \right\rangle \Big/ \left\langle \frac{\omega^2-f^2}{N^2-\omega^2} \right\rangle_{\mathrm{GM}} = \frac{\omega_c^2-f^2}{\omega_{c\mathrm{GM}}^2-f^2} = \frac{2}{R_\omega-1}$$

in (5.5) for the Doppler shift term. Dividing the result of (5.4) evaluated at k_c for the general spectrum by that at $k_{c\mathrm{GM}} = 0.1$ cpm for GM76 yields the parameterization

$$\varepsilon_{\mathrm{iwP}} = \varepsilon_{0P} \left(\frac{k_{c\mathrm{GM}}}{k_c}\right)^2 \frac{N^2}{N_0^2} \frac{\alpha}{\alpha_{\mathrm{GM}}} \left(\frac{2}{R_\omega-1}\right)^{1/2} \tag{5.7}$$

where $\varepsilon_{0P} = 6.7 \times 10^{-10}$ W kg^{-1} is the GM76 expectation from Equation 11 of *Polzin et al.* [1995] for $N = N_0$ at 27° N. By assumption, $r(m)$ depends only on the background variance $Fr'^2(m)$, which is 0.7 in both cases (and so $r = 0.75$ for both), and variations in $\cosh^{-1}(N/f)$ are negligible. Because $k_{c\mathrm{GM}}/k_c =$

$\phi_{\mathrm{Frc}}/\phi_{\mathrm{FrcGM}}$, either ratio relates the general spectrum to GM76.

The *Gregg* [1989] parameterization of (5.4) can be expressed as

$$\varepsilon_{\mathrm{iwG}} = \varepsilon_{oG} \left(\frac{\langle Fr'^2_{10} \rangle}{Fr^2_{10\mathrm{GM}}} \right)^2 \frac{N^2}{N_0^2} \tag{5.8}$$

where the GM76 value $\varepsilon_{oG} = 7 \times 10^{-10}$ W kg^{-1} is established empirically, to match assorted observations within a factor of 2. No adjustments are made for frequency content. No particular form is assumed for Φ_{Fr}, and the ratio of observed 10-m first-differenced fluctuation variance to its GM76 counterpart, $Fr^2_{10\mathrm{GM}} = 0.33$, is used in place of the spectral ratio $\phi_{\mathrm{Frc}}/\phi_{\mathrm{FrcGM}}$ implicit in $\varepsilon_{\mathrm{iwP}}$. For higher level spectra that begin to roll off before 0.1 cpm, this fixed bandwidth approach tends to underestimate the modeled dissipation [*Gargett*, 1990].

The model Froude spectra in Figure 5.6 refines the composite spectrum of *Gargett et al.* [1981] by combining the internal wave spectrum assumed for $\varepsilon_{\mathrm{iwP}}$ with the Nasmyth turbulence spectrum. Further discussion is deferred to the next chapter, where buoyancy parameters k_b and $\phi_{\mathrm{Fr}b}$ and viscous parameters k_s and $\phi_{\mathrm{Fr}s}$ are defined. Manipulation of (5.7) allows low-wavenumber parameters k_c and ϕ_{Frc} to be computed from measured dissipation rates and stratification. Projected spectra are then compared, in that chapter, to observed spectra toward understanding the success or failure of $\varepsilon_{\mathrm{iwP}}$ or $\varepsilon_{\mathrm{iwG}}$ in estimating ε in diverse regions of the Current.

5.3.3 Comparison to observations

Within 1-MPa (100-m) intervals at each station, observed average $\overline{\langle \varepsilon \rangle}$ are compared to the parameterizations. To evaluate $\varepsilon_{\mathrm{iwP}}$ via (5.7), k_c is inferred by accumulating the fluctuation spectrum until $Fr'^2(k_c) = 0.7$, and N^2 is taken as the interval average, $\overline{\langle N^2_{10} \rangle}$. For the comparison in the upper panel of Figure 5.7,

GM76 frequency content is assumed by fixing $R_\omega = 3$. For most of stations 3 through 6—about 63% of the section—agreement to within a factor of 2 is realized. Above 2 MPa at station 5 and above 1.2 MPa at station 7, $\varepsilon_{\mathrm{iwP}}$ underestimates $\overline{\langle\varepsilon\rangle}$ by factors of 2 to 4. Over the two western stations and most of station 7, $\varepsilon_{\mathrm{iwP}}$ is 4 to 8 times too low, and more than 8 in a few spots (including the TSBL of station 3). Adjustment of $\varepsilon_{\mathrm{iwP}}$ for non-GM76 frequency content by using $R_\omega = Fr'^2(k_c)/St^2(k_c)$ yields mixed results, which are examined later in this chapter.

Interval averages $\overline{\varepsilon_{\mathrm{iwG}}}$ are formed from 0.1-MPa gridded $\varepsilon_{\mathrm{iwG}}$, which are generated via (5.8) from station mean profiles of $\langle Fr_{10}'^2\rangle$ and $N^2 = \langle\widetilde{N_{10}^2}\rangle$. Ratios $\overline{\langle\varepsilon\rangle}/\overline{\varepsilon_{\mathrm{iwG}}}$ (not shown) are about 15% higher on average than $\overline{\langle\varepsilon\rangle}/\varepsilon_{\mathrm{iwP}}$, and they share the same basic features shown in the upper panel of Figure 5.7.

There is motivation, and justification, for considering the contribution of subinertial shear to the downscale energy flux modeled by (5.1). Its inclusion in the assumed background flow suggests that total rather than fluctuating Φ_{Sh} are appropriate for (5.2); a lower k_c results if $Fr^2(k_c) = 0.7$ rather than $Fr'^2(k_c) = 0.7$ initiates the spectral rolloff. *Polzin et al.* [1996] estimate that Doppler shifting by mean shear of along-flow waves competes with the large-scale internal wave effects when the mean Fr^2 exceeds 0.05 (i.e., $Ri < 20$); mean shear does not affect cross-flow waves. Depending on the strength of the subinertial shear relative to the internal wave background and on the distribution of wave azimuths and frequencies, the combined effect of Doppler shifting in such a flow, $\langle dm/dt\rangle$, may not be properly represented by (5.3) and previously established $r(m)$.

To include the simplest contributions of mean shear—while ignoring less definite consequences—total shear spectra and variances are used in place of fluctuating quantities in $\varepsilon_{\mathrm{iwP}}$ or $\varepsilon_{\mathrm{iwG}}$. This approach also establishes upper bounds

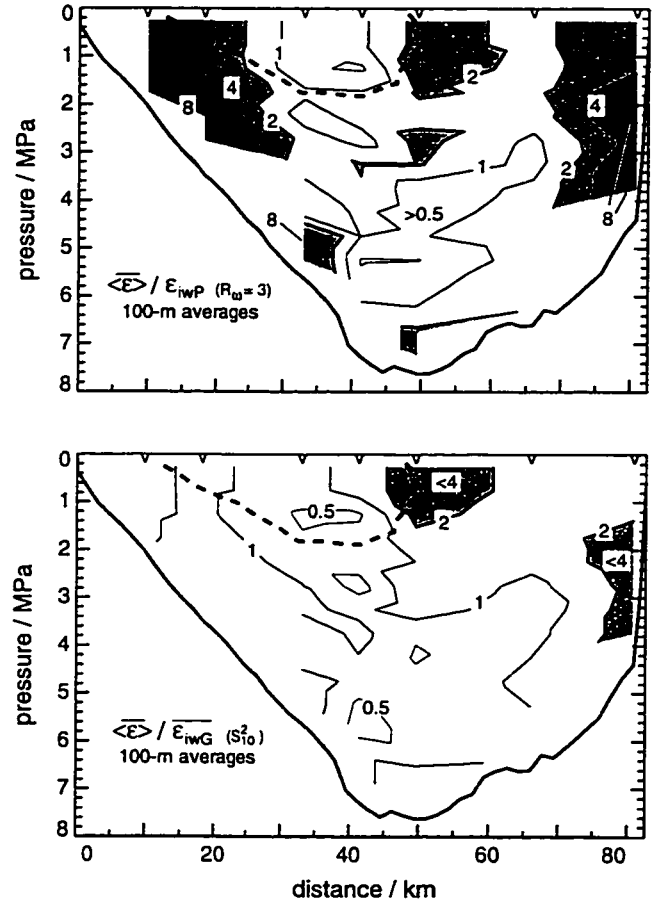

Figure 5.7: Patterns for ratios of observed-to-scaled ε averaged or computed within 1-MPa windows centered every 0.5 MPa (from 0.75 MPa onwards). Upper panel compares the spectral scaling of *Polzin et al.* [1995], given $R_\omega = 3$ for GM76 frequency content. Lower panel compares the scaling of *Gregg* [1989] modified to use the square of total shear variance, $\langle S_{10}^2 \rangle^2$. Dashed line is 1.2-m s^{-1} isotach.

for the scalings, in that it avoids underestimation of internal wave shear (especially cross-channel) related to the uncertain removal of subinertial flow from these Florida Current measurements. For an empirical test, $\overline{\varepsilon_{\mathrm{iwG}}}$ are computed by substituting $\langle Fr_{10}^2 \rangle$ for $\langle Fr_{10}'^2 \rangle$ in (5.8) before forming interval averages. As shown in the lower panel of Figure 5.7, the agreement with $\overline{\langle \varepsilon \rangle}$ in the high mean shear regions of stations 1 through 3 is now better than a factor of 2. Station 7 also shows improvement, although beneath 1 MPa the scaling still falls short (as it does at station 5 above 1 MPa). Elsewhere, the favorable comparison with $\varepsilon_{\mathrm{iwP}}$ (upper panel) is conserved, aside from small regions within and under the core where $\overline{\varepsilon_{\mathrm{iwG}}} > 2\overline{\langle \varepsilon \rangle}$. Computation of $\varepsilon_{\mathrm{iwP}}$ with k_c inferred from total Froude spectra yields similar results (not shown) to those for $\overline{\varepsilon_{\mathrm{iwG}}}$ computed with $\langle Fr_{10}^2 \rangle$, except in regions of high mean shear or strong turbulence where the spectral representation of large-scale shear variance is inadequate.

The fair agreement, overall, of $\varepsilon_{\mathrm{iwP}}$ and $\varepsilon_{\mathrm{iwG}}$ with observed dissipation rates was not anticipated. The background conditions of strong flow, nearby topography, and vertical and lateral shear are in sharp contrast to the remotely forced ocean pycnocline that *Henyey et al.* [1986] assume in their simulations and model. Close matching of $\overline{\langle \varepsilon \rangle}$ by $\varepsilon_{\mathrm{iwP}}$—computed with fluctuating shear—occurs even in broad regions where mean shear is such that $\langle \widetilde{Fr}_{10} \rangle^2 > 0.2$. Regardless of the processes driving the downscale energy flux, the resulting dissipation here is predicted with the same skill—to within a factor of 2—that *Gregg* [1989] claims for $\varepsilon_{\mathrm{iwG}}$. The high mean shear zones are an exception, but there it takes only the substitution of total for fluctuating shear variance to compute acceptable estimates.

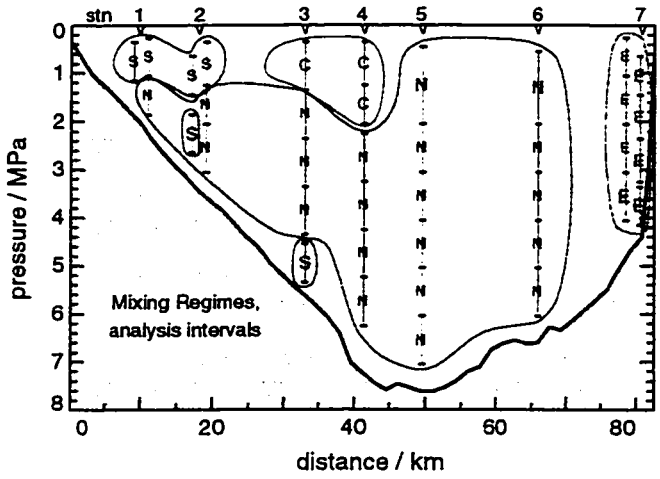

Figure 5.8: Mixing regimes with boundaries of analysis intervals indicated. Regimes are outlined, with symbols marking the midpoints of the intervals: 'N' for the interior (green), 'C' for the current core (blue), 'S' for the zones of high mean shear (red), and 'E' for the east channel wall (brown). Variations in symbol sizes reflect subdivisions within a regime (see Table 5.1). Interval thicknesses range from 80 m to 160 m, but most are 100 m. For stations 1, 2 and 7, intervals from the first occupation are left of those from the second occupation.

5.4 Mixing Regime Characteristics

Mixing and finescale activity throughout most of the Florida Straits section are moderate by oceanic standards, judging by the observed distributions of $\langle K_\rho \rangle$ and $\langle Fr_{10}'^2 \rangle$. Dissipation rates are consistent with the downscale energy flux expected for internal wave interactions, despite appreciable background shear and subinertial variability. Exceptions to this broad picture are found in zones of high mean shear, in the current core, on the east side at station 7, and in TSBLs. The differing nature of these regions suggests five distinct mixing regimes (with plot symbols as in Figure 5.8):

- **Interior (N):** This is the large region of moderate $\langle K_\rho \rangle$ and $\langle Fr_{10}'^2 \rangle$, in which both fluctuating and total shear variance are good indicators of ε.

- **High mean shear zones (S):** In the areas containing the highest mean shear, dissipation rates exceed those anticipated from fluctuating shear; total shear variance is a better indicator here.

- **Current core (C):** The weakest diffusivities of the section are found near the surface in the high velocity axis of the current. The weak fluctuating shear slightly overpredicts ε.

- **East channel wall (E):** Fluctuating shear is predominately cross-channel, suggesting that the nearby topography is affecting the internal wave field. Dissipation is sometimes weak and sometimes strong and tends to be underpredicted by $\varepsilon_{\mathrm{iwP}}$, unless higher frequency content is considered.

- **Turbulent stratified boundary layers (TSBLs):** The highest K_ρ occur in these energetic layers, which often appear as interfaces or transition zones between well-mixed boundary layers below and interior waters above.

Statistics and spectra are used to characterize and distinguish the regimes, and to understand influences on mixing and internal waves in each. Determination of regime boundaries is guided by features in the station mean profiles. Contrast among the regimes is enhanced by examination of characteristics computed on designated vertical intervals. Most deliberately chosen are the interval bounds for all high mean shear zones, for the weakly mixing core, and for the TSBL deep at the east wall (Figure 5.8). Considerations are also made toward searching for dependencies on background shear or stratification, and avoiding or minimizing boundary layer contributions (in non-TSBL intervals).

Most interval thicknesses are 100 m, the uppermost at stations 5 and 6 are 160 m and 150 m, and some are 80 m or 90 m to fit a regime's extent; thinner

intervals are prohibited owing to poor spectral results. A total of 38 intervals are defined, including separate ones for the separate occupations of stations 1, 2 and 7: For example, different bounds are required to isolate the high shear zones at station 2 before and after June 9th (Figure 3.8). Most TSBLs are too thin or too variable to be assigned analysis intervals; those at stations 3 and 7 are appropriate, but they are considered in the context of the high mean shear zones (HMSZs) and the east channel wall, respectively.

Each analysis interval is characterized by several attributes, which are based either on interval averages of 0.1-MPa (10-m) station mean profiles or on quantities derived from interval spectra. Table 5.1 summarizes some basic attributes and emphasizes those that distinguish each regime (or subdivision within a regime).

5.4.1 Interior

The interior lies in an active and variable subinertial environment, and exhibits turbulence and finescale variance similar to that observed in a moderately forced oceanic pycnocline. Interior intervals are distinct from the other regimes in their pairings of $\overline{\langle N_{10}^2 \rangle}$ and $\overline{\langle \varepsilon \rangle}$ with resulting intermediate diffusivities (Figure 5.9). Less distinct are interior $\overline{\langle \tilde{S}_{10} \rangle^2}$, which are similar in range and stability to intervals of the core and east wall.

Observed dissipation rates in the interior are anticipated fairly well by the internal wave scalings (Figure 5.10). This result is robust, whether comparing $\varepsilon_{\mathrm{iwP}}$ (with $R_\omega = 3$) or $\varepsilon_{\mathrm{iwG}}$. Of the 21 intervals, all but one—the upper one at station 5—have their observed $\overline{\langle \varepsilon \rangle}$ matched by $\varepsilon_{\mathrm{iwP}}$ within a factor of 2.1. When $\varepsilon_{\mathrm{iwG}}$ is computed with total shear variance, the station 5 outlier is in closer agreement, while observations in seven intervals are overestimated by factors of 2.1 to 2.7. Consideration of non-GM76 frequency content for $\varepsilon_{\mathrm{iwP}}$ generally has little effect, given the R_ω of 2 to 5 inferred from fluctuating Froude and strain

Table 5.1: Mixing regime statistics: Averages or summations over each interval's bounds. Distinguishing characteristics of (sub)regimes are highlighted. For subregimes with only two analysis intervals, paired values are ordered by station number and date. Otherwise, ranges of values are shown.

	$\overline{\langle N_{10}^2 \rangle}^{1/2}$	$\overline{\langle \epsilon \rangle}$	$\overline{\langle K_\rho \rangle}$	$\overline{\langle \tilde{S}_{10} \rangle^2}^{1/2}$	$\overline{\langle \widetilde{Fr}_{10} \rangle^2}$	$\frac{Fr'^2(k_c)}{Fr^2_{GM}(k_c)}$	$\frac{\overline{\langle \epsilon \rangle}}{\epsilon_{IWP}}$
	10^{-3} s^{-1}	10^{-9} W kg^{-1}	10^{-5} m^2 s^{-1}	10^{-3} s^{-1}			
Interior							
Stns 1–4	4.2–9.0	1.5–8.9	1.3–5.1	1.0–5.5	0.06–**0.53**	**1.5–3.5**	**0.6–2.0**
Stns 5,6 > 2 MPa	3.7–7.0	1.4–10.1	0.7–6.9	1.4–2.6	0.06–**0.55**	**1.3–3.7**	**0.6–2.1**
Stns 5,6 < 2 MPa	12.0,12.8	29.2,12.0	4.0,1.4	2.3,2.9	0.03,0.05	**2.1,1.5**	2.7,**1.8**
High Mean Shear							
Shallow < 1.5 MPa	16.3–17.9	9.9–49.4	0.6–3.2	**10.4–12.0**	0.41–0.47	0.7–1.2	**4.0–6.0**
Turbulent, Stns 2,3	7.4,6.7	**67.7,141.5**	**27.3,55.7**	**8.3,9.1**	**1.3,1.8**	1.4,3.6	**33.2,3.7**
Current Core							
Stns 3,4	10.6–16.0	*1.2–4.0*	*0.2–0.3*	2.4–4.3	0.02–0.17	0.8–1.3	*0.4–0.6*
East Wall							
June 6	5.1–12.8	*0.7*–5.9	*0.6–0.9*	1.1–3.8	0.04–0.08	0.9–1.0	1.3–2.5
June 13	3.6–12.9	7.6–**50.8**	3.6–**38.6**	1.7–5.6	0.19–0.36	1.5–3.4	2.0–**13.9**
TSBL, June 6,13	4.5,5.5	**21.5,36.6**	**22.9,23.3**	2.4,4.3	0.26,**0.59**	2.3,1.7	**8.6,18.3**

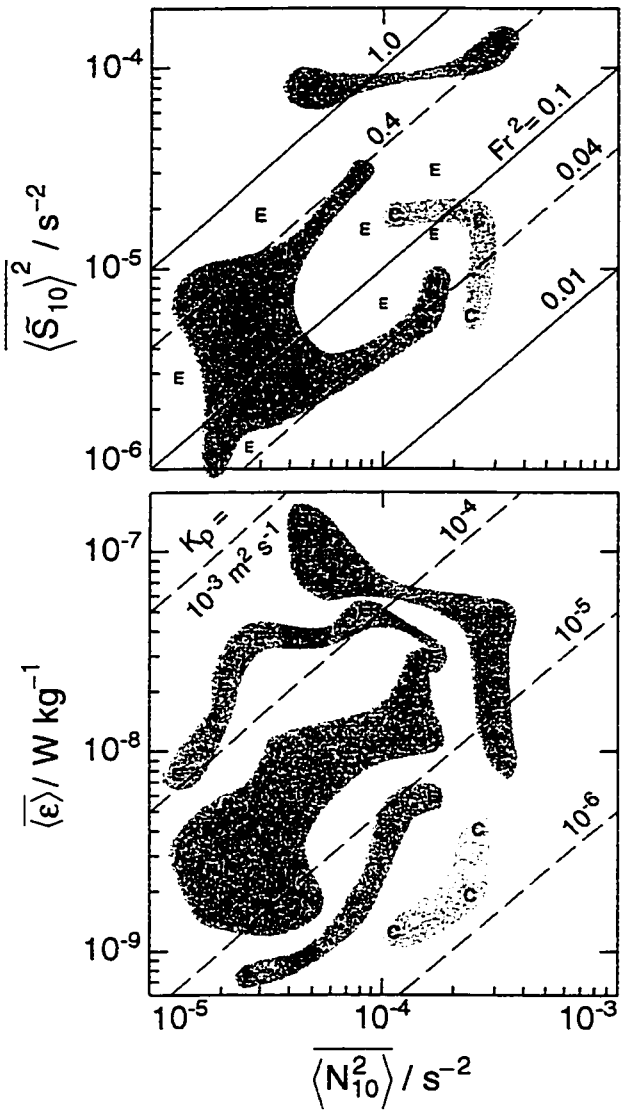

Figure 5.9: Interval statistics, vertically averaged from 0.1-MPa mean profiles. Symbols are explained with Figure 5.8. Upper panel: mean shear squared vs buoyancy frequency squared; diagonals are lines of constant $Fr^2 = \overline{\langle \tilde{S}_{10} \rangle^2} / \overline{\langle N_{10}^2 \rangle}$. Lower panel: dissipation rate vs buoyancy frequency squared; diagonals are lines of constant $K_\rho = 0.2\,\overline{\langle \varepsilon \rangle} / \overline{\langle N_{10}^2 \rangle}$. Note that these inferred values of Fr^2 and K_ρ often differ from $\overline{\langle \widetilde{Fr}_{10} \rangle^2}$ and $\overline{\langle K_\rho \rangle}$.

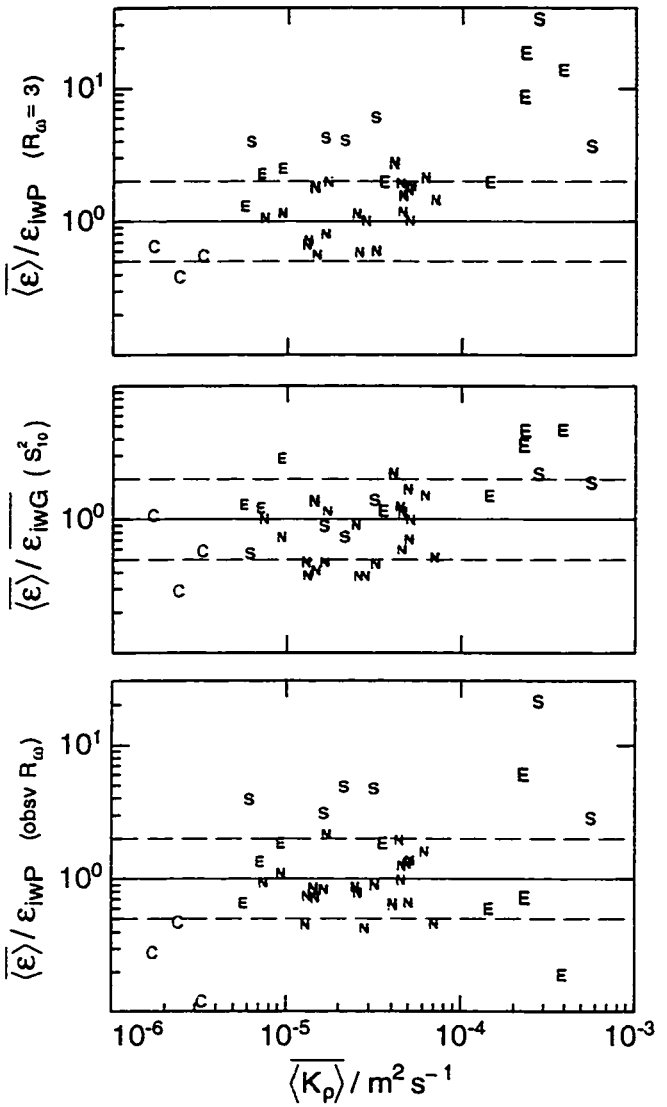

Figure 5.10: Ratios of observed to scaled interval-averaged dissipation rates, plotted against average $\overline{\langle K_\rho \rangle}$ of 0.1-MPa mean profiles. Symbols are explained with Figure 5.8. Dashed lines delimit factor-of-2 agreement. Observed ε are compared to: (upper panel) spectral scaling of *Polzin et al.* [1995], assuming GM76 frequency content ($R_\omega = 3$); (middle panel) spatial scaling of *Gregg* [1989], modified to use total rather than fluctuating shear variance; (lower panel) *Polzin et al.* [1995], adjusted for non-GM76 frequency content using observed R_ω.

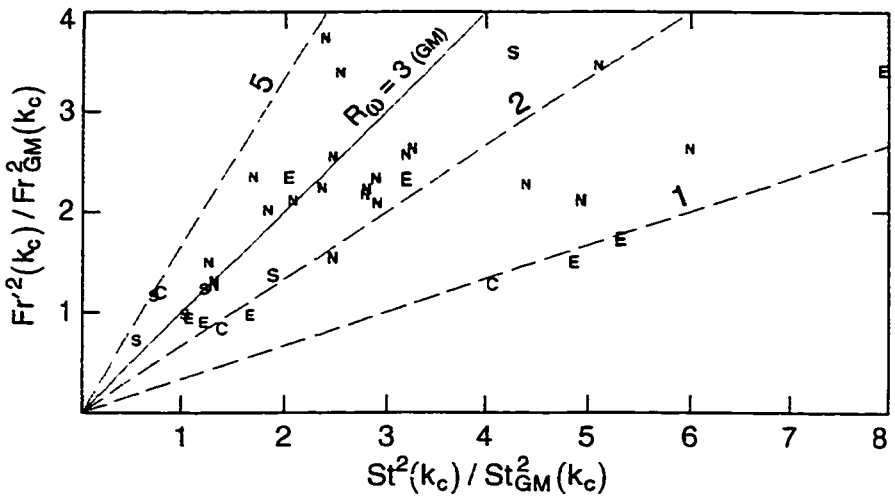

Figure 5.11: Ratios to GM76 values of fluctuation Froude variance and strain variance, computed by integrating interval (and GM76) spectra to wavenumber k_c where $Fr'^2(k_c) \approx 0.7$. Symbols are explained with Figure 5.8. Diagonals are lines of constant shear-to-strain ratio, $R_\omega = Fr^2/St^2$, which is 3 for GM76.

spectra (Figure 5.11). For the anomalous station 5 interval, the low $R_\omega = 1.3$ more than triples ε_{iwP} to slightly overpredict $\overline{\langle\varepsilon\rangle}$. In three other intervals, the modified ε_{iwP} are 2.4 times higher than observed values.

Interior intervals represent a variety of finescale shear characteristics. Mean $\overline{\langle\widetilde{Fr}_{10}\rangle^2}$ range from the lowest in the section to nearly the highest (Figure 5.12a); the mean component is 25% to 43% of the total when $\overline{\langle\widetilde{Fr}_{10}\rangle^2} > 0.25$, but is less than 28% of $\overline{\langle Fr_{10}^2\rangle}$ when $\overline{\langle\widetilde{Fr}_{10}\rangle^2} < 0.25$. Mean shear is often dominated by the north component, but the east one is sometimes significant (Figure 5.12b). Fluctuating variance in the low-wavenumber band is 1 to 4 times GM76 levels (Figure 5.11), with east components about 1 to 2 times the north ones (Figure 5.12c). Clockwise fluctuating variance always exceeds anticlockwise, and is often more than twice as high (Figure 5.12d); many of the higher ratios occur with higher $\overline{\langle\widetilde{Fr}_{10}\rangle^2}$ just beneath the core or deep in midchannel (Figure 5.5). Upper

station 5 is again notable, with the highest east-to-north ratios for both mean and fluctuating shear, and with the least rotary polarization (Figure 5.12b,c,d); many attributes of this interval are more typical near the east channel wall.

The background environment in the interior varies in channel bathymetry and Rossby number, Ro, both of which influence internal wave behavior. At western stations 1 and 2—and to a lesser extent at station 3—intervals are wedged between high shear above and the gentle slope below; the subinertial flow fluctuates appreciably, and Ro is as high as 0.7. Stations 3 and 4 are under the current core, where $Ro \approx 0$. Topography is bumpy and uneven at stations 5 and 6, and the cross-channel slope is somewhat flatter than on the west side; the subinertial flow is relatively steady, with Ro of -0.1 to -0.3 below 2 MPa. The two upper intervals lie above both velocity and salinity maxima, with anticyclonic flow of Ro near -0.5; the internal wave bandwidth is broadened here by the high buoyancy frequency and the low $f_{\text{eff}} \approx 0.75f$.

The interior exhibits moderate diffusivity resulting from dissipation rates that are consistent—through parameterizations based on internal wave interactions—with finescale shear variance. This is true despite the background environment of nearby topography, weak to moderate mean shear, and significant horizontal shear. It will also be shown that interior intervals share a commonly shaped Froude spectra, although cross spectra and coherences vary.

5.4.2 High mean shear zones

These intervals feature the highest mean shears observed in the section (Figure 5.9), shears that are predominately northward (Figure 5.12b). Dissipation rates are high, and are at least twice those predicted by ε_{iwP} (Table 5.1); adjustments for frequency content—unreliable owing to uncertain strains—are inconsequential (Figure 5.10). Total shear variance does, however, provide a fair

Figure 5.12: Comparisons of shear components, displayed against total variance $\overline{\langle Fr_{10}^2 \rangle}$. (a) Mean $\overline{\langle \widetilde{Fr}_{10} \rangle^2}$, with diagonal dashed lines showing mean-to-total ratios of 1.0, 0.5, and 0.25. (b) Ratios of east-to-north squared mean shear, based on interval averages of the $\langle \widetilde{S}_{10} \rangle^2$ components. Ratios of fluctuating shear variance—(c) east-to-north and (d) clockwise-to-anticlockwise (looking downward)—are computed from spectral components accumulated up to 0.07 cpm. The highest $\overline{\langle Fr_{10}^2 \rangle}$—plotted past 1.9 in (b) through (d) to fit the restricted range—has an actual value of 2.8. The two intervals of $\overline{\langle \widetilde{Fr}_{10} \rangle^2} > 1$ are offscale of (a); their mean-to-total ratios are 0.64 and 0.73 (Table 5.1).

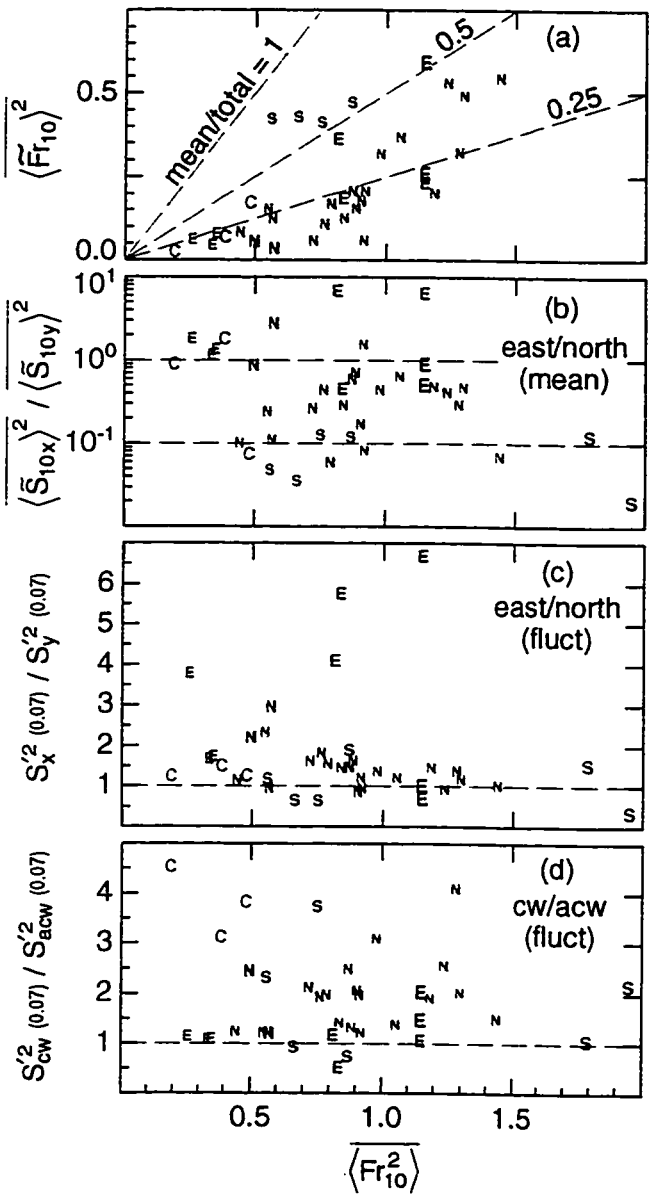
(a)
mean/total = 1
0.5
0.25
(b)
east/north
(mean)
(c)
east/north
(fluct)
(d)
cw/acw
(fluct)
0.5
1.0
1.5

estimate of $\overline{\langle\varepsilon\rangle}$ under the $\varepsilon_{\mathrm{iwG}}$ formulation in (5.8). Decomposition of shear is uncertain, because of the highly fluctuating subinertial flow (Figure 3.7). Even so, computed mean $\overline{\langle\widetilde{Fr}_{10}\rangle^2}$ are more than half the measured total $\overline{\langle Fr_{10}^2\rangle}$, in contrast to the interior's lesser ratios (Figure 5.12a and Table 5.1).

Two intervals—from deep station 2 and the TSBL of station 3—are distinct in that their $\overline{\langle\varepsilon\rangle}$ and $\overline{\langle K_\rho\rangle}$ are the highest over all the regimes (Figure 5.9), and that they alone have $\overline{\langle\widetilde{Fr}_{10}\rangle^2} > 1$ (Table 5.1). These turbulent zones were of limited duration, and seemed to be related to shifting or adjustment of the current's axis.

The other four intervals are up toward the surface at stations 1 and 2, where strong stratification moderates the high $\overline{\langle\tilde{S}_{10}\rangle^2}$ and $\overline{\langle\varepsilon\rangle}$ to yield, respectively, $\overline{\langle\widetilde{Fr}_{10}\rangle^2}$ and $\overline{\langle K_\rho\rangle}$ comparable to interior levels (Table 5.1). This shallow zone is probably a persistent feature of the current, although its strength and position may vary. Also, it is the most cyclonic region, with $Ro \approx 1$.

Fluctuating shear, regardless of its nature, is not a good indicator of dissipation in this regime. Apparently, mean shear does not dominate turbulent production, but it is important in its contribution to total shear variance, which is a good indicator of dissipation. This empirical result is puzzling, because the scaling $\varepsilon_{\mathrm{iwG}}$ is based on energy flux through internal wave interactions unlike those that should be expected in such a severe background.

5.4.3 Current core

The weakest diffusivities are found in the current core, where low dissipation occurs within high stratification (Figure 5.9). Total shear is also among the weakest, with $\overline{\langle Fr_{10}^2\rangle} < 0.5$ (Figure 5.12, abscissa). Mean northward shear is prominent only in the deeper interval of station 4. Fluctuating shear variance is close to GM76 levels (Figure 5.11), and dissipation is slightly less than the

scalings anticipate (Figure 5.10)—disregarding higher R_ω-modified $\varepsilon_{\mathrm{iwP}}$ based on unreliable strain estimates. The high ratio of clockwise-to-anticlockwise variance distinguishes fluctuating shear in the core (Figure 5.12d). The excess clockwise variance corresponds to a peak in core Froude spectra, which fall off more steeply than GM76 thereafter. Core intervals are from the high velocity axis of the current, where $Ro \approx 0$.

5.4.4 East channel wall

Profiles at station 7 are within 2 km of the channel's eastern side, which is virtually a wall owing to its steep slope. This regime is marked by its proximity to topography and—above the TSBL—by its predominately eastward shear variance (Figures 5.5 and 5.12b,c). The strong turbulence of the June 13th occupation is in sharp contrast to the weak activity of the June 6th occupation (Table 5.1).

In the two middepth intervals of June 13, $\overline{\langle K_\rho \rangle}$ exceeds 10^{-4} m^2 s^{-1}, levels matched only in the underlying TSBL and in the two turbulent high mean shear zones (Figure 5.10). The higher value is from the 90-m thick interval centered at 1.9 MPa, in which the $\overline{\langle \varepsilon \rangle}$ of 5.1×10^{-8} W kg^{-1} is dominated by a vigorous event extending into a nearly homogenized layer that is 10 m to 20 m thick. This high dissipation is much greater than predicted by the internal wave scalings, unless $\varepsilon_{\mathrm{iwP}}$ is modified—unrealistically—for the extremely low $R_\omega < 1$ (Figure 5.11).

Finescale shear in the TSBL of station 7 differs from that up shallower. Northward mean shear contributes more than eastward to the high $\overline{\langle \widetilde{Fr}_{10} \rangle^2} > 0.25$ in the TSBL (Figure 5.12b). Fluctuating shear is nearly isotropic but exhibits some clockwise rotation with depth (Figure 5.12c,d). As in the energetic middepth interval discussed above, $\varepsilon_{\mathrm{iwP}}$ greatly understimates $\overline{\langle \varepsilon \rangle}$ without an excessive adjustment for low R_ω, and even $\varepsilon_{\mathrm{iwG}}$ computed with total variance is more than a factor of 3 too low (Figure 5.10).

In the remaining five east wall intervals, fluctuating shear is a fair indicator of dissipation, especially when ε_{iwP} is modified for high frequency content (Figure 5.10). The combined adjustments in (5.7) are moderate, ranging from 1.1 to 3.3 for the inferred R_ω of 3.4 to 1.3 (Figure 5.11). Higher frequency internal waves are a reasonable expectation near the east wall, for which the critical reflection frequency is around $0.1N$ to $0.3N$. Individual drop profiles of shear exhibit rectilinear behavior, indicative of higher frequencies than presumed for the more elliptical profiles of the interior.

5.4.5 Turbulent stratified boundary layers

These near-bottom layers account for nearly half of the section-averaged K_ρ, although occupying only 7% of the total record. Most prominent are TSBLs which exhibit higher dissipation, stratification and shear than waters immediately above (and below if an underlying layer is present). The previously discussed intervals deep at stations 3 and 7 are summarized in Table 5.1 and example profiles are shown in Figure 5.13. Some drops from other stations exhibit TSBLs that are similar to—though thinner than—those at stations 3 or 7. Others contain TSBLs that are less turbulent or less distinct. Because TSBLs vary in character and in position (depth range) from drop to drop, inter-regime contrast is enhanced by computing attributes for the each drop's TSBL, and then averaging appropriately to form station statistics. However, this increases mean ε, K_ρ and Fr^2 by only 50–100% for stations 3 and 7.

5.5 Summary of Observed Patterns

In this chapter, regions of high, moderate and low turbulent activity have been identified, and relationships between finescale variance and dissipation have been

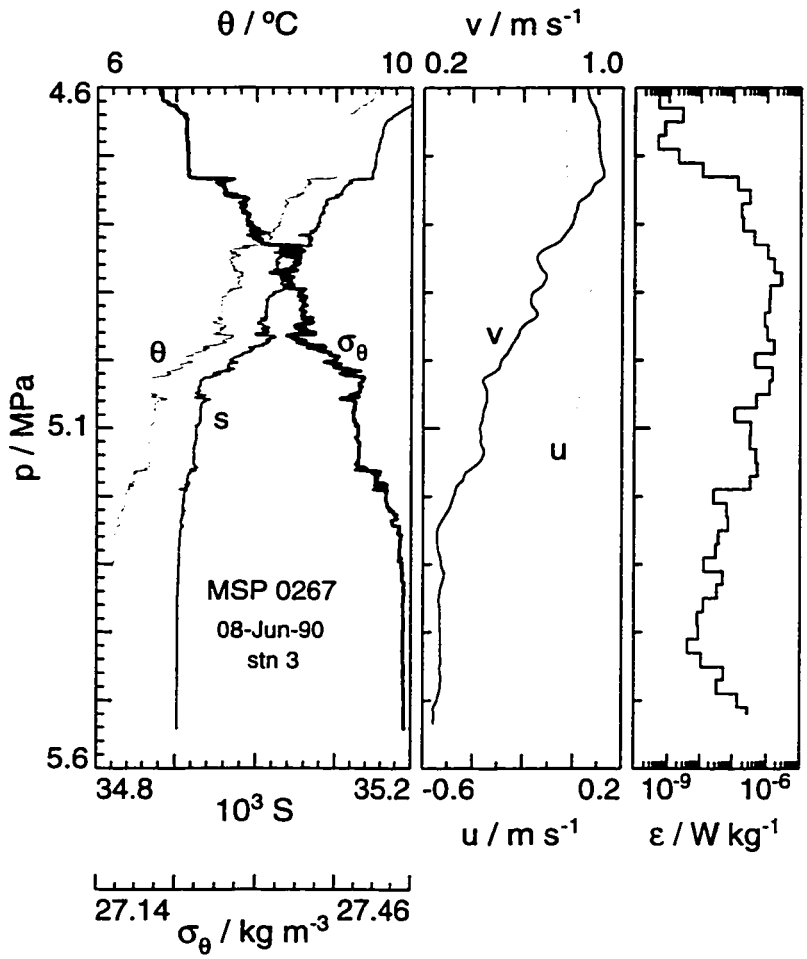

Figure 5.13: Boundary layer profiles for (a) station 3 beneath the core and (b) station 7 near the east wall. Hydrography and velocity scales are broader in (a) than in (b).

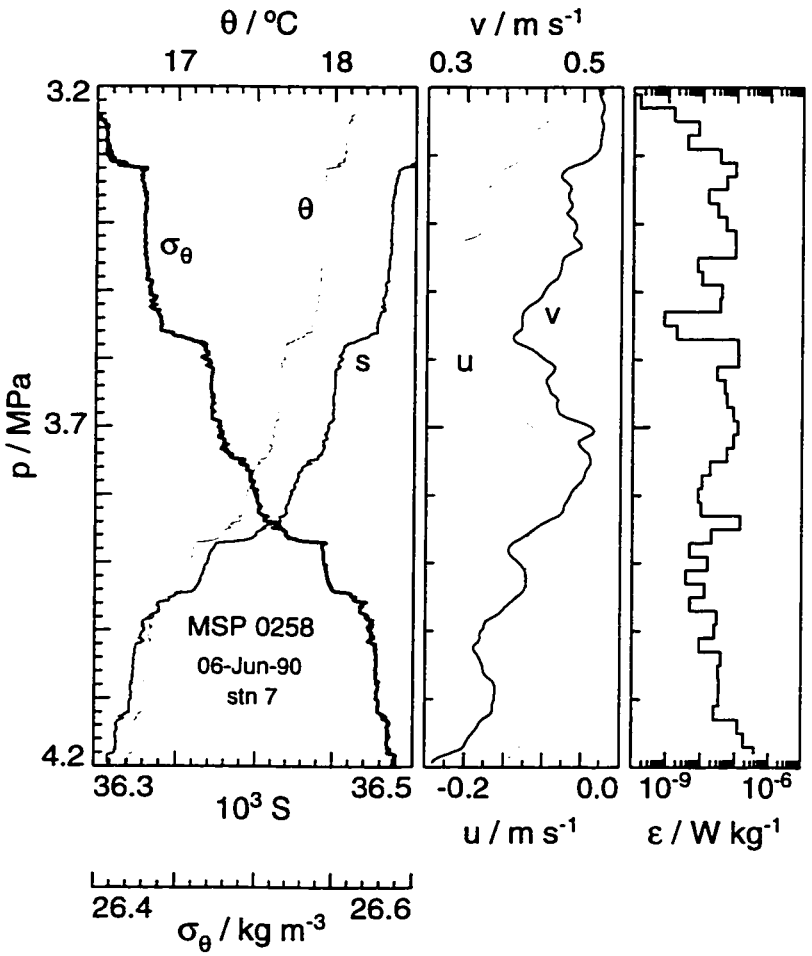

Figure 5.13: (b) Boundary layer, station 7

investigated. To accentuate the observed variety of background conditions and turbulent and internal wave activity, five mixing regimes have been designated. Four of these seem to be linked to flow geography: In the current core mixing is weakest; high northward mean shear enhances the production of moderate turbulence west of the core and of strong turbulence in less persistent features deeper at stations 2 and 3; near the steep eastern slope of the channel, finescale shear is dominated by its eastward component and turbulence varies from nearly the weakest to nearly the strongest; within 100 m of the channel bottom, strong turbulence in stratified boundary layers accounts for half the effective diffusivity over the entire survey. The remaining 67% of the current—designated the interior regime—contains turbulence and finescale variance whose levels and interrelationship are consistent with those expected for a moderately active oceanic pycnocline.

There is no significant dependence on background shear of turbulent or finescale quantities in the interior, despite its appreciable range of background Froude numbers. Some interior intervals with higher mean shear do exhibit elevated fluctuating Froude variance or clockwise-to-anticlockwise ratios, but counterexamples also exist. The greatest contrast related to mean shear is that between the high mean shear zones and the other regimes. Topography seems more of a factor, with influences evident both in the TSBLs and near the east channel wall.

Chapter 6

VERTICAL WAVENUMBER SPECTRA

Finescale spectra are examined to gain further insight into relationships between internal waves and turbulence, particularly within a background shear. Froude spectra are compared in level and shape with the GM76 model and with the form presumed by the dissipation scaling $\varepsilon_{\mathrm{iwP}}$. The focus is the low wavenumber band, whose cutoff k_c will be inferred via (5.7) from observed ε and N rather than the earlier integration to $Fr'^2(k_c) = 0.7$. Attributes of both total and fluctuation variance in this band are used to analyze the circumstances under which the scalings predict ε either poorly, as in some high K_ρ intervals in Figure 5.10, or reliably, as in the interior.

6.1 Variety of Spectra

Spectral levels and shapes vary throughout the current, as illustrated by the contrasting cases in Figure 6.1. At low wavenumbers, Froude spectra are bunched within a decade about GM76, as are strain spectra. As Φ_{Fr} roll off, they merge near GM76 at 0.14 cpm, consistent with geographically diverse observations of *Gregg et al.* [1993, 1996]. The rolloffs in Φ_{Fr} are steeper than in associated Φ_{St}. The hundredfold variation among Φ_{Fr} between 1 cpm and 10 cpm reflects the wide range in K_ρ, from the strongly turbulent regions to the moderately active interior to the weakly mixing core.

Most common are spectra characteristic of the interior regime, similar to

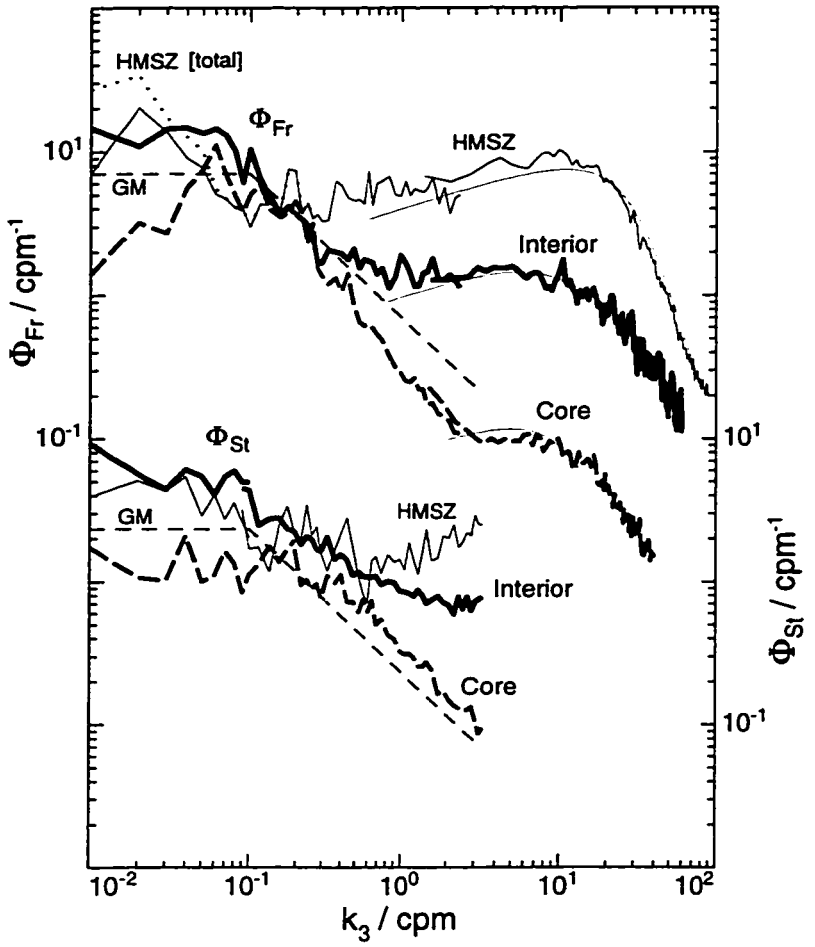

Figure 6.1: Representative Froude and strain spectra. Froude spectra are computed from demeaned ACM velocity profiles for 0.01–2.5 cpm and from airfoil probes beyond 1.3 cpm. Finescale strain spectra are computed from isopycnal displacements for $k_3 < 0.1$ cpm and from temperature perturbations for higher k_3 (spectra of temperature microstructure are resolved by MSP, but are not available for display). Heavy curve: Interior, station 5, 2.5–4.5 MPa, $N = 0.00533$ s^{-1}, $\varepsilon = 4.60 \times 10^{-9}$ W kg^{-1}. Heavy dashed curve: Core, station 4, 0.5–1.5 MPa, $N = 0.01516$ s^{-1}, $\varepsilon = 1.47 \times 10^{-9}$ W kg^{-1}. Light curve: High mean shear, station 2 (June 7th), 1.75–2.75 MPa, $N = 0.00700$ s^{-1}, $\varepsilon = 5.44 \times 10^{-8}$ W kg^{-1} (dotted curve is spectrum of total shear, that is, without demeaning). Light dashed curves: Approximate GM76 spectra. Smooth light curves: Average Nasmyth spectra weighted by the ε_{10} distribution for each interval.

those displayed for middepth at station 5. The Φ_{Fr} is near-canonical, with a rolloff—coinciding past 0.1 cpm with GM76—of slope near -1 that descends from a low-wavenumber plateau above GM76 to an inertial subrange of turbulence, whose slight rise spans a decade before reaching a viscous rolloff. The Φ_{St} is not canonical, as its rolloff is gentler and higher than GM76; its slope changes at higher wavenumbers than that of Φ_{Fr} from its upper plateau down the rolloff and into the turbulent range—which, though not archived for display, is resolved by MSP out to a diffusive rolloff [as in *Gregg et al.*, 1996]. Interior Φ_{Fr}, whether computed for total or fluctuating shear, are consistent with Figure 5.6, the form employed in parameterizing (5.4) as ε_{iwP} in (5.7).

The Froude spectrum from the core rises to a peak that is dominated by clockwise variance, descends initially along and then more steeply below GM76, and briefly flattens before a viscous rolloff. The strain spectrum is flat until rolling off just above GM76, again less steeply than Φ_{Fr}.

In regions where strong turbulence produces $K_\rho > 2 \times 10^{-4}$ m^2 s^{-1}, wide inertial subranges originate before 0.2 cpm, from near or above the GM76 plateau. Low wavenumber features are poorly resolved in such Φ_{Fr}, owing to the small spectral windows of 80 m to 100 m required to isolate the elevated turbulence. Important contributions from larger scale shear are missed, so the slope breaks before accumulation to $Fr'^2 = 0.7$, which consequently overestimates k_c—the sample spectrum in Figure 6.1 is almost into its inertial subrange at its inferred $k_c = 0.075$ cpm (Figure 6.2). Consideration of total rather than fluctuating Φ_{Fr} lowers the estimate for this high mean shear zone to $k_c = 0.025$ cpm, which corresponds better to the observed rolloff; use of this lower k_c in (5.7) raises ε_{iwP} ninefold.

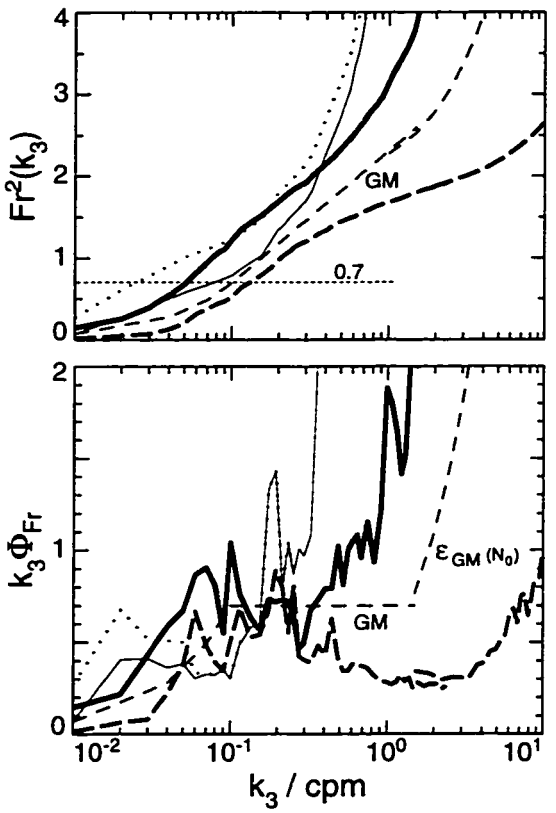

Figure 6.2: Froude functions and variance preserving display for spectra of Figure 6.1.

6.2 Model Froude Spectrum

A composite Froude spectrum is specified to extend that of *Gargett et al.* [1981] by explicitly defining—for given values of ε and N—the relationship between the internal wave band and the inertial subrange of turbulence. The model spectrum, shown in Figure 5.6, synthesizes features of numerous observed spectra with the dissipation scaling (5.7) of *Polzin et al.* [1995]. Four spectral bands are delineated in terms of cutoff wavenumber k_c, buoyancy wavenumber k_b, and Kolmogoroff wavenumber k_s.

The model Φ_{Fr} has a constant level of $\phi_{\mathrm{Fr}c}$ for all $k_3 < k_c$. The low wavenumber bandwidth is not fixed (as at 0.1 cpm in GM76), but varies such that $k_c\phi_{\mathrm{Fr}c} = 0.7$. Randomly propagating internal waves contribute to this portion of the spectrum, termed the intrinsic range by *Munk* [1981]. Note that observed spectra are seldom entirely constant or flat, so associating $\phi_{\mathrm{Fr}c}$ with the average level up to k_c is a more realistic interpretation.

The spectrum rolls off at $k_3 > k_c$ as

$$\Phi_{\mathrm{Fr}} \;=\; \phi_{\mathrm{Fr}c}\,(k_3/k_c)^{-1} \;=\; 0.7\,k_3^{-1} \quad [\mathrm{cpm}^{-1}]$$

in the compliant or saturated range, the transistion between internal waves and turbulence. The rolloff ends where it intersects the inertial subrange, which occurs at $k_3 = 0.6k_b$ and $\Phi_{\mathrm{Fr}} = 1.2\phi_{\mathrm{Fr}b}$ for the Nasmyth universal turbulent spectrum [*Oakey*, 1982]. When normalized by buoyancy parameters

$$k_b = (N^3\varepsilon^{-1})^{1/2}/2\pi \quad [\mathrm{cpm}] \tag{6.1}$$

and $\phi_{\mathrm{Fr}b} = {k_b}^{-1}$, observed Froude spectra often collapse onto a common rolloff range [*Gargett et al.*, 1981; *Winkel et al.*, 1992; *Gregg et al.*, 1993]. Given dis-

sipation rates that scale as $\varepsilon_{\mathrm{iwP}}$, the bandwidth of the rolloff can be specified. Manipulating (5.7) for the GM76 spectrum yields $k_{b\mathrm{GM}} = k_{b\mathrm{GM0}}\,(N/N_0)^{1/2}$, where $k_{b\mathrm{GM0}}$=2.33 cpm is computed with $\varepsilon=\varepsilon_{0P}$ and $N=N_0$. For the general case,

$$k_c(\varepsilon_{\mathrm{iwP}}, N) \;=\; k_b(\varepsilon_{\mathrm{iwP}}, N)\,\frac{k_{c\mathrm{GM}}}{k_{b\mathrm{GM0}}}\left(\frac{N_0}{N}\right)^{1/2}\gamma^{1/2} \tag{6.2}$$

where $\gamma = (\alpha/\alpha_{\mathrm{GM}})(2/R_\omega - 1)^{1/2}$ is the adjustment in (5.7) for non-GM76 frequency content. Therefore, the rolloff bandwidth

$$\frac{0.6k_b}{k_c} \;=\; 14.0\left(\frac{N}{N_0}\right)^{1/2}\gamma^{-1/2}$$

widens as $N^{1/2}$ for a given k_c (ignoring γ); conversely, the bandwidth remains fixed for a given N, regardless of internal wave or turbulent spectral levels. As γ increases with higher frequency content, the bandwidth narrows.

In the inertial subrange of turbulence, Φ_{Fr} slopes up as $k_3^{1/3}$ from the terminus of the rolloff range. It flattens approaching its peak level of $0.65\phi_{\mathrm{Fr}s}$ at $0.16k_s$, with

$$k_s = (\varepsilon\nu^{-3})^{1/4}/2\pi \qquad [\mathrm{cpm}]$$

and where $\phi_{\mathrm{Fr}s}=\phi_{\mathrm{Sh}s}/N^2$ is the Kolmogoroff shear spectral level

$$\phi_{\mathrm{Sh}s} = 2\pi(\varepsilon^3\nu^{-1})^{1/4} \qquad [\mathrm{s}^{-2}\ \mathrm{cpm}^{-1}]$$

normalized as a Froude level. At wavenumbers higher than $0.16k_s$, the viscous rolloff follows the Nasmyth empirical spectrum. Because observed microscale spectra encompass multiple mixing patches, they are better represented by the average of Nasmyth spectra computed over the distribution of measured ε, rather than by the Nasmyth spectrum for the average ε. For simplicity, however, the

latter form is assumed in specifying this model Froude spectrum.

The model cannot describe spectra for weakly diffusive regimes, where the inertial subrange vanishes as its bandwidth

$$\frac{0.16k_s}{0.6k_b} = 0.267\left(\frac{\varepsilon}{\nu N^2}\right)^{3/4} \approx \left(\frac{K_\rho}{1.4\times 10^{-6}\ \mathrm{m^2\ s^{-1}}}\right)^{3/4}$$

drops below unity. Observed Φ_{Fr} associated with such low K_ρ often fall more steeply than the model from low-wavenumber levels thereby reaching turbulent ranges before $0.16k_s$ (and, therefore, before $0.6k_b$).

6.3 Finescale Spectra by Regime

The assorted spectra of Figure 6.1 and the canonical Φ_{Fr} model provide context for discussion of finescale Froude and strain spectra from the analysis intervals of Figure 5.8.

The reasons for spectrally inferred $\varepsilon_{\mathrm{iwP}}$ to disagree with observed $\overline{\langle\varepsilon\rangle}$ fall into two categories. First, the transfer of finescale shear variance to dissipative scales proceeds at a rate different from that modeled by (5.4) and parameterized by (5.7). In some cases, dissipation is driven by dynamics not considered by the model; in other cases, the model is appropriate, but some of its assumptions are incorrect or some of its terms are assigned inaccurate values. Second, owing to either uncertainty in the measurements or shortcomings in the spectral representation, variance is resolved inadequately at finescales—here, it will be assumed that ε and microscale Φ_{Fr} derived from the airfoil data are accurate. For all but the least diffusive intervals, the ACM measurements resolve the transistion near $0.6k_b$ from the rolloff into the subinertial range; airfoil and ACM spectra are well-matched where they overlap near 2 cpm, as demonstrated in Figure 6.1 and by *Winkel et al.* [1992] for this dataset and by *Gregg et al.* [1993] and *Winkel et al.*

[1996] for MSP in general.

6.3.1 Interior

The Froude and strain spectra from interior intervals (Figure 6.3) are similar to the examples from station 5 shown in Figure 6.1. Their low wavenumber levels exceed GM76 by the factors indicated in Figure 5.11, and Φ_{Fr} follow the -1 rolloff until flattening in inertial subranges reflecting the tenfold span in K_ρ (Figure 5.9). Rolloffs of Φ_{St} are gentler, remaining above GM76 with slopes of -0.8 to -0.6.

Low wavenumber Φ_{Fr} correspond closely to the canonical model, consistent with the decent agreement of scaled and measured dissipation shown in Figure 5.10. Interval averages $\overline{\langle\varepsilon\rangle}$ and $(\overline{\langle N_{10}^2\rangle})^{1/2}$ are used in (6.1) and (6.2) with $\gamma = 1$ to compute the wavenumbers k_b and k_c that determine the model spectrum. Observed Φ_{Fr} cluster about the projected $\phi_{\mathrm{Fr}c} = 0.7/k_c$ at $k_3 < k_c$, then follow the modeled rolloff to at least $k_3 = 10k_c$ (Figure 6.4). Because the rolloff band widens as $N^{1/2}$, some spread remains near the transistion into the inertial subrange; Φ_{Fr} collapse near this intersection when normalized by k_b and $\phi_{\mathrm{Fr}b}$, consistent with *Gargett et al.* [1981].

Finescale Froude variance is represented by the average level, $\overline{\Phi}_{\mathrm{Fr}}$, within the band $k_3 < k_c$. When $\overline{\Phi}_{\mathrm{Fr}} > \phi_{\mathrm{Fr}c}$, Froude variance is greater than expected for the observed dissipation, and $\varepsilon_{\mathrm{iwP}}$ will overestimate $\overline{\langle\varepsilon\rangle}$. Conversely, when $\overline{\Phi}_{\mathrm{Fr}} < \phi_{\mathrm{Fr}c}$, a deficit in Froude variance leads to $\varepsilon_{\mathrm{iwP}}$ underestimating $\overline{\langle\varepsilon\rangle}$. The limits $0.5 < \overline{\langle\varepsilon\rangle}/\varepsilon_{\mathrm{iwP}} < 2.0$ indicated on Figure 5.10 correspond to spectral ratios $1.4 > \overline{\Phi}_{\mathrm{Fr}}/\phi_{\mathrm{Fr}c} > 0.7$. For interior intervals, ratios for fluctuation Φ_{Fr} lie between 0.61 and 1.31, with four at 0.7 or less. The combination of all intervals yields $\overline{\Phi}_{\mathrm{Fr}} = (0.95 \pm 0.21)\phi_{\mathrm{Fr}c}$. Total Φ_{Fr}—which include contributions from mean shear characterized in Figure 5.12a—agree as well as their fluctuating counterparts with the canonical spectrum. Total ratios range from 0.72 to 1.75, with four exceeding

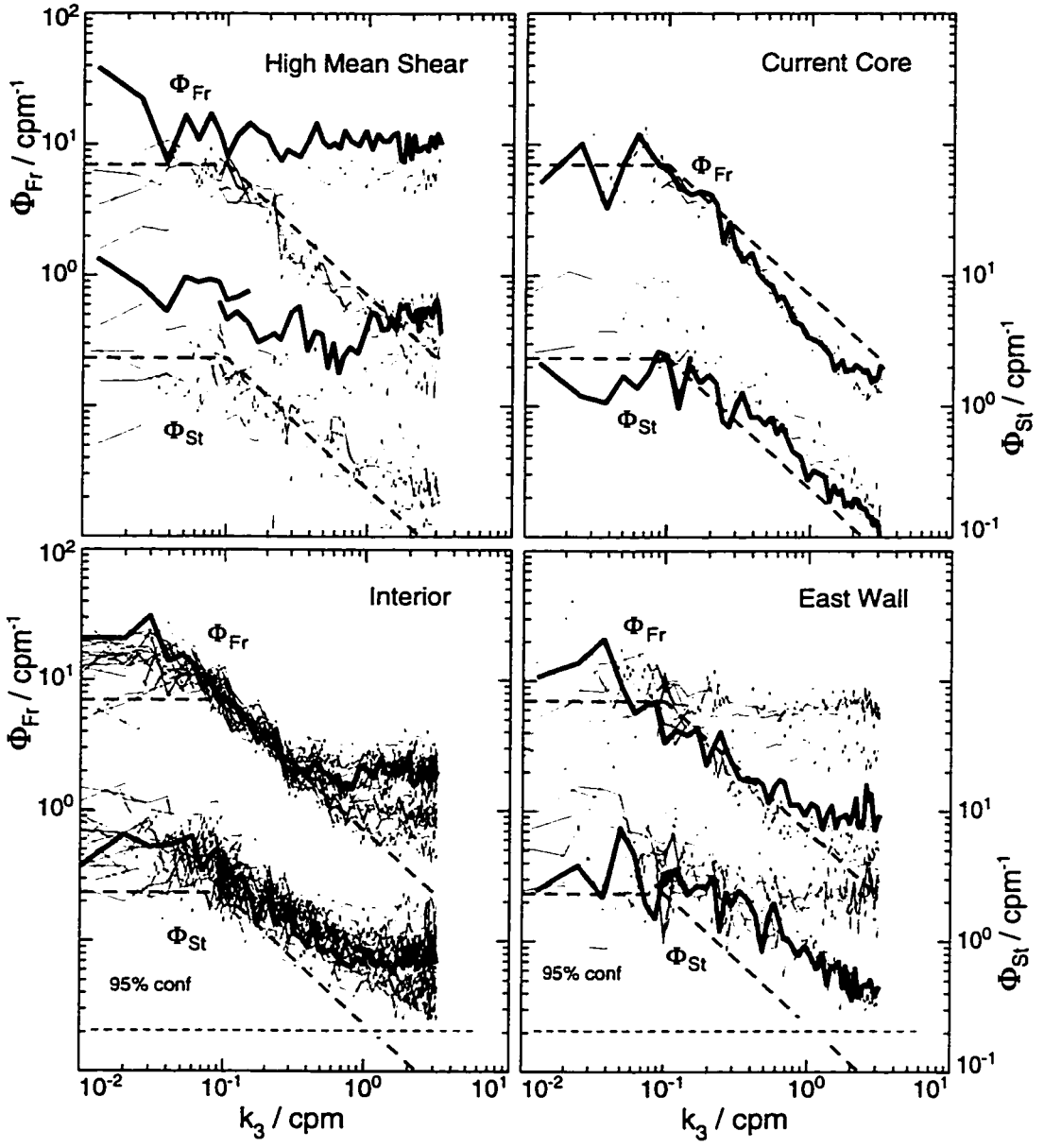

Figure 6.3: Finestructure spectra for mixing regime analysis intervals of Figure 5.8. Upper are Froude spectra computed from fluctuating shear. Lower are strain spectra based on isopycnal displacements for $k_3 < 0.1$ cpm, and on θ fluctuations for higher k_3. Spectra of a selected interval of each regime are highlighted for reference. Nominal 95% confidence limits are shown for Froude spectra of interior (10 drops) and east wall (4 to 6 drops) intervals; the narrower (wider) limits apply for current core (HMSZ) Φ_{Fr}. Limits for strain spectra are nearly twice as wide as for Froude. Dashed lines are approximate GM76 spectra.

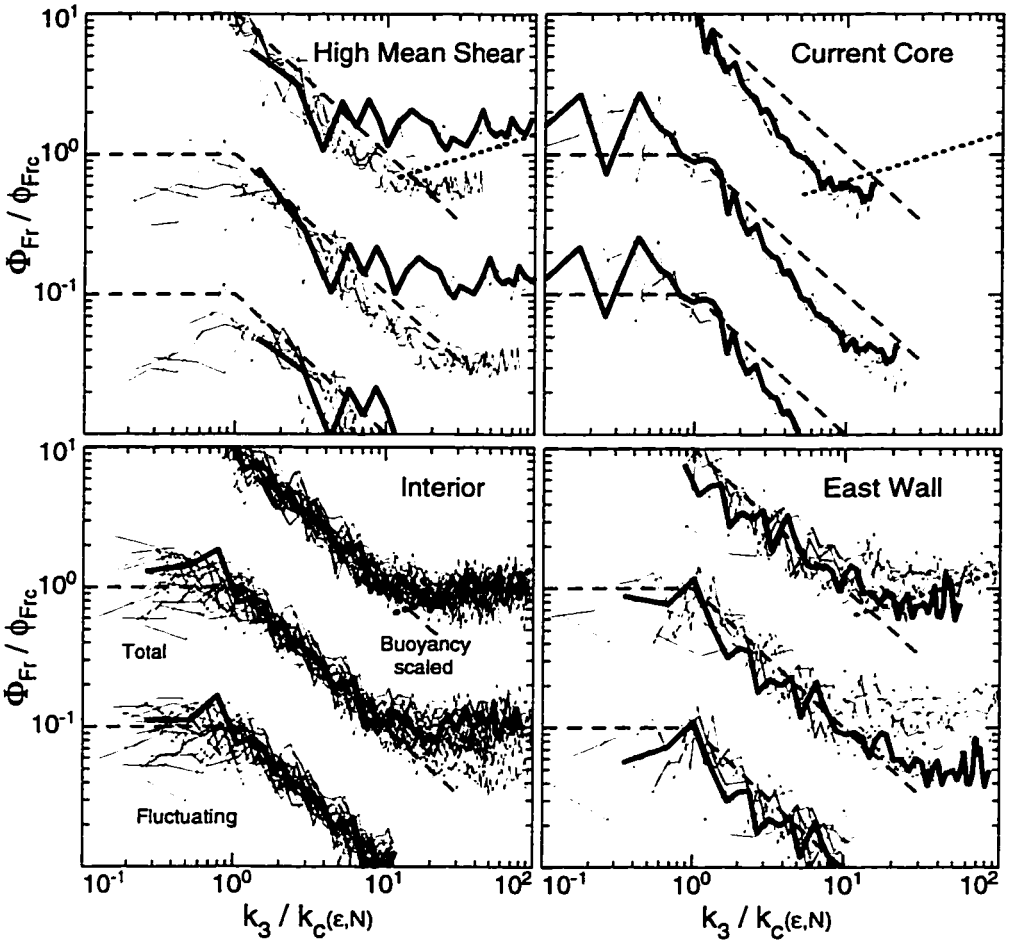

Figure 6.4: Comparisons of Froude spectra to composite model. Average ε and N^2 are used to compute k_b for each interval, and k_c result from (6.2) with $\gamma = 1$. In the middle of each panel, total Φ_{Fr} levels are scaled by $\phi_{Frc} = 0.7/k_c$ and wavenumbers by k_c; offset down a decade are similarly scaled fluctuating Φ_{Fr}, truncated past $k_3/k_c = 1$. In the upper corners, fluctuating Φ_{Fr} are scaled by $k_c = k_b/23.3$ and $\phi_{Frc} = 16.3/k_b$ (as if $\gamma = N/N_0$ in (6.2)) to test their collapse near the intersection of the rolloff (dashed line) and the inertial subrange (dotted line); these buoyancy-scaled spectra [*Gargett et al.*, 1981] are offset up a decade and are plotted only for $k_3/k_c > 0.8$.

1.4; overall, $\overline{\Phi}_{\mathrm{Fr}} = (1.12 \pm 0.28)\phi_{\mathrm{Frc}}$.

In the interior, finescale shear variance is a good indicator of turbulent dissipation. The near-canonical Φ_{Fr} are well suited to estimate the moderate diffusivities via the parameterization $\varepsilon_{\mathrm{iwP}}$. Results are nearly insensitive to factors such as significant subinertial shear, uncertainty in the decomposition of mean and fluctuating shear, non-GM76 frequency content inferred from shear-to-strain ratios, and anisotropy and asymmetry in the internal wave field.

As an open ocean counterpart, the PATCHEX North dataset [*Gregg et al.*, 1993] is most similar to the interior regime, particularly in its moderate K_ρ and in the shape and level of its near-canonical Φ_{Fr}.

6.3.2 High mean shear zones

Two varieties of Φ_{Fr} are apparent in Figure 6.3. Those from the strongly turbulent intervals are similar to the elevated example of Figure 6.1. Those from the highly stratified, upper region west of the core are near GM76 up to 0.1 cpm, after which they roll off slightly below GM76. Strain spectra are shown for completeness, but are unreliable.

The limited extent of strong turbulence in the highly diffusive intervals prohibits spectral resolution of the modeled spectral plateau at $k_3 < k_c$. When its projected k_c is less than twice the fundamental wavenumber $\Delta k_3 = 1/\Delta z$, a measured spectrum—such as that from the TSBL of station 7 highlighted in Figure 6.4—starts near or within the rolloff. The computation of $\varepsilon_{\mathrm{iwP}}$ via (5.7) is flawed for such cases, because $Fr'^2 = 0.7$ is a poor indicator of k_c; the resulting $\varepsilon_{\mathrm{iwP}}$ underestimates the modeled dissipation and, perhaps, the observations (as in Figure 5.10). Accumulation of total Φ_{Fr} to $Fr^2 = 0.7$ lowers the estimated k_c, but the spectral plateau remains unresolved.

Spectra from the four upper intervals do resolve several wavenumbers lower

than the projected k_c, but levels fall below the anticipated $\phi_{\mathrm{Fr}c}$ (Figure 6.4). In combination, the fluctuating spectra yield $\overline{\Phi}_{\mathrm{Fr}} = 0.46\phi_{\mathrm{Fr}c}$ and the total spectra yield $\overline{\Phi}_{\mathrm{Fr}} = 0.66\phi_{\mathrm{Fr}c}$—not quite high enough for $\varepsilon_{\mathrm{iwP}}$ to reach half the observed dissipation. The total spectra include much of the mean shear contribution, but some is missing at scales exceeding the interval thicknesses. This missing variance is captured when shear is computed spatially, as for the comparison to $\varepsilon_{\mathrm{iwG}}$ in Figure 5.10. The spatial approach also provides a decent measure of the total variance in the turbulent intervals, although the 10-m first differencing will tend to underestimate $\phi_{\mathrm{Fr}c}$ [*Gargett*, 1990].

6.3.3 Current core

The Froude and strain spectra in Figure 6.3 are similar to those of Figure 6.1. Each Φ_{Fr} peaks near 0.07 cpm, rolls off along GM76 until 0.2 cpm, then falls beneath GM76 with a steeper slope of -1.3 down to a narrow turbulent range at 2 cpm. Core Φ_{St} are unreliable at low wavenumbers, but their near-GM76 rolloff is notable in contrast to the steeper descent of Φ_{Fr}.

Because diffusivity in the core is weak, Froude spectra below GM76 levels are anticipated by the model. The observed Φ_{Fr} begin their steeper rolloff near the projected $k_c > 0.1$ cpm (Figure 6.4). Spectra are higher than expected at low wavenumbers, with $\overline{\Phi}_{\mathrm{Fr}} = 1.26\phi_{\mathrm{Fr}c}$ and $\overline{\Phi}_{\mathrm{Fr}} = 1.35\phi_{\mathrm{Fr}c}$ for combined fluctuating and total spectra, respectively. The excess variance yields $\varepsilon_{\mathrm{iwP}}$ that are around twice the observed dissipation (Figure 5.10).

The steep rolloff of Φ_{Fr} is reminiscent of spectra from weakly diffusive waters in the Equatorial Pacific [*Gregg et al.*, 1996]. Unlike the core spectra, those near the Equator rise well above the GM76 plateau before descending. Other steep rolloffs are observed in a moderately diffusive warm core ring [*Polzin et al.*, 1995] and in energetic near-inertial currents [*Duda and Cox*, 1989].

6.3.4 East channel wall

The four intervals of weak to moderate K_ρ yield Φ_{Fr} and Φ_{St} similar to those in the interior (Figure 6.3). The other four intervals—from middepths during the second occupation and from the TSBL—yield spectra similar to those of the turbulent high mean shear zones (HMSZs).

The turbulent intervals suffer from the limitation that their spectra cannot resolve the modeled low wavenumber plateau preceding $k_c < 0.02$ cpm (Figure 6.4). Again, k_c are overestimated by $Fr'^2 = 0.7$ (or $Fr^2 = 0.7$), and the flawed $\varepsilon_{\mathrm{iwP}}$ tend to fall short of observed ε (Figure 5.10). The exception is the middepth interval of $K_\rho \approx 1.4 \times 10^{-4}$ m^2 s^{-1}, where spectral resolution is marginal. Recall that in the other middepth interval, an isolated vigorous event dominates the mean turbulent profiles. Unlike the HMSZs, the three outliers here are not acceptably estimated by use of spatially computed variance (via $\varepsilon_{\mathrm{iwG}}$).

Fluctuating Φ_{Fr} from the less diffusive intervals are below their projected levels, with $\overline{\Phi}_{\mathrm{Fr}} = 0.71\phi_{\mathrm{Frc}}$; total Φ_{Fr} yield $\overline{\Phi}_{\mathrm{Fr}} = 0.88\phi_{\mathrm{Frc}}$ (Figure 6.4). However, if frequency content near the east wall is higher than in GM76, then $\gamma > 1$ in (6.2), which raises k_c and lowers ϕ_{Frc}.

6.3.5 Implications of the model comparison

The comparison of modeled and observed Froude spectra demonstrates why the $\varepsilon_{\mathrm{iwP}}$ scaling is reasonably successful in the interior, in the current core, and sometimes near the east wall. Finescale spectra adequately resolve the variance required by the parameterization to estimate dissipation. Generally, total Φ_{Fr} are as good a match as fluctuating Φ_{Fr} to model spectra projected from observed ε and N.

In some cases, it is more difficult to determine the value of k_c such that the

model spectrum is an appropriate representation of the the measured finescale field. For instance, isolation of regions of strong turbulence or high mean shear requires spectral windows that are too small to capture important contributions from larger scale shear. The spatial approach employed for ε_{iwG} is a useful alternative, and it does provide decent estimates of dissipation in the high mean shear zones—but only when total rather than fluctuating variance is considered.

The processes driving turbulence in some portions of the current probably differ from the internal wave interactions assumed by the model of *Henyey et al.* [1986]. It is not surprising that ε_{iwP} fails to predict dissipation rates in the TSBL of station 7. It is surprising that ε_{iwP} (or ε_{iwG}) yields close estimates of dissipation in the high mean shear zones, including the TSBL of station 3. Although the dynamics may not correspond to those in the model, they apparently result in similar dissipation rates and spectral forms.

Chapter 7

INTERNAL WAVE PROPAGATION: INFERENCES FROM CROSS SPECTRA

The internal wave field in the Florida Current differs in composition from that in the open ocean. Regions in Figure 5.5 with the greatest imbalances of clockwise-to-anticlockwise and across-to-along-channel shear variance contain velocity and density perturbations consistent with internal waves propagating in preferred directions. Figure 7.1 shows the two most typical behaviors. Between 4.5 MPa and 5.8 MPa in the upper panel, the fluctuating Froude vector rotates clockwise with depth, with its along-flow (north) component mirroring finescale strain; this combination suggests distortion of the background shear by a westward travelling wave. Between 0.5 MPa and 1.5 MPa in the lower panel, Froude fluctuations alternate from westward to eastward, suggestive of a higher-frequency wave propagating almost normal to the steep east bank. The following analysis supports these interpretations by contrasting measured Froude-strain cross spectra to those anticipated by Appendix C.

7.1 Measured Cross Spectra

Coherent features such as those in Figure 7.1 appear in much of the Florida Straits dataset, but their wavelengths, locations, and degrees of coherence vary from drop to drop. Station cross spectra provide a statistical description of tendencies that deviate most significantly from open ocean internal waves. Velocity

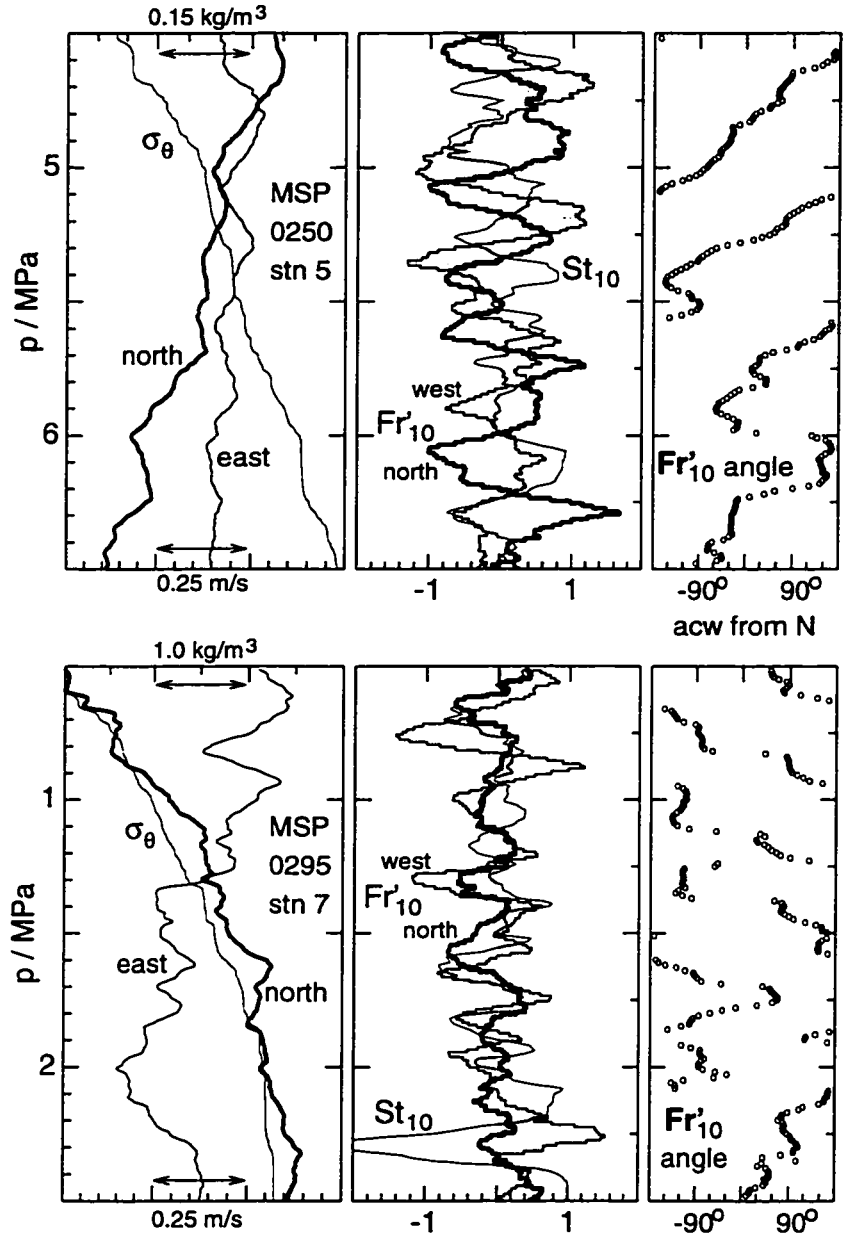

Figure 7.1: Profiles of density and velocity, and of 10-m strain and fluctuating Froude components. Top panel is for drop 0250 in the interior. Bottom panel is for drop 0295 near the east wall. Froude coordinates (north and west) correspond to the flow frame of Appendix C. Direction of Froude vector is plotted in degrees, anticlockwise from North.

or Froude cross spectra reflect attributes noted in the sample profiles or presented as component ratios in Figures 5.5 and 5.12c,d. For an interior interval deep at midchannel, Figure 7.2 shows that clockwise dominance is broadbanded, though concentrated near the 0.03-cpm peak where coherence is highest. In the current-core interval, the greatest clockwise excesses occur at the spectral peaks. The station 7 cross spectrum shows the eastward Froude dominance that distinguishes the east wall from the other regimes. In all these cases, Froude components converge at higher wavenumbers, sometimes well into the spectral rolloff.

Significant coherence between strain and northward Froude fluctuations occurs throughout the central and eastern interior. Figure 7.3 shows the predominant tendency of phase differences indistinct (at 95% confidence) from 180°, consistent with the upper profiles of Figure 7.1. For this interval, strain is also coherent with eastward Froude at 0.03 cpm, where strain lags by 90°.

To better envision the finestructure reflected in the cross spectra, Froude-strain ellipses are constructed from the measured phase and amplitude relations. Comparison to ellipses anticipated for propagating internal waves of various frequencies and flow orientations (Figure C.4) yields insight into the observed behaviors.

7.2 Froude-Strain Ellipses

Ellipses are formed for fluctuations in four wavenumber bands. Cross spectra are computed on 120-m intervals rather than on the mixing regime intervals employed earlier. The first estimates (at 1/120 cpm) are discarded, and then Fourier components for each two of the subsequent estimates are band-averaged before cross spectra and confidence limits are computed. The result is coherence and phase in four bands, each 0.0167-cpm wide, centered at 0.02083, 0.0375, 0.05417

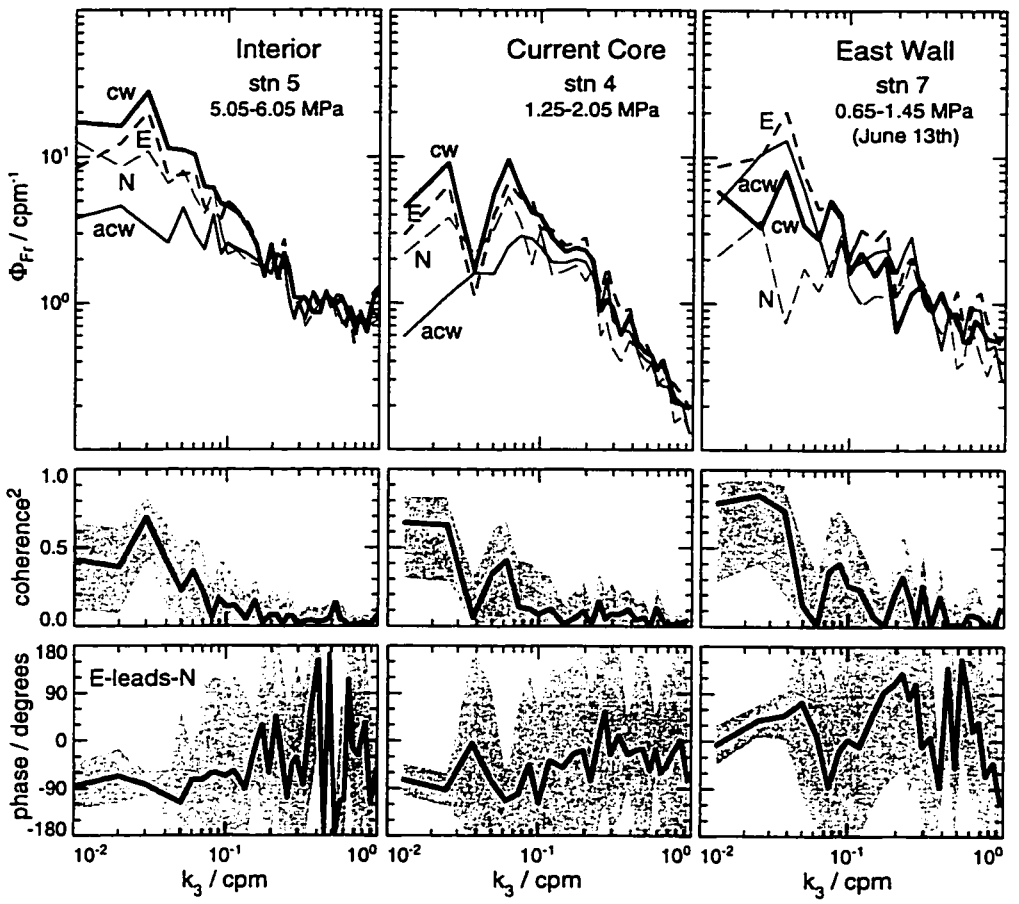

Figure 7.2: Rotary and Cartesian components for three of the fluctuation Φ_{Fr} highlighted in Figure 6.3. Lower panels show squared coherence and phase lead (with depth) of east shear to north, shaded at 95% confidence limits.

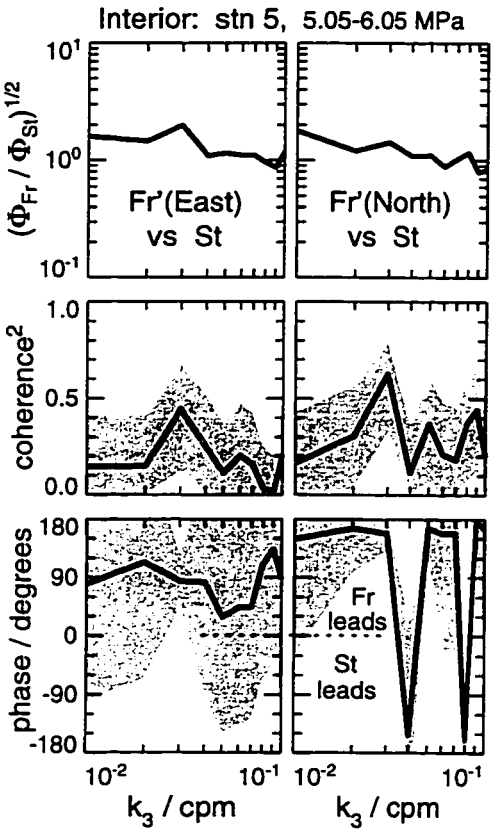

Figure 7.3: Cross spectra of east and north Froude fluctuations to strain for the same interior interval as in Figure 7.2. Froude-to-Strain amplitude ratios are in the upper panels, squared coherence and phase, shaded at 95% confidence limits, are in the lower panels.

and 0.07083 cpm. The combination of thicker intervals and band averaging enhances coherence in some places and dilutes it in others. However, the general conclusions of this chapter are not sensitive to how intervals are chosen or to particulars of the spectral processing.

Figure 7.4 represents all intervals and wavebands that have significant coherences among two or more pairs of Froude and strain perturbations. Most often, these are (1) the two Froude components and (2) strain and northward Froude. Strain and eastward Froude are sometimes coherent, either in addition to the two just noted (as at 0.03 cpm in the interior example from station 5) or in place of one of them. One wave variable—typically strain—is assigned a cosine profile, from which the other two—north and east Froude—are computed by applying spectral amplitude ratios and the most significant phase offsets. Some wavebands near the east wall have little to no strain coherence, but their ellipses are included to contrast with the interior ones; for these, one Froude component is computed from the other. Ellipses trace the depth progression of spectrally-determined Froude vectors, which rotate clockwise in all cases but one. When there is strain coherence, ellipses are green (red) where strain is within 45° of its maximum (minimum) value. Ellipses are scaled such that their major-axis lengths indicate relative Froude spectral levels.

There are three main points regarding the coherence patterns in Figure 7.4: First, there are no coherent intervals for stations 1 and 2; second, ellipses at station 7 are narrower than elsewhere; third, coherence is more prevalent deep in midchannel. Inadequate sampling, unreliable strain estimates, and the offshore shifting of the current diminish the ability to resolve coherent tendencies—if any exist—at the two western stations. Finescale perturbations near the steep eastern wall demonstrate topographic effects, while those in midchannel have some relation to the mean shear field (Figure 7.5).

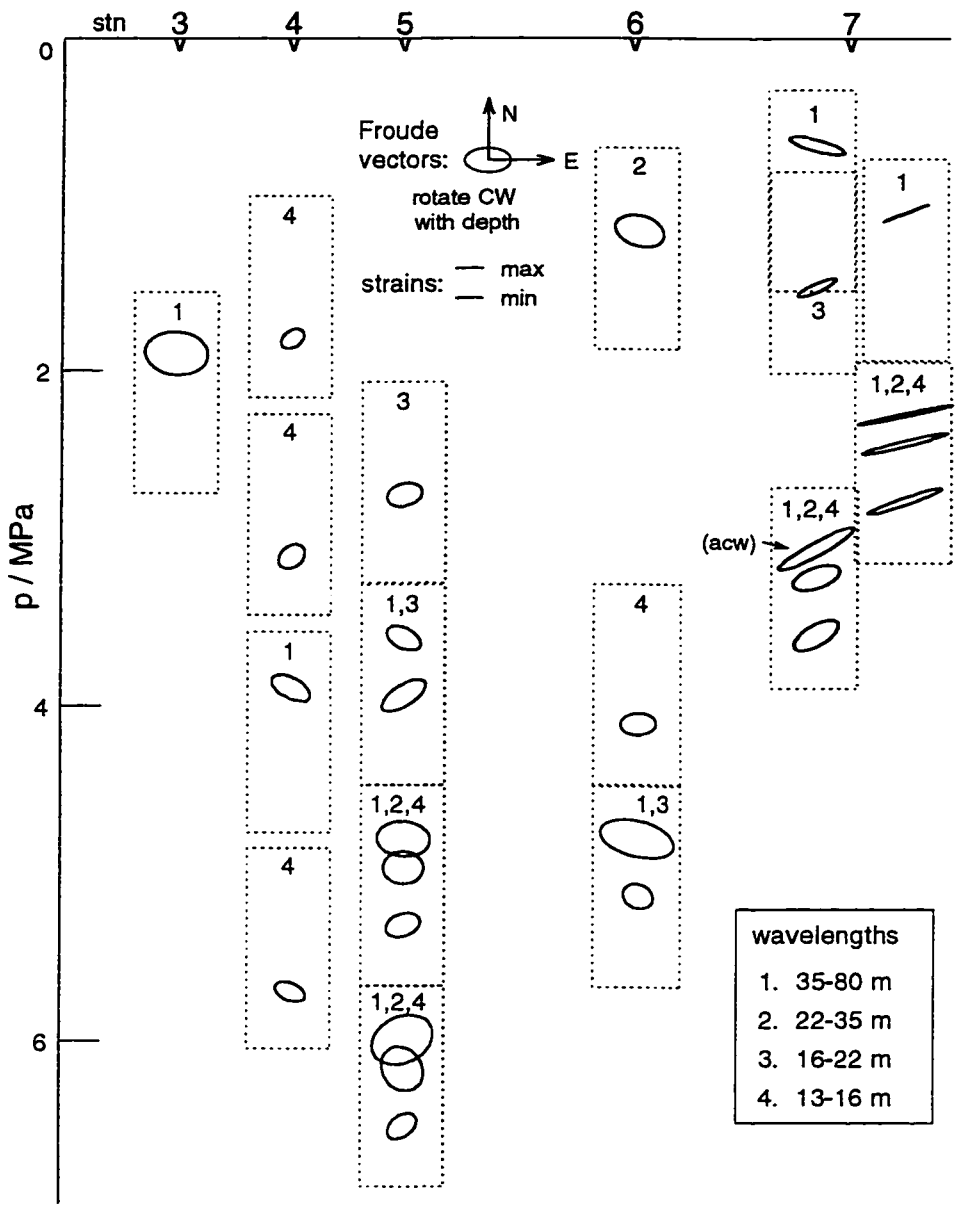

Figure 7.4: Ellipses for depth progression of Froude perturbations, based on east-to-north ratios and phase lags computed on four wavenumber bands from 120-m cross spectra. All but one rotate clockwise with depth. Longer major axes indicate higher Froude spectra levels (the shortest are near GM76). Most include significant $Fr-St$ coherence: Strain extrema are color coded to show phase relation with Froude vector. Locations within mean shear field are shown in Figure 7.5.

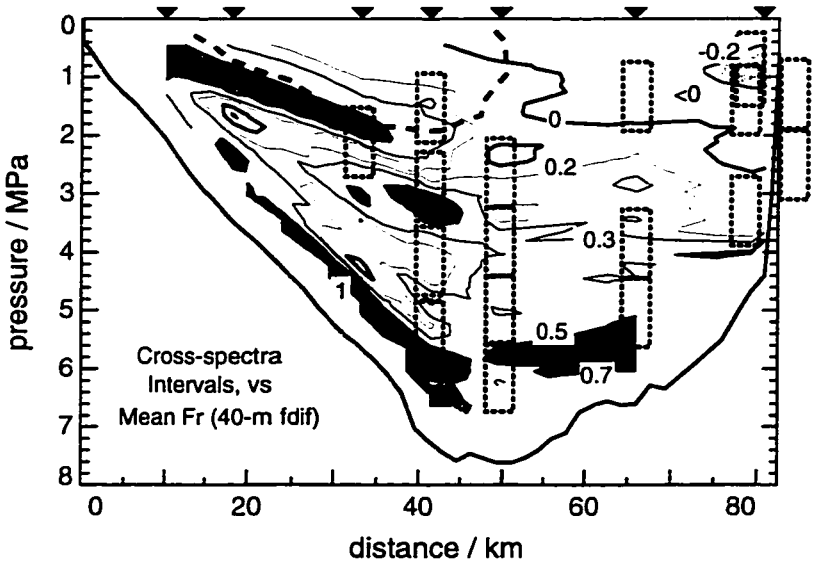

Figure 7.5: Cross-spectral intervals with significant coherence among Froude and strain fluctuations, outlined atop contours of background Froude of 40-m first-differenced mean north shear. Intervals for earlier drops at station 7 are left of those for later drops. Ellipses computed from cross spectra appear on Figure 7.4.

7.2.1 Interior: mean-shear distortion

Attributes described for the interior profiles of Figure 7.1 and cross spectra of Figures 7.2 and 7.3 are apparent in all ellipses of stations 3 through 6. Froude vectors rotate clockwise with depth, with northward components nearly 180° out of phase with strain. Orientations of major axes vary, but most are more across-flow than along-flow. Ratios of major-to-minor axes vary from about 2.5 to 1.2, which would indicate frequencies of $2.5f$ to $1.2f$ for narrow-banded internal waves propagating through a still background. However, multiple waves likely contribute signals—some more coherent than others—to each cross-spectral estimate, and, more important, the background has considerable shear.

An internal wave of any horizontal azimuth distorts the mean vertical shear, inducing along-flow velocity perturbations that—for positive shear—are nega-

tively correlated to vertical displacement [*Eriksen*, 1985; *Boyd et al.*, 1993]. These perturbations combine with the along-flow velocity fluctuation of the wave to alter the observed current ellipse. The outcome depends on the strength of the mean shear, Fr, and on the wave's frequency, σ, and direction of propagation, φ, as described in Appendix C. Relative contributions scale as $|\mathrm{Fr}\sin\varphi|$ from the mean shear versus f/σ from the wave, so cross-flow, higher-frequency waves are the most affected. Note that Froude-strain phase relations (i.e., ellipses) are equivalent to their velocity-displacement counterparts for narrow-banded linear internal waves.

If the interior ellipses of Figure 7.4 were in a non-sheared background ($\mathrm{Fr}=0$), they would be most consistent with lower-frequency internal waves of upward phase, propagating toward the west side of the channel ($\varphi\approx 90°$). Other waves are contrary in at least one regard (Figure C.4a): Eastward and upward have strain at the opposite phase; eastward and downward rotate anticlockwise; westward and downward are inconsistent in both respects; those propagating nearer the flow direction have strains that are $\pm 90°$ off, and their major axes are more along-flow.

When mean shear is present, even a wave with downward phase can exhibit the observed rotary and strain attributes, provided its frequency is high enough and its direction tends toward the west (Figure C.4b,c). Upward-phased waves achieve more circular rotation if westward, while eastward ones with higher σ or within stronger Fr appear to rotate anticlockwise. If $\sigma > f/\mathrm{Fr}$, both eastward and westward waves induce the observed mirroring of strain and northward Froude. Thus, given the higher Fr deep in midchannel (Figure 7.5), there is a broader frequency range of cross-channel waves that can contribute to the more prevalent strain coherence found there. Still, a preference for westward propagation is required to maintain the clockwise dominance, which is also enhanced in this

region (Figure 5.5).

The energy content at the observed vertical scales of 10 m to 100 m is a small part of the wave field's total, but these results do demonstrate anisotropy and asymmetry in the spectral band relevant to the finescale dissipation scalings. Furthermore, coherences are found even at wavenumbers well into the Froude spectral rolloff.

7.2.2 East channel wall: high-frequency waves

The narrower ellipses at station 7 provide further evidence that higher-frequency internal waves enhance shear variance near the east wall (Figure 7.4). Cross-channel propagation is indicated by the directions of the major axes (compare Figure C.4c), but coherences are too weak to distinguish onshore or offshore tendencies. Rotation of either sign is found in short segments of individual profiles—such as in Figure 7.1—but neither direction is dominant.

The deepest interval extends to the base of the wall, so most of it is in the turbulent stratified boundary layer (TSBL). As discussed in Chapter 5 while considering shear-component ratios in Figure 5.12cd, there is more rotation with depth here than in the overlying waters. However, for this 120-m interval, the lowest waveband exhibits anticlockwise rotation.

7.3 Discussion

Coherent features in finescale profiles of strain and shear perturbations are consistent with propagating internal waves interacting with the background environment. In midchannel, distortion of the mean shear by an anisotropic wave field can account for the excess of clockwise fluctuating shear and the 180° phase difference between its northward component and strain. Near the east wall, near-

critical reflection off the steep slope is a possible explanation for the dominance of cross-channel fluctuating shear and the low shear-to-strain ratios. There is no evidence of critical layers in the mean shear or of bottom-generated waves.

Cross spectra of shear and strain in midchannel share some characteristics of velocity-temperature time series collected within deep mean shear zones in the equatorial Pacific. For fluctuations at internal wave frequencies, *Eriksen* [1985] reports that current ellipses are oriented across the flow and that zonal (along-flow) current and temperature are coherent, with phases near—but significantly different from—0° or 180°. Furthermore, cross-flow kinetic energy exceeds along-flow, but there is no coherence between velocity components. Consistent with these observations is distortion of the mean shear by an anisotropic wave field, with across-flow waves more energetic than along-flow and with asymmetry in along-flow waves, that is, a westward-to-eastward imbalance [*Eriksen*, 1985]. Depletion of along-flow waves by critical layers is offered as an explanation for the inferred anisotropy.

The coherence between fluctuating shear or Froude components leads to a different characterization of the anisotropic wave field distorting the Florida Current shear. The asymmetry is instead in the cross-flow waves, with excess shear variance propagating westward. Unlike the equatorial case, the mean-shear perturbation can reduce along-flow velocity in some near-inertial waves, rather than just adding to that component. However, the general excess of cross-flow to along-flow variance is—again—probably due to depletion of along-flow waves by critical layers upstream. Another distinction involves upward versus downward waves. Energy at the equatorial moorings is assumed to come from above (upward phase), owing to the decay of kinetic energy with depth [*Eriksen*, 1985]. However, it is possible that higher-frequency waves carrying variance upward and toward the west contribute to the observed coherence patterns in the Florida Current.

Such waves could be generated, scattered, or reflected from the bottom.

Observations at Fieberling Guyot provide a contrast for those near the east wall. Signatures of near-critical reflection are sought by *Toole et al.* [1997] from profiler measurements and by *Eriksen* [1998] from closely spaced moored instruments. The critical frequency on the seamount's flank is around $0.5N$, a bit higher than that at the east wall of $(0.1\text{–}0.3)N$. *Toole et al.* [1997] do observe low shear-to-strain ratios and elevated spectral levels suggestive of near-critical enhancement, but cross-slope shear variance is essentially the same as along-slope. Near the critical frequency, moored velocity spectra are elevated, moreso than shear spectra (determined from current meters separated by 10 m). The enhanced energy seems to come from waves of great vertical wavelength, rather than from the anticipated shorter waves [*Eriksen*, 1998]. In contrast, finescale shear near the east wall does exhibit cross-slope enhancement at wavelengths of 10 m to 100 m, as shown in Figure 7.4. While suggestive of near-critical reflection, the profile data are inconclusive without support from time-series measurements.

Chapter 8

SUMMARY

The primary goal of this study is to examine how a steady mean shear affects internal waves and turbulent production. The motivation is to test existing parameterizations that have used finescale shear measurements to estimate viscous dissipation rates to within a factor of two in diverse open ocean settings. In an environment with mean shear, is the validity of the parameterizations limited owing to changes in the turbulent cascade through internal wave scales?

The Florida Current is a natural laboratory suited to this investigation. The structure and variability of the flow have been characterized by previous field programs, particularly where it passes through an 80-km wide channel between Florida and the Little Bahama Bank at 27°N. The Multi-Scale Profiler sampled finestructure and turbulent fluctuations at seven stations across the channel to encounter a range of mean shear conditions.

Reporting the levels and patterns of internal wave activity and mixing at this site is important in its own right, given the role of the Florida Current in ocean circulation. The observations suggest five contrasting regimes, four of which are associated with specific regions in the flow: the current core, high mean shear zones (HMSZs), the east wall, and turbulent stratified boundary layers (TSBLs). The fifth is designated the interior, which encompasses most of the channel. Each regime has attributes related to mean shear, finescale variance, turbulent mixing, or their interrelations that distinguish it from the others. The regimes provide a useful framework for further discussion.

8.1 Florida Current Characteristics

Mixing in the Florida Current is moderately strong by oceanic standards. Averaged over all regimes, $K_\rho = 6.7 \times 10^{-5}$ m^2 s^{-1}, which is a decade higher than the background level associated with the quiet midlatitude pycnocline. Stronger turbulence averaging 4.2×10^{-4} m^2 s^{-1} is found in the TSBLs, which lie within 10 m to 100 m of the channel bottom and account for only 7% of the total record; 4.0×10^{-5} m^2 s^{-1} is the average over the remaining 93%. The current core mixes weakly, at the ocean background level. Elsewhere, K_ρ is $(0.7-7.0) \times 10^{-5}$ m^2 s^{-1}, although it sometimes exceeds 10^{-4} m^2 s^{-1} near the east wall and in transient highly-sheared zones on the west side.

Mean shear is highest in the HMSZ west of the core near the surface, but it is stabilized by strong stratification such that $Fr^2 = 0.4$. Similar moderate Fr^2 occur deep in midchannel, immediately under the core, and in the TSBL at the base of the east wall. Midchannel mean Fr^2 weaken toward the surface. Only in the transient HSMZ and in the TSBL beneath the core is $Fr^2 > 1$—sites of the strongest mixing.

Internal waves are 1 to 4 times the GM76 background, based on fluctuating Froude variance and spectra. Minima occur in the core and the upper east wall. Higher values are from interior waters under the core and deep in midchannel. Decomposition into mean and fluctuations is uncertain west of the core because the current shifted offshore during sampling. Cross-channel variance generally exceeds along-channel, especially at the east wall where it is 3 to 4 times higher. Clockwise variance exceeds anticlockwise almost everywhere, by factors of 3 to 4 in the core and 2 to 4 deep in midchannel. Fluctuating Fr^2 is more than 3 times mean Fr^2 in most of the interior, although it is only 1.5 to 2 times higher where mean $Fr^2 > 0.3$. Only in the HSMZs does mean Fr^2 exceed fluctuating.

Coherent features in shear and strain profiles or cross spectra indicate interactions of internal waves with the mean shear or the east wall. Mirroring in midchannel of along-flow shear perturbations by strain is consistent with distortion of the mean shear by internal wave displacements. This distortion can reverse the apparent sense of rotation of an internal wave's velocity vector, depending on the wave's frequency and direction. Because the dominant sense of rotation is clockwise—especially deeper where mean shear is stronger—this suggests an anisotropic wave field with excess westward propagation. The alignment of narrow shear ellipses across the channel near the steep east wall suggests near-critical reflection of higher-frequency internal waves.

8.2 Finescale Production of Turbulence

The finescale parameterizations successfully estimate the observed dissipation for most of this dataset, provided that mean shear is accounted for in a simple way. By using total Froude variance or spectra rather than fluctuating, the contribution of mean shear is included. For the *Polzin et al.* [1995] formulation, one must determine the wavenumber at which the accumulated Froude variance reaches 0.7; this is where the spectral rolloff occurs that corresponds to the start of the instability range. The mean shear simply supplements the background otherwise provided by larger-scale waves, thereby moving the rolloff to a lower wavenumber (and higher spectral level) to elevate the resulting turbulent dissipation.

The validity of the parameterization is tested from two directions. First, dissipation rates estimated from finescale shear are compared to those observed. Second, Froude spectra projected from measured dissipation rates are compared to the observed low-wavenumber band. This spectral comparison can help to explain poorly estimated dissipation rates (i.e., when they are over a factor of

2 off). Disagreement can occur if (1) dissipation is driven by dynamics outside the scope of the modeled turbulent cascade, or (2) uncertainty in the measurements or sampling or shortcomings in the parameterization's methodology lead to inadequate resolution of the required finescale variance.

The good agreement of dissipation rates and Froude spectra in the interior and in the less turbulent waters near the east wall suggests that the parameterization remains valid for environments with moderately strong mean shear—or, for anisotropic or asymmetric internal wave fields. In these cases, the use of total versus fluctuating variance leads to little difference in the dissipation estimate, and, conversely, there is little difference between total and fluctuating Froude spectra. This is because mean shear contributes less to the total variance than fluctuating shear does. Another factor in favor of successful estimation of these dissipation rates is that the associated turbulent diffusivities are low to moderate rather than high.

For the current core, dissipation is slightly overpredicted by peaked Froude spectra that roll off more steeply than the canonical form. If the wave field is relatively narrow-banded, interactions and downscale transfer may be slower than in a more broad-banded spectrum. Spectra from weakly diffusive waters in the equatorial Pacific also peak before steeply rolling off, but there, the finescale variance is much higher than expected for the low dissipation rates.

Spectral determination of the required finescale shear variance can be problematic when estimating dissipation rates in regions of strong turbulence or high mean shear that are limited in extent. Isolation of such features requires spectral windows that are too small to capture important contributions from larger-scale shear. If the measured Froude spectrum rolls off near its first estimate (at its fundamental wavenumber), then integration to 0.7 will yield an overestimate of the cutoff wavenumber and, consequently, an underestimate of dissipation. If a spec-

trum does resolve the rolloff, but does not resolve shear contributions from scales larger than the feature—such as in the upper, less turbulent HMSZs—dissipation will also be underestimated. Spatial computation of shear variance can provide a better estimate in such cases. Optimally, the resulting variance should be matched to the model Froude spectrum—identified by its cutoff wavenumber—that yields that same variance when subjected to the chosen spatial filtering.

BIBLIOGRAPHY

Atkinson, L. P., T. Berger, P. Hamilton, E. Waddell, K. Leaman, and T. N. Lee, Current meter observations in the Old Bahama Channel, *J. Geophys. Res.*, *100*, 8555–8560, 1995.

Blumenthal, M. B., and M. G. Briscoe, Distinguishing propagating waves and standing modes: An internal wave model, *J. Phys. Oceanogr.*, *25*, 1095–1115, 1995.

Booker, J. R., and F. P. Bretherton, The critical layer for internal gravity waves in a shear flow, *J. Fluid Mech.*, *27*, 513–539, 1967.

Boyd, T. J., D. S. Luther, R. A. Knox, and M. C. Hendershott, High-frequency internal waves in the strongly sheared currents of the upper equatorial Pacific: Observations and a simple spectral model, *J. Geophys. Res.*, *98*, 18,089–18,107, 1993.

Cairns, J. L., and G. O. Williams, Internal wave observations from a mid-water float, 2, *J. Geophys. Res.*, *81*, 1943–1950, 1976.

Calman, J., On the interpretation of ocean current spectra. Part I: The kinematics of three-dimensional vector time series, *J. Phys. Oceanogr.*, *8*, 627–643, 1978a.

Calman, J., On the interpretation of ocean current spectra. Part II: Testing dynamical hypotheses, *J. Phys. Oceanogr.*, *8*, 644–652, 1978b.

Desaubies, Y. J. F., Internal waves near the turning point, *Geophys. Fluid Dyn.*, *5*, 143–154, 1973.

Duda, T. F., and C. S. Cox, Vertical wave number spectra of velocity and shear at small internal wave scales, *J. Geophys. Res.*, *94*, 939–950, 1989.

Eriksen, C. C., Observations of internal wave reflection off sloping bottoms, *J. Geophys. Res.*, *87*, 525–538, 1982.

Eriksen, C. C., Some characteristics of internal gravity waves in the equatorial Pacific, *J. Geophys. Res.*, *90*, 7243–7255, 1985.

Eriksen, C. C., Internal wave reflection and mixing at Fieberling Guyot, *J. Geophys. Res.*, *103*, 2977–2994, 1998.

Fofonoff, N. P., Spectral characteristics of internal waves in the ocean, *Deep-Sea Res.*, *16*(Suppl.), 59–71, 1969.

Gargett, A. E., Do we really know how to scale the turbulent kinetic energy dissipation rate ϵ due to breaking of oceanic internal waves?, *Deep-Sea Res.*, *95*, 15,971–15,974, 1990.

Gargett, A. E., P. J. Hendricks, T. B. Sanford, T. R. Osborn, and A. J. Williams, III, A composite spectrum of vertical shear in the upper ocean, *J. Phys. Oceanogr.*, *11*, 1258–1271, 1981.

Garrett, C., and W. Munk, Space-time scales of internal waves, *Geophys. Fluid Dyn.*, *2*, 225–264, 1972.

Garrett, C. J. R., and W. H. Munk, Space-time scales of internal waves: A progress report, *J. Geophys. Res.*, *80*, 291–297, 1975.

Gill, A. E., *Atmosphere-Ocean Dynamics*, Academic Press, 1982.

Gonella, J., A rotary-component method for analyzing meteorogical and oceanographic vector time series, *Deep-Sea Res.*, *19*, 833–846, 1972.

Gregg, M. C., Variations in the intensity of small-scale mixing in the main thermocline, *J. Phys. Oceanogr.*, *7*, 436–454, 1977.

Gregg, M. C., Diapycnal mixing in the thermocline: A review, *J. Geophys. Res.*, *92*, 5249–5286, 1987.

Gregg, M. C., Scaling turbulent dissipation in the thermocline, *J. Geophys. Res.*, *94*, 9686–9698, 1989.

Gregg, M. C., and E. Kunze, Shear and strain in Santa Monica Basin, *J. Geophys. Res.*, *96*, 16,709–16,719, 1991.

Gregg, M. C., and T. B. Sanford, Signatures of mixing from the Bermuda Slope, the Sargasso Sea and the Gulf Stream, *J. Phys. Oceanogr.*, *10*, 105–127, 1980.

Gregg, M. C., and T. B. Sanford, The dependence of turbulent dissipation on stratification in a diffusively stable thermocline, *J. Geophys. Res.*, *93*, 12,381–12,392, 1988.

Gregg, M. C., D. P. Winkel, and T. B. Sanford, Varieties of fully resolved spectra of vertical shear, *J. Phys. Oceanogr.*, *23*, 124–141, 1993.

Gregg, M. C., D. P. Winkel, T. B. Sanford, and H. Peters, Turbulence produced by internal waves in the oceanic thermocline at mid and low latitudes, *Dyn. Atmos. Oceans*, *24*, 1–14, 1996.

Henyey, F. S., J. Wright, and S. M. Flatté, Energy and action flow through the internal wave field, *J. Geophys. Res.*, *91*, 8487–8495, 1986.

Johnson, C. L., and T. B. Sanford, Anomalous behavior of internal gravity waves near Bermuda, *J. Phys. Oceanogr.*, *10*, 2021–2034, 1980.

Jones, W. L., Propagation of internal gravity waves in fluids with shear flow and rotation, *J. Fluid Mech.*, *30*, 439–448, 1967.

Kunze, E., Near-inertial wave propagation in geostrophic shear, *J. Phys. Oceanogr.*, *15*, 544–565, 1985.

Kunze, E., A. J. Williams, III, and M. G. Briscoe, Observations of shear and vertical stability from a neutrally buoyant float, *J. Geophys. Res.*, *95*, 18,127–18,142, 1990.

Kunze, E., R. W. Schmitt, and J. M. Toole, The energy balance in a warm-core ring's near-inertial critical layer, *J. Phys. Oceanogr.*, *25*, 942–957, 1995.

Larsen, J. C., and T. B. Sanford, Florida Current volume transports from voltage measurements, *Science*, *227*, 302–304, 1985.

Leaman, K. D., Observations on the vertical polarization and energy flux of near-inertial waves, *J. Phys. Oceanogr.*, *6*, 894–908, 1976.

Leaman, K. D., and R. L. Molinari, Topographic modification of the Florida Current by Little Bahama and Great Bahama Banks, *J. Phys. Oceanogr.*, *17*, 1724–1736, 1987.

Leaman, K. D., and T. B. Sanford, Vertical energy propagation of inertial waves: A vector spectral analysis of velocity profiles, *J. Geophys. Res.*, *80*, 1975–1978, 1975.

Leaman, K. D., and T. B. Sanford, Observations on the vertical polarization and energy flux of near-inertial waves, *J. Geophys. Res.*, *6*, 894–908, 1976.

Leaman, K. D., R. L. Molinari, and P. S. Vertes, Structure and variability of the Florida Current at 27°N: April 1982–July 1984, *J. Phys. Oceanogr.*, *17*, 565–583, 1987.

Leaman, K. D., P. S. Vertes, L. P. Atkinson, T. N. Lee, P. Hamilton, and E. Waddell, Transport, potential vorticity, and current/temperature structure across Northwest Providence and Santaren Channels and the Florida Current off Cay Sal Bank, *J. Geophys. Res.*, *100*, 8561–8570, 1995.

Ledwell, J. R., A. J. Watson, and C. S. Law, Tracer dispersion during the North Atlantic Tracer Experiment (NATRE), in *EOS*, p. 75s: 121, Amer. Geophys. Union, 1994.

Lee, C. M., and C. C. Eriksen, Near-inertial internal wave interactions with mesoscale fronts: Observations and models, *J. Geophys. Res.*, *102*, 3237–3253, 1997.

Lee, T. N., F. A. Schott, and R. J. Zantopp, Florida Current: Low-frequency variability as observed with moored current meters during April 1982 to June 1983, *Science*, *227*, 298–302, 1985.

Lien, R. C., M. J. McPhaden, and M. C. Gregg, High-frequency internal waves at 0°, 140° W and their possible relationship to deep-cycle turbulence, *J. Phys. Oceanogr.*, *26*, 581–600, 1996.

Molinari, R. L., et al., Subtropical Atlantic Climate Studies: Introduction, *Science*, *227*, 292–295, 1985a.

Mooers, C. N. K., A technique for the cross spectrum analysis of pairs of complex-valued time series, with emphasis on properties of polarized components and rotational invariants, *Deep-Sea Res.*, *20*, 1129–1141, 1973.

Moum, J. N., M. C. Gregg, R. C. Lien, and M. E. Carr, Comparison of turbulent kinetic energy dissipation rate estimates from two ocean microstructure profilers, *J. Atmos. Ocean. Tech.*, *12*, 346–366, 1995.

Munk, W. H., Abyssal recipes, *Deep-Sea Res.*, *13*, 707–730, 1966.

Munk, W. H., Internal waves and small-scale processes, in *Evolution of Physical Oceanography*, edited by B. A. Warren, and C. Wunsch, pp. 264–291, MIT Press, Cambridge, MA, 1981.

Oakey, N. S., Determination of the rate of dissipation of turbulent energy from simultaneous temperature and velocity shear microstructure measurements, *J. Phys. Oceanogr.*, *12*, 256–271, 1982.

Oakey, N. S., and J. A. Elliott, The variability of temperature gradient microstructure observed in the Denmark Strait, *J. Geophys. Res.*, *85*, 1933–1944, 1980.

Osborn, T. R., Estimates of the local rate of vertical diffusion from dissipation measurements, *J. Phys. Oceanogr.*, *10*, 83–89, 1980.

Osborn, T. R., and C. S. Cox, Oceanic fine structure, *Geophys. Fluid Dyn.*, *3*, 321–345, 1972.

Peters, H., M. C. Gregg, and J. M. Toole, On the parameterization of equatorial turbulence, *J. Geophys. Res.*, *93*, 1199–1218, 1988.

Peters, H., M. C. Gregg, and T. B. Sanford, The diurnal cycle of the upper equatorial ocean: Turbulence, fine-scale shear, and mean shear, *J. Geophys. Res.*, *99*, 7707–7721, 1994.

Peters, H., M. C. Gregg, and T. B. Sanford, On the parameterization of equatorial turbulence: Effect of fine-scale variations below the range of the diurnal cycle, *J. Geophys. Res.*, *100*, 18,333–18,348, 1995.

Polzin, K. L., J. M. Toole, and R. W. Schmitt, Finescale parameterization of turbulent dissipation, *J. Phys. Oceanogr.*, *25*, 306–328, 1995.

Polzin, K. L., N. S. Oakey, J. M. Toole, and R. W. Schmitt, Fine structure and microstructure characteristics across the northwest Atlantic Subtropical Front, *J. Geophys. Res.*, *101*, 14,111–14,121, 1996.

Schmitt, R. W., K. L. Polzin, and J. M. Toole, A comparison of direct turbulence measurements with tracer dispersion in the North Atlantic Tracer Release Experiment, in *EOS*, p. 75S: 130, Amer. Geophys. Union, 1994.

Schmitz, W. J., and P. L. Richardson, On the sources of the Florida Current, *Deep-Sea Res.*, *38 suppl.1*, 5379–5409, 1991.

Seim, H. E., and G. Gawarkiewicz, Stratified spin-up and benthic frontogenesis in a sloping channel, *J. Phys. Oceanogr.*, submitted, 1998.

Seim, H. E., D. P. Winkel, G. Gawarkiewicz, and M. C. Gregg, A benthic front in the Florida Straits and its relationship to the structure of the Florida Current, *J. Phys. Oceanogr.*, submitted, 1998.

Thorpe, S. A., The generation of internal waves by flow over the rough topography of a continental slope, *Proc. Roy. Soc. London A*, *439*, 115–130, 1992.

Thorpe, S. A., The cross-slope transport of momentum by internal waves generated by alongslope currents over topography, *J. Phys. Oceanogr.*, *26*, 191–204, 1996.

Toole, J. M., R. W. Schmitt, K. L. Polzin, and E. Kunze, Near-boundary mixing above the flanks of a midlatitude seamount, *J. Geophys. Res.*, *102*, 947–959, 1997.

Wesson, J. C., and M. C. Gregg, Mixing at Camarinal Sill in the Strait of Gibraltar, *J. Geophys. Res.*, *99*, 9847–9878, 1994.

Winkel, D. P., M. C. Gregg, and T. B. Sanford, Simultaneous observations of shear and turbulence in the Florida Current, in *AMS 10th Symposium on Turbulence and Diffusion, September 29–October 2, 1992, Portland, Oregon*, pp. (J5)101–(J5)104, 1992.

Winkel, D. P., M. C. Gregg, B. M. Bell, and T. B. Sanford, Resolving velocity profiles with the Multi-Scale Profiler, Technical Report APL-UW TR 9414,

Appl. Phys. Lab., Univ. of Wash., 1013 N.E. 40th Street, Seattle, WA 98105, 1994.

Winkel, D. P., M. C. Gregg, and T. B. Sanford, Resolving oceanic shear and velocity with the Multi-Scale Profiler, *J. Atmos. Ocean. Tech.*, *13*, 1046–1072, 1996.

Appendix A

NOTATION

Abbreviations

MSP	Multi-Scale Profiler
ACM	acoustic current meter
ECM	electromagnetic current meter
HBL	homogeneous boundary layer, at the bottom of the channel
SBL	surface boundary layer
TSBL	turbulent stratified boundary layer, directly above the HBL; if no HBL is present, TSBL extends to the bottom.
HMSZ	high mean shear zone

Operators

$\langle A \rangle$	time-mean profile of A, the average of A-profiles for a set of drops at an MSP station
$\tilde{A}$	indicates that a low-pass filter was applied to vertically smooth A
$\overline{A}$	arithmetic average of A over some vertical interval

Reference frame

x, y, z	east, north, and upward directions (Appendix C defines x and y differently, as streamwise coordinates)
p	pressure—in seawater, $\Delta z = 10$ m yields $\Delta p \approx 0.1$ MPa

Hydrography: density, displacement, strain

θ, S	potential temperature ($°C$) and salinity
σ_θ	potential density, $\sigma_\theta = \rho(S, \theta, 0 \text{ MPa}) - 1000 \text{ kg m}^{-3}$
$\langle\sigma_\theta\rangle$	station mean density profile; average σ_θ on pressure surface
σ'_θ	density fluctuation, $\sigma'_\theta = \sigma_\theta - \langle\sigma_\theta\rangle$
η_p	linear displacement, $\eta_p = -\sigma'_\theta/(d\langle\sigma_\theta\rangle/dz)$
$z(\sigma_\theta)$	depth of isopycnal, instantaneous
$\langle z(\sigma_\theta)\rangle$	station mean density profile; average depth of isopycnal
η_σ	isopycnal displacement, $\eta_\sigma = z(\sigma_\theta) - \langle z(\sigma_\theta)\rangle$
St_{10}	first-differenced strain, $St_{10} \equiv \Delta\eta_\sigma/\Delta z$, with $\Delta z = 10$ m
$\langle St_{10}^2\rangle$	variance of 10-m first-differenced strain (for station)

Buoyancy frequency

N_{10}^2	squared buoyancy frequency, computed with Fofonoff's method over intervals of $\Delta p = 0.1$ MPa centered every 5 kPa, then subsampled every 0.1 MPa
$\langle N_{10}^2\rangle$	station mean 0.1-MPa (10-m) N^2 profile
$\overline{\langle N_{10}^2\rangle}$	station average N^2 over designated interval
$\widetilde{N_{10}^2}$	smoothed N_{10}^2: running average of 5-kPa gridded N_{10}^2 is taken within 0.125-MPa intervals centered every 0.1 MPa
$\langle\widetilde{N_{10}^2}\rangle$	station smoothed-mean N^2 profile

Velocity and shear

u, v	east and north components of ocean velocity, as determined from ACM measurements
$\tilde{u}$, $\tilde{v}$	smoothed velocity: u and v filtered with a 0.22-MPa (22-m) Bartlett window and subsampled every 5 kPa (0.5 m)
$\langle\tilde{u}\rangle$, $\langle\tilde{v}\rangle$	smoothed mean velocity, representative of subinertial background flow
u', v'	fluctuation velocity: $u' = u - \langle\tilde{u}\rangle$ and $v' = v - \langle\tilde{v}\rangle$
S_{10x}, S_{10y}	total shear components: first differences $\Delta u/\Delta z$ and $\Delta v/\Delta z$ for $\Delta z = 10$ m, centered every 0.1 MPa
S'_{10x}, S'_{10y}	fluctuating shear components: 10-m first differences of u' and v' every 0.1 MPa
$\langle\tilde{S}_{10x}\rangle$, $\langle\tilde{S}_{10y}\rangle$	mean shear components: 10-m first differences of $\langle\tilde{u}\rangle$ and $\langle\tilde{v}\rangle$ every 0.1 MPa
S_{10}^2	square of total shear magnitude, $S_{10}^2 = S_{10x}^2 + S_{10y}^2$
$S_{10}'^2$	square of fluctuating shear magnitude, $S_{10}'^2 = S_{10x}'^2 + S_{10y}'^2$
$\langle\tilde{S}_{10}\rangle^2$	square of mean shear magnitude, $\langle\tilde{S}_{10}\rangle^2 = \langle\tilde{S}_{10x}\rangle^2 + \langle\tilde{S}_{10y}\rangle^2$
$\langle S_{10}^2\rangle$	variance of 10-m first-differenced total shear (for station)
$\langle S_{10}'^2\rangle$	variance of 10-m first-differenced fluctuating shear (for station)

Froude numbers

Fr_{10}^2	total 10-m squared Froude number; equals $S_{10}^2/\langle\widetilde{N_{10}^2}\rangle$
$Fr_{10}'^2$	fluctuating 10-m squared Froude number; equals $S_{10}'^2/\langle\widetilde{N_{10}^2}\rangle$
$\langle\widetilde{Fr}_{10}\rangle^2$	station mean squared Froude number; equals $\langle\tilde{S}_{10}\rangle^2/\langle\widetilde{N_{10}^2}\rangle$

Notation for further Froude components and station variances corresponds to shear counterparts

Dissipation and diffusivity

ε_{10} measured viscous dissipation rate, averaged within 10-m windows centered every 0.1 MPa (10 m)

K_ρ diapycnal diffusivity; equals $0.2\varepsilon_{10}/\langle N_{10}^2 \rangle$ for 0.1-MPa gridded drop profiles

$\varepsilon_{\mathrm{iwG}}$ dissipation scaling of *Gregg* [1989], based on 10-m first-differenced shear variance

$\varepsilon_{\mathrm{iwP}}$ dissipation scaling of *Polzin et al.* [1995], based on spectrally-integrated shear variance

Spectral quantities

k_3	vertical wavenumber, in cycles per meter (cpm)
Φ_{St}	strain spectrum
Φ_{Sh}	shear spectrum: sum of east and north Cartesian autospectra, $\Phi_{Shx}+\Phi_{Shy}$, or of clockwise and anticlockwise rotary components, $\Phi_{Shc}+\Phi_{Sha}$
Φ_{Fr}	Froude spectrum, computed $\Phi_{Fr} = \Phi_{Sh}/\overline{\langle N_{10}^2 \rangle}$
$St^2(k_{up})$	strain function: cumulative variance of Φ_{St} through $k_3 = k_{up}$
$S'^2(k_{up})$	shear function: cumulative variance of Φ_{Sh} (fluctuating) through $k_3 = k_{up}$; Cartesian components are $S_x'^2$ and $S_y'^2$, rotary ones are $S_{cw}'^2$ and $S_{acw}'^2$
$S^2(k_{up})$	shear function: cumulative variance of Φ_{Sh} (total) through $k_3 = k_{up}$
$Fr'^2(k_{up})$	Froude function: cumulative variance of Φ_{Fr} (fluctuating) through $k_3 = k_{up}$
$Fr^2(k_{up})$	Froude function: cumulative variance of Φ_{Fr} (total) through $k_3 = k_{up}$

Appendix B

GARRETT-MUNK VERTICAL WAVENUMBER SPECTRA

The conventional form is that presented in the appendix of *Gregg and Kunze* [1991],

$$\Phi_{\mathrm{ShGM}}(\beta) = \frac{3Eb^3N_0^2}{2j_*\pi}\,\frac{\beta^2}{(1+\beta/\beta_*)^2}\,C(\beta) \quad [\mathrm{s}^{-2}/\mathrm{rad\ m}^{-1}] \qquad \text{(B.1)}$$

with radian wavenumber β, dimensionless energy level $E = 6.3 \times 10^{-5}$, thermocline scale depth $b = 1300$ m, and reference buoyancy frequency $N_0 = 0.00524\,\mathrm{s}^{-1}$. Dependence of Φ_{ShGM} on N^2, the background stratification, arises from the bandwidth wavenumber $\beta_* = (\pi j_*/b)(N/N_0)$ when mode number j_* is fixed at 3 by convention. The spectral rolloff past $\beta_{c\mathrm{GM}} = 0.628$ rad m^{-1} is achieved by specifying $C(\beta) = 1$ for $\beta \le \beta_{c\mathrm{GM}}$ and $C(\beta) = \beta_{c\mathrm{GM}}\beta^{-1}$ for higher wavenumbers. Horizontal isotropy and vertical symmetry are assumed for wavenumber distribution, so each Cartesian and rotary spectral component is $0.5\,\Phi_{\mathrm{ShGM}}$.

The Froude spectrum

$$\Phi_{\mathrm{FrGM}}(\beta) = \frac{\Phi_{\mathrm{ShGM}}}{N^2} = \frac{3Eb\pi j_*}{2}\,\frac{1}{(1+\beta_*/\beta)^2}\,C(\beta) \quad [1/\mathrm{rad\ m}^{-1}] \qquad \text{(B.2)}$$

is nearly independent of N at high wavenumbers ($\beta \gg \beta_*$), especially in the rolloff beyond $\beta_{c\mathrm{GM}}$. For example, $\Phi_{\mathrm{FrGM}}(\beta_{c\mathrm{GM}})$ varies only as $N^{-0.04}$ from its nominal value of 1.13 rad^{-1} m at $N = N_0$. At low wavenumbers, Φ_{FrGM} rises approaching β_* and then nearly flattens toward $\beta_{c\mathrm{GM}}$; spectral shape and level vary somewhat

owing to the narrowing separation of β_* and $\beta_{c_{GM}}$ with increasing N. The Froude variance accumulated up to the rolloff varies as $N^{-0.11}$, with $Fr^2_{GM}(\beta_{c_{GM}}) = 0.667$ for $N = N_0$, 0.690 for $N = 0.003$ s^{-1}, and 0.574 for $N = 0.018$ s^{-1}. To ignore these weak dependencies on N, the approximate form

$$\Phi_{Fr_{GM}}(\beta) \approx \frac{1.11}{\text{rad m}^{-1}} C(\beta)$$

is sometimes assumed, with the result that $Fr^2_{GM}(\beta_{c_{GM}}) = 0.7$ regardless of N [*Polzin et al.*, 1995]; it is shown in Figure 5.6. The nominal value of $Fr^2_{10_{GM}} = 0.33$, reflecting 10-m first-differenced shear, is based on this approximation [*Gregg and Sanford*, 1988].

The GM76 strain spectrum is simply $\Phi_{St_{GM}}(\beta) = \frac{1}{3}\Phi_{Fr_{GM}}(\beta)$, with the same conventions or assumptions as for the Froude spectrum. The analytic forms of $\Phi_{Fr_{GM}}$ and $\Phi_{St_{GM}}$ are multiplied by 2π radians/cycle to plot spectra and wavenumbers ($k_3 = \beta/2\pi$) in terms of cycles per meter (cpm).

Appendix C

INTERNAL WAVE PERTURBATIONS IN VERTICAL SHEAR FLOWS

The motivation is to develop the proper interpretation for cross spectra of vertical variations in velocity and density as measured by profilers. Specifically, we derive the phase relations for fluctuations produced by linear internal waves propagating within a geostrophic, vertically sheared background flow.

Most of the oceanographic literature regarding cross spectra is oriented to time series. *Fofonoff* [1969] developed expressions from the internal wave equations, without mean flow, for comparison to mooring data. *Gonella* [1972] focussed on the rotary decomposition of horizontal velocity, with application within Ekman theory to coherence between wind and mixed layer current. *Mooers* [1973] studied rotary statistics of internal-wave frequency cross spectra. *Calman* [1978a, b] took a broader approach to representing spectra of vector time series and then illustrated the utility of selected representations in interpreting a variety of ocean dynamics. *Eriksen* [1985] formed cross spectra for collocated time series from an Equatorial mooring, and examined for various depths the effects of mean shear on internal wave kinematics and energy density components. *Blumenthal and Briscoe* [1995] investigated phase and coherence between vertically separated time series, under the assumption that the measured fluctuations are the sum, over all wavenumbers, of propagating and standing internal wave modes. Their results from data at large separations and high frequencies are contrasted to predictions

of the Garrett and Munk spectral models.

Regarding analysis of vertical fluctuations, *Leaman and Sanford* [1975] applied the rotary decomposition to profiles of horizontal velocity. Looking downward, they observed excess clockwise vs anticlockwise rotation of velocity vectors. Combined with the upward phase propagation apparent in their 5-day time series of profiles [*Leaman*, 1976], this polarized motion suggested downward travelling near-inertial energy. From profiles taken near Bermuda, *Johnson and Sanford* [1980] observed coherence between temperature and northward velocity in the wavelength band 30–50 m. They compared measured phase with that expected from the sum of two internal waves of equal horizontal, but opposite vertical, wavenumber components. They concluded that the data could represent energy propagating offshore and dominantly upward. The present analysis indicates that they misinterpreted the phase relations for the downward propagating component, although their basic conclusion may be valid. The conflict arises from a subtlety in the manner that downward- vs upward-phased waves project onto Fourier space.

C.1 Internal Wave Equations

Consider a steady background flow, $\mathbf{U}(z)$, that is vertically sheared, geostrophically balanced, and unidirectional. Internal waves propagating in such a flow yield perturbations that differ from those produced in an unsheared environment. The associated kinematics depend on the angle, φ, between $\mathbf{U}(z)$ and the horizontal wavevector, $\mathbf{k_h}$ (Figure C.1). Two reference frames are defined: The wave frame—aligned with $\mathbf{k_h}$—is better for analyzing and understanding the interaction of the flow with a single wave; the flow frame—aligned with $\mathbf{U}(z)$—is appropriate when considering combined effects of multiple waves of various

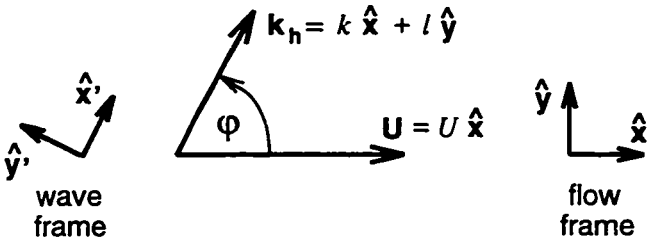

Figure C.1: Definition diagram relating wave frame to flow frame.

orientations and, therefore, when interpreting observations. Spatial location is expressed as $\mathbf{x_h} + z\hat{\mathbf{z}}$, with $\mathbf{x_h} = x'\,\hat{\mathbf{x}}' + y'\,\hat{\mathbf{y}}'$ in the wave frame and $\mathbf{x_h} = x\hat{\mathbf{x}} + y\hat{\mathbf{y}}$ in the flow frame. The horizontal unit vectors are related by

$$\begin{aligned} \hat{\mathbf{x}} &= \hat{\mathbf{x}}' \cos\varphi - \hat{\mathbf{y}}' \sin\varphi \\ \hat{\mathbf{y}} &= \hat{\mathbf{x}}' \sin\varphi + \hat{\mathbf{y}}' \cos\varphi \end{aligned}$$

and the vertical unit vector, $\hat{\mathbf{z}}$, points upward in both frames.

The background flow is expressed as

$$\mathbf{U}(z) \equiv U(z)\,\hat{\mathbf{x}} = U'\,\hat{\mathbf{x}}' + V'\,\hat{\mathbf{y}}'$$

where $U' = U\cos\varphi$ and $V' = -U\sin\varphi$. Negative values of $U(z)$ are permitted. Because $\mathbf{U}(z)$ is steady, $\partial_t \mathbf{U} \equiv \mathbf{U}_t = 0$, and because it is unidirectional, $U_x = 0$ and $U_y = 0$ (and $V = 0$). The background buoyancy and density fields are related by

$$B = -g\overline{\rho}/\rho_0 \qquad (\mathrm{m\ s^{-2}})$$

and so $B_z = N^2$. Furthermore, geostrophy implies $B_y = -fU_z$, $B_{x'} = fV'_z$, and $B_{y'} = -fU'_z$ (and $B_x = fV_z = 0$) by thermal wind. Note that $f < 0$ in the southern hemisphere.

Perturbations are denoted as $\mathbf{u}(\mathbf{x_h},z,t) = u\,\hat{\mathbf{x}} + v\,\hat{\mathbf{y}} = u'\,\hat{\mathbf{x}}' + v'\,\hat{\mathbf{y}}'$ for horizontal velocity, w for vertical velocity, ρ for density, $b = -g\rho/\rho_0$ for buoyancy, and p for reduced pressure (i.e., normalized by ρ_0). By definition, there are no cross-wavenumber fluctuations; that is, $\partial_{y'} = 0$.

Given the specified background and perturbations—and assuming an inviscid, incompressible, and Boussinesq flow—the linearized wave-frame equations for momentum, buoyancy, and mass are

$$u'_t + U'u'_{x'} + wU'_z - fv' + p_{x'} = 0 \qquad \text{(C.1a)}$$

$$v'_t + U'v'_{x'} + wV'_z + fu' = 0 \qquad \text{(C.1b)}$$

$$w_t + U'w_{x'} + p_z - b = 0 \qquad \text{(C.1c)}$$

$$b_t + U'b_{x'} + u'fV'_z - v'fU'_z + wN^2 = 0 \qquad \text{(C.1d)}$$

$$u'_{x'} + w_z = 0 \qquad \text{(C.1e)}$$

with thermal wind and $B_z = N^2$ employed in the buoyancy equation.

C.2 Polarization Relations

By assumption, perturbations vary horizontally and temporally as $e^{i(\mathbf{k_h}\cdot\mathbf{x_h}-\omega t)}$, where $\mathbf{k_h} \equiv K\,\hat{\mathbf{x}}' = K\cos\varphi\,\hat{\mathbf{x}} + K\sin\varphi\,\hat{\mathbf{y}}$ (with $K > 0$), and with $\omega > 0$ the Eulerian frequency observed at a fixed location. The intrinsic frequency $\sigma = \omega - \mathbf{k_h}\cdot\mathbf{U}$ is that observed while moving with the background flow. Note that $\sigma_z = -U_z K\cos\varphi$ and that $(\partial_t + \mathbf{U}\cdot\nabla_\mathbf{h}) = -i\sigma$ when applied to perturbations. Here, $\nabla_\mathbf{h} \equiv \hat{\mathbf{x}}\,\partial_x + \hat{\mathbf{y}}\,\partial_y = \hat{\mathbf{x}}'\,\partial_{x'} + \hat{\mathbf{y}}'\,\partial_{y'}$ is the horizontal gradient operator. A necessity for internal waves is that $|f| \le \sigma \le N$; equivalently, $|\gamma_f| \le 1$ and $\gamma_N \le 1$ where $\gamma_f \equiv f/\sigma$ and $\gamma_N \equiv \sigma/N$ and with $\sigma > 0$ by convention.

Manipulation of the wave-frame equations yields the polarization relations

$$u' = \frac{i}{K}\, w_z \tag{C.2a}$$

$$v' = \frac{i\, U_z \sin\varphi}{\sigma}\, w + \frac{\gamma_f}{K}\, w_z \tag{C.2b}$$

$$p = \frac{U_z}{K}\,(i\cos\varphi + \gamma_f \sin\varphi)\, w + i\,\frac{\sigma^2 - f^2}{\sigma\, K^2}\, w_z \tag{C.2c}$$

$$b = -\frac{1}{\sigma}\,(\gamma_f\, U_z^2 \sin\varphi\cos\varphi + i\, N^2)\, w + \gamma_f\,\frac{U_z}{K}\,(-\sin\varphi + i\,\gamma_f\cos\varphi)\, w_z \tag{C.2d}$$

where the first, which follows from (C.1e), is substituted into (C.1b) to give the second. The first two are substituted into (C.1a) to yield the third, and into (C.1d) to produce the fourth. For the flow frame

$$u = -\frac{i\, U_z \sin^2\varphi}{\sigma}\, w + \frac{i\cos\varphi - \gamma_f \sin\varphi}{K}\, w_z \tag{C.3a}$$

$$v = \frac{i\, U_z \sin\varphi\cos\varphi}{\sigma}\, w + \frac{i\sin\varphi + \gamma_f\cos\varphi}{K}\, w_z \tag{C.3b}$$

are the polarizations for horizontal velocity.

Away from influences of turning levels and critical levels in the background shear, a freely propagating wave is assumed to conform to

$$w = \alpha(z)\, \hat{W}(\omega, \mathbf{k_h})\, e^{i(\mathbf{k_h}\cdot\mathbf{x_h} - \omega t)} \tag{C.4}$$

with complex amplitude $\hat{W}(\omega, \mathbf{k_h})$. If the vertical structure $\alpha(z)$ comprises at least a few oscillations before propagation is disrupted, then searching for phase relations is reasonable. If $\alpha_z(z)$ can be cast simply in terms of $\alpha(z)$, then the polarizations can be reduced to complex-valued, algebraic expressions that relate, to one another, the vertical structures of u', v', u, v, b and w occuring

instantaneously beneath a fixed location.

C.3 Vertical Structure Equation

Substitution of (C.2c) and (C.2d) into (C.1c) and isolation of the vertical structure described by (C.4) yields

$$\alpha_{zz} + M_1(z)\,\alpha_z + M_0(z)\,\alpha = 0 \tag{C.5}$$

where

$$\begin{aligned} M_1(z) &= -\frac{2\,NK}{\sigma}\,\frac{\mathrm{Fr}\,\gamma_f\,(\gamma_f\cos\varphi - i\sin\varphi)}{(1-\gamma_f^2)}\,, \\ M_0(z) &= \frac{N^2K^2}{\sigma^2}\,\frac{(1-\gamma_N^2)}{(1-\gamma_f^2)} + \frac{NK}{\sigma}\,\frac{U_{zz}\,(\cos\varphi - i\,\gamma_f\,\sin\varphi)}{N\,(1-\gamma_f^2)} \\ &\quad -\frac{i\,2\,N^2K^2}{\sigma^2}\,\frac{\mathrm{Fr}^2\,\gamma_f\,\cos\varphi\sin\varphi}{(1-\gamma_f^2)} \end{aligned}$$

for $\mathrm{Fr} \equiv U_z/N$ as the Froude number of the background flow. Near the equator (where $f = 0$) or for high frequencies (where $|\gamma_f| \ll 1$), this reduces to the Taylor-Goldstein equation 8 of *Eriksen* [1985].

For the case of $\mathrm{Fr} = 0$, the WKB solution

$$\alpha(z) = \alpha_0\, m^{-1/2}\, e^{i\int^z m(s)ds} \tag{C.6}$$

approximately satisfies (C.5), where the dispersion relation

$$m^2 = \frac{N^2K^2}{\sigma^2}\,\frac{(1-\gamma_N^2)}{(1-\gamma_f^2)} \tag{C.7}$$

is that for a uniform flow. Given certain restrictions, (C.6) and (C.7) are adequate in modeling the low order kinematics associated with a sheared background flow:

For $|\gamma_f \mathrm{Fr}| \ll 1$, $|\mathrm{Fr}| < 1$ and $\gamma_N^2 \ll 1$, $M_1(z)$ and the last term of $M_0(z)$ can be neglected—near-inertial waves in moderately strong shear and non-hydrostatic waves violate these conditions. As $U_{zz} \to 0$, the middle term of $M_0(z)$ vanishes. Furthermore, if N and Fr are also essentially constant over the analysis region, then vertical wavenumber m can be taken as constant. Under the above assumptions, a general solution to (C.5) is

$$\alpha(z) = A_{\mathrm{up}}\, e^{imz} + A_{\mathrm{down}}\, e^{-imz} \tag{C.8}$$

where A_{up} and A_{down} are complex constants and $m > 0$ conforms to (C.7). Vertical velocity for a wave with upward phase propagation is specified by substituting (C.8) into (C.4) with $A_{\mathrm{up}} = 1$ and $A_{\mathrm{down}} = 0$; for a wave with downward phase propagation, $A_{\mathrm{up}} = 0$ and $A_{\mathrm{down}} = 1$. Note that upward propagators have $\alpha_z = im\alpha$ while downward have $\alpha_z = -im\alpha$. The polarization relations can now be evaluated to form combinations of wave variables according to the following conventions.

C.4 Cross Spectra

Cross spectra computed on profile measurements sometimes reveal coherences among horizontal velocity components and density fluctuations. To evaluate whether such coherences could be attributed to propagating internal waves, one must understand how the spectral processing views the modeled perturbations. Particular attention must be paid to phase conventions. Consider the profiles $a(z)$ and $c(z)$ in Figure C.2. The sense of phase in such instantaneous records is ambiguous, because $\cos(-mz) = \cos(mz)$. To follow the downward-looking orientation of oceanography, the convention here is to perceive phase increasing with depth, thereby dictating that $a(z) = a_0 \cos(-mz)$ since $m > 0$ (i.e., $-mz \to$

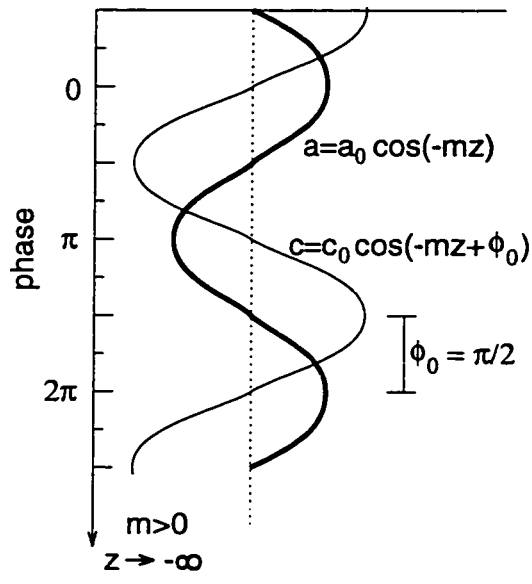

Figure C.2: Definition diagram for cross-spectral phase and amplitude. By convention, phase is interpreted as increasing downward, so $c(z)$ is seen as leading $a(z)$ by $\phi_0 = \pi/2$. Wavenumber m and amplitudes a_0 and c_0 are real and positive, and $z \to -\infty$ with depth.

∞ as $z \to -\infty$). The phase offset between records, designated ϕ_0, is restricted to $-\pi < \phi_0 \leq \pi$. Hence, in the pictured example, $c(z) = c_0 \cos(-mz+\phi_0)$ leads $a(z)$ by $\phi_0 = \pi/2$. Integrating with increasing depth $\zeta = -z$ down to $\zeta = D$ via

$$\hat{c}(m) = \frac{1}{D}\int_0^D c(z)e^{im\zeta}d\zeta = \frac{1}{D}\int_{-D}^0 c(z)e^{-imz}dz = \frac{c_0}{2}e^{-i\phi_0}$$

yields Fourier coefficients for each discrete $m = n\pi/D > 0$. We introduce the cross-spectral quantity

$$H_{ca}(m) \equiv \frac{\hat{a}(m)}{\hat{c}(m)} = \frac{a_0}{c_0}e^{i\phi_0}$$

to describe the amplitude and phase relation of c to a.

Now, assume that a vertically propagating wave is the cause of measured fluctuations a and c. Either an upward-phased wave with variables conforming to

$$a_{\mathrm{u}} = a_0 e^{imz}, \quad c_{\mathrm{u}} = c_0 e^{-i\phi_0} e^{imz}$$

or a downward wave with

$$a_{\mathrm{d}} = a_0 e^{-imz}, \quad c_{\mathrm{d}} = c_0 e^{i\phi_0} e^{-imz}$$

would correspond to the observations in Figure C.2 (e.g., $c = \Re(c_{\mathrm{u}}) = \Re(c_{\mathrm{d}})$). To recover the observed cross-spectral relation H_{ca} from the model variables, the downward case must be treated differently from the upward case. Thus, two forms

$$H_{ca}^{+} = \frac{a_{\mathrm{u}}}{c_{\mathrm{u}}} \quad \text{and} \quad H_{ca}^{-} = \frac{a_{\mathrm{d}}^{*}}{c_{\mathrm{d}}^{*}} \tag{C.9}$$

are defined, with complex conjugates employed for the latter. Both yield the required result, as $\mathrm{mod}(H_{ca}^{\pm}) = a_0/c_0$ and $\arg(H_{ca}^{\pm}) = \phi_0$. This methodology of combining wave variables to anticipate measurement cross spectra is applicable beyond the simple illustrative example. For generic variables a, c and d, $H_{cd}^{\pm} = H_{ca}^{\pm} H_{ad}^{\pm} = (H_{dc}^{\pm})^{-1}$ and, in general, $H_{cd}^{+} \neq H_{cd}^{-}$.

Expressions are formed to interpret coherences among observed profiles of velocity and density. Substitution of $w_z = \pm imw$ into (C.2a), (C.2b) and (C.2d), and subsequent simplification according to (C.9), yields relations $H_{u'v'}^{\pm}$, $H_{u'b}^{\pm}$ and $H_{v'b}^{\pm}$. To model cross spectra involving vertical displacement η, the relation $H_{b\eta}^{\pm}$ is needed to form $H_{u'\eta}^{\pm} = H_{u'b}^{\pm} H_{b\eta}^{\pm}$ and $H_{v'\eta}^{\pm} = H_{v'b}^{\pm} H_{b\eta}^{\pm}$. Typically, η is estimated by measuring deviations of a scalar property from its mean profile, as

in

$$\eta = \frac{-b}{B_z} \;=\; \frac{-b}{N^2}\,; \tag{C.10}$$

however, advection of mean horizontal variations can also contribute to this measurement. Determination of η_L—the actual displacement of a water parcel from its mean vertical position—requires a Lagrangian measurement, a task not suited to vertical profilers or moored instruments. Therefore, measured displacements are modeled by (C.10), which implies $H^{\pm}_{b\eta} = -N^{-2}$. In certain cases, η_L should be used when analyzing energetics. Note that $w = (\partial_t + \mathbf{U}\cdot\nabla_{\mathbf{h}})\eta_L = -i\sigma\eta_L$ and so $H^{\pm}_{w\eta_L} = \pm i/\sigma$.

Several of the following expressions contain the wave Burger number, Br $= NK/fm$; its variation with frequency is shown in Figure C.3 for $f > 0$ in the northern hemisphere. Other parameters previously defined are $\gamma_f = f/\sigma$, $\gamma_N =$

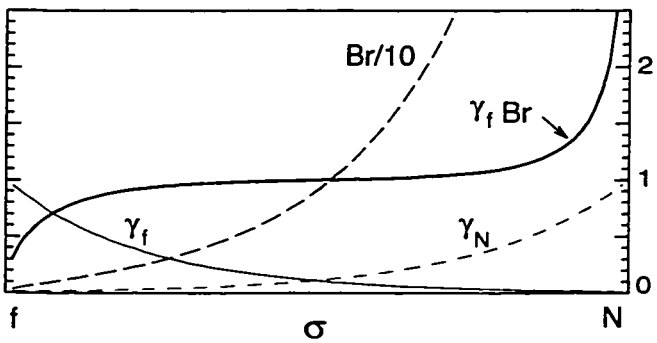

Figure C.3: Variation of Br $= NK/fm$ and γ_fBr with intrinsic frequency σ, assuming dispersion relation (C.7) with $N/f = 80$. To center and highlight the continuum band, σ is plotted logarithmically; its value is $\gamma_f^{-1} f$ or $\gamma_N N$.

σ/N, Fr $= U_z/N$ and positive wavenumbers K and m.

Results from the wave-frame polarizations include

$$H^{\pm}_{u'v'} \;=\; \mp i\,\gamma_f\,(1 \pm \mathrm{BrFr}\sin\varphi) \tag{C.11a}$$

$$H^{\pm}_{\hat{w}\eta} = N^{-1}\left[-\gamma_f^2\,\mathrm{Fr}\cos\varphi\,(1 \pm \mathrm{BrFr}\sin\varphi) - i\,\gamma_f\,(\mathrm{Br} \pm \mathrm{Fr}\sin\varphi)\right] \quad \text{(C.11b)}$$

$$H^{\pm}_{\hat{w}\eta} = N^{-1}\left[\pm\left(\frac{\mathrm{Br} \pm \mathrm{Fr}\sin\varphi}{1 \pm \mathrm{BrFr}\sin\varphi}\right) \mp i\,\gamma_f\,\mathrm{Fr}\cos\varphi\right] \quad \text{(C.11c)}$$

$$H^{\pm}_{\hat{w}w} = \mp\frac{K}{m}\,. \quad \text{(C.11d)}$$

These can be simplified for continuum frequencies, $|f| \ll \sigma \ll N$, for which

$$\gamma_f\,\mathrm{Br} = \frac{NK}{\sigma m} \approx 1$$

follows from (C.7). As Figure C.3 shows, given $f = \pm 6.6 \times 10^{-5}$ s^{-1} and $N = 5.3 \times 10^{-3}$ s^{-1}, γ_fBr ranges from 0.9 at $\gamma_f = \pm 0.45$ ($\sigma = \pm 2.2f$) to 1.1 at $\gamma_N = 0.40$ ($\sigma = N/2.5$). For this frequency range

$$H^{\pm}_{\hat{w}v'} = \mp i\,(\gamma_f \pm \mathrm{Fr}\sin\varphi) \quad \text{(C.12a)}$$

$$H^{\pm}_{\hat{w}\eta} = N^{-1}\left[-\gamma_f\,\mathrm{Fr}\cos\varphi\,(\gamma_f \pm \mathrm{Fr}\sin\varphi) - i\,(1 \pm \gamma_f\,\mathrm{Fr}\sin\varphi)\right] \quad \text{(C.12b)}$$

$$H^{\pm}_{v'\eta} = N^{-1}\left[\pm\left(\frac{1 \pm \gamma_f\,\mathrm{Fr}\sin\varphi}{\gamma_f \pm \mathrm{Fr}\sin\varphi}\right) \mp i\,\gamma_f\,\mathrm{Fr}\cos\varphi\right] \quad \text{(C.12c)}$$

are the approximate forms of (C.11a)–(C.11c). Combining these expressions with

$$H^{\pm}_{uu'} = (\cos\varphi - H^{\pm}_{\hat{w}v'}\sin\varphi)^{-1} \quad \text{or} \quad H^{\pm}_{vu'} = (\sin\varphi + H^{\pm}_{u'v'}\cos\varphi)^{-1}$$

yield flow-frame relations $H^{\pm}_{uv} = H^{\pm}_{uu'}/H^{\pm}_{vu'}$, $H^{\pm}_{u\eta} = H^{\pm}_{uu'}H^{\pm}_{u'\eta}$ and $H^{\pm}_{v\eta} = H^{\pm}_{vu'}H^{\pm}_{u'\eta}$.

C.5 Velocity Ellipses

Influences of mean-shear strength and wave frequency and orientation are illustrated by the current ellipses in Figure C.4. Each is determined for given Fr,

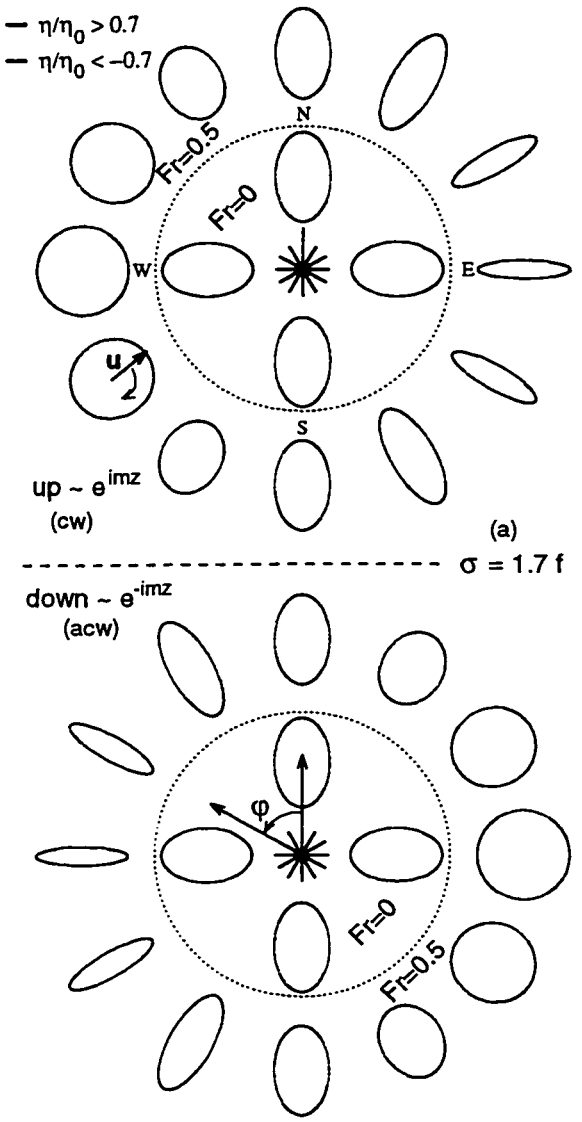

Figure C.4: Ellipses showing progression with depth of perturbation velocity vector. Extrema of displacement (green=up, red=down) show phase relations to velocity. Ellipse positioning indicates wavevector azimuth. Inner ellipses are for the no-shear case (Fr = 0), outer are for Fr = 0.5 (with flow toward the top of the page, labeled 'N' for Florida Current comparison). Northern-hemisphere behavior for both upward and downward phase propagation is displayed for three frequencies: (a) $\sigma = 1.7f$ ($\gamma_f = 0.6$); (b) $\sigma = 3.3f$ ($\gamma_f = 0.3$); (c) $\sigma = 10f$ ($\gamma_f = 0.1$). Dashed lines enclose ellipses that rotate opposite the default clockwise for upward and anticlockwise for downward phase.

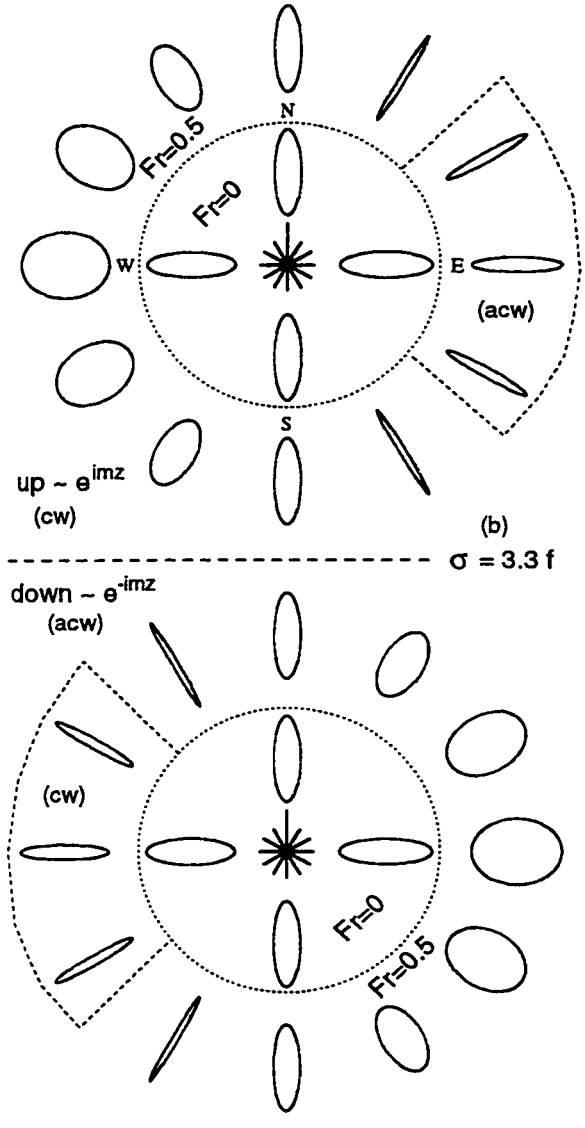

Figure C.4: (b) Ellipses for $\sigma = 3.3f$ ($\gamma_f = 0.3$).

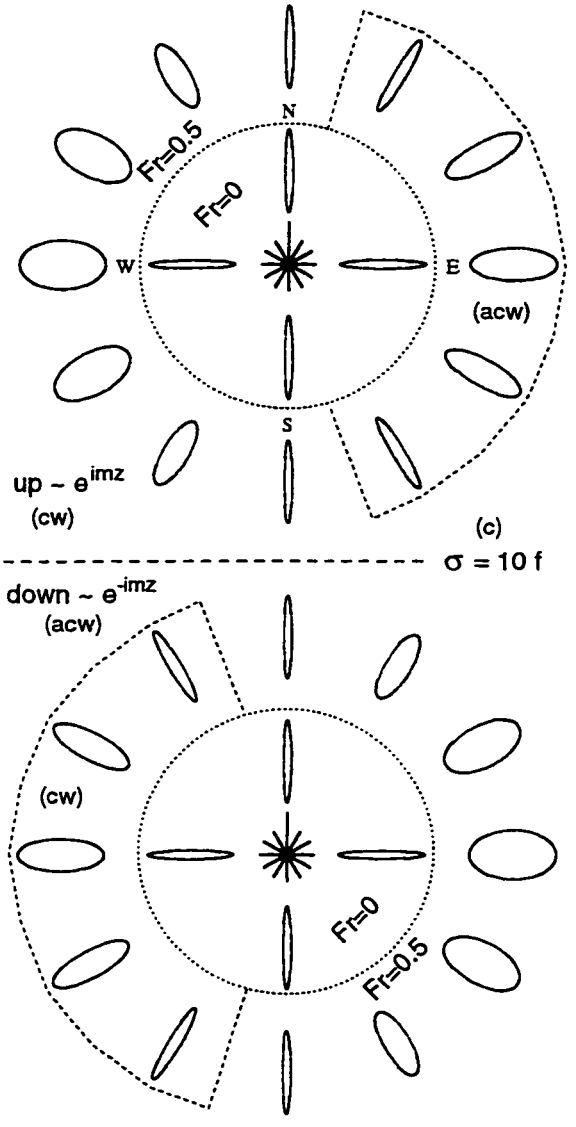

Figure C.4: (c) Ellipses for $\sigma = 10f$ ($\gamma_f = 0.1$).

γ_f and φ by applying phase and amplitude relations computed from $H^{\pm}_{u\eta}$ and $H^{\pm}_{v\eta}$ to a specified displacement profile, $\eta = \eta_0 \cos(-mz)$, and following the depth progression of the resulting perturbation velocity vector. Northern-hemisphere behavior is shown, with default rotations being clockwise for upward-phased and anticlockwise for downward-phased waves—ellipses for the southern hemisphere are identical to their northern counterparts of opposite vertical phase (i.e., $H^{\pm}(\mathrm{Fr}, \varphi, \sigma, f<0) = H^{\mp}(\mathrm{Fr}, \varphi, \sigma, |f|)$ for (C.11a)–(C.11c)).

For a background without mean flow or shear, any horizontal reference can be chosen for the flow direction. Evident in the ellipses computed with $\mathrm{Fr}=0$ is the diminishing amplitude of cross-wave velocity, v', with increasing frequency. Displacement, η, is in phase with along-flow velocity, u, for upward-phased waves propagating cross-flow to the right, and 180° out of phase for those to the left; the converse occurs for downward-phased waves. Note that displacement leads along-wave velocity, u', by 90°, regardless of azimuth or phase direction. This conflicts with the up-down comparison in Figure 9 of *Johnson and Sanford* [1980].

An additional along-flow perturbation is produced when background shear is distorted by internal wave displacements. The relative contribution of this component depends on Fr and wave frequency and direction. Rotary polarization is enhanced in some cases, diminished in others, and even reversed for combinations of strong shear and higher frequencies. For upward phase propagation

$$u^{+}_{\mathrm{cw}} = 2^{-1/2}(u' + iv') \quad \text{and} \quad u^{+}_{\mathrm{acw}} = 2^{-1/2}(u' - iv')$$

rotate clockwise and anticlockwise with depth, while for downward phase

$$u^{-}_{\mathrm{cw}} = 2^{-1/2}(u'^{*} + iv'^{*}) \quad \text{and} \quad u^{-}_{\mathrm{acw}} = 2^{-1/2}(u'^{*} - iv'^{*})$$

behave accordingly. Ratios of amplitudes for the two cases are

$$\frac{|u^+_{cw}|}{|u^+_{acw}|} = \left|\frac{1 + \gamma_f(1 + \mathrm{BrFr}\sin\varphi)}{1 - \gamma_f(1 + \mathrm{BrFr}\sin\varphi)}\right| \approx \left|\frac{1 + (\gamma_f + \mathrm{Fr}\sin\varphi)}{1 - (\gamma_f + \mathrm{Fr}\sin\varphi)}\right| \quad \text{(C.13a)}$$

$$\frac{|u^-_{cw}|}{|u^-_{acw}|} = \left|\frac{1 - \gamma_f(1 - \mathrm{BrFr}\sin\varphi)}{1 + \gamma_f(1 - \mathrm{BrFr}\sin\varphi)}\right| \approx \left|\frac{1 - (\gamma_f - \mathrm{Fr}\sin\varphi)}{1 + (\gamma_f - \mathrm{Fr}\sin\varphi)}\right| \quad \text{(C.13b)}$$

where the approximate forms on the right are valid if $|\gamma_f| < 0.45$ and $\gamma_N < 0.40$. The rotary amplitudes are invariant with respect to horizontal coordinates: (C.13a) and (C.13b) result even if flow-frame velocities u and v replace u' and v' in the component definitions. These relations are consistent with previous results for $\mathrm{Fr}=0$, including rotary ratios for time series in *Mooers* [1973] and for downward-phased fluctuations in *Johnson and Sanford* [1980].

The competition between internal-wave fluctuation and mean-shear distortion is reflected in the recurring terms $(\gamma_f \pm \mathrm{Fr}\sin\varphi)$. When $|\gamma_f| + |\mathrm{Fr}| > 1$, polarity increases until perturbation orbits are circular at azimuths with $\sin\varphi = \pm(1 - \gamma_f)/\mathrm{Fr}$, between which $H^{\pm}_{u'v'}$ reveals that cross-wave amplitudes exceed along-wave. With $\mathrm{Fr} = 0.5$ and near-inertial $\gamma_f = 0.6$ in Figure C.4a, this effect occurs at $\varphi = \pm(90 \pm 37)°$. (Shear-affected ellipses are sized to match their no-shear counterparts in cross-flow amplitude, $|u|$.) Ellipses become less polarized approaching the opposite normal azimuth, but do not achieve reversed rotation unless $|\mathrm{Fr}| > |\gamma_f|$. In such a case, reversals occur for azimuths between rectilinear boundaries at $\sin\varphi = \mp\gamma_f/\mathrm{Fr}$. Figures C.4b,c exhibit the broadening of this region with increasing frequency, from $\varphi = \mp(90 \pm 53)°$ for $\sigma = 3.3f$ out to $\mp(90 \pm 78)°$ at $10f$. Broadening with increasing Fr is also implied. Notice that the reversed ellipses at a given azimuth match those of oppositive vertical phase in their sense of rotation—though with less polarization—and their relation to displacement. Regarding lower frequency waves aligned near to the flow,

mean-shear distortion alters the η-u' phase relation, although horizontal advection of density fluctuations also plays an appreciable role at this extreme where the dispersion-relation restriction $|\gamma_f \mathrm{Fr}| \ll 1$ is questionable.

Relations among internal-wave Froude components, u_z/N and v_z/N, and vertical strain, η_z, correspond to those of N-scaled velocity (u/N, v/N) and displacement, assuming that m is essentially constant over the analysis region.

For typical conventions, time-series fluctuations should follow the interpretations given here for upward vertical phase. Some consequences of the mean-flow perturbation on equatorial mooring measurements are discussed in *Eriksen* [1985], *Boyd et al.* [1993], and *Lien et al.* [1996].

To extend the analysis from the single-wave case, all waves at a given vertical wavenumber must be combined to form cross spectra. This can be done by supplying complex amplitudes via (C.4) to the polarization relations over a spectrum of frequencies, azimuths and vertical directions. Upward wave variables must be summed with conjugates of the downward ones before computing the relation, e.g.,

$$H_{\Sigma u \Sigma \eta} = \frac{\sum u_{\mathrm{up}} + \sum u^*_{\mathrm{down}}}{\sum \eta_{\mathrm{up}} + \sum \eta^*_{\mathrm{down}}}$$

between a given pair [compare *Blumenthal and Briscoe*, 1995]. In their integration, *Johnson and Sanford* [1980] missed this subtlety. Although variables in *Eriksen* [1985] were summed over vertical wavenumber rather than frequency, certain conclusions regarding horizontal kinetic energy components and current-temperature coherence at a mooring apply to profile measurements as well.

VITA

David P. Winkel

Born 12 October 1955, Columbus, Georgia

Education

B.S. 1976, University of Washington, Mathematics

M.S. 1990, University of Washington, Oceanography

Ph.D. 1998, University of Washington, Oceanography

Publications

Winkel, D. P., M. C. Gregg, and T. B. Sanford, 1992: Simultaneous observations of shear and turbulence in the Florida Current, in *Proceedings of the Tenth Symposium on Turbulence and Diffusion, Sep. 29 – Oct. 2, 1992, Portland, Oregon*, pp. (J5)101–104, AMS, Boston.

Gregg, M. C., D. P. Winkel, and T. B. Sanford, 1993: Varieties of fully resolved spectra of vertical shear, *J. Phys. Oceanogr.*, **23**, 124–141.

Winkel, D. P., M. C. Gregg, B. M. Bell, and T. B. Sanford, 1994: Resolving velocity profiles with the Multi-Scale Profiler, Technical Report APL-UW TR 9414, Appl. Phys. Lab., Univ. of Wash., 80 pp.

Winkel, D. P., M. C. Gregg, and T. B. Sanford, 1996: Resolving oceanic shear and velocity with the Multi-Scale Profiler, *J. Atmos. Ocean. Tech.*, **13**, 1046–1072.

IMAGE EVALUATION TEST TARGET (QA-3)

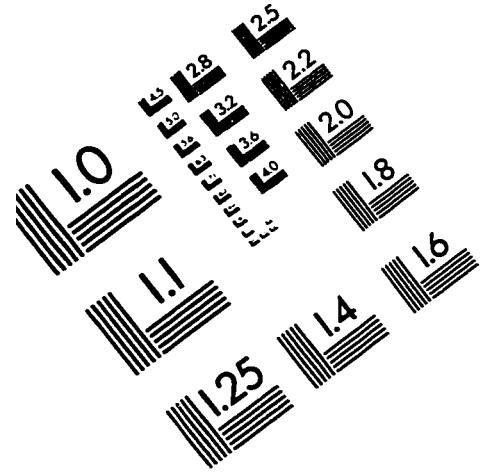

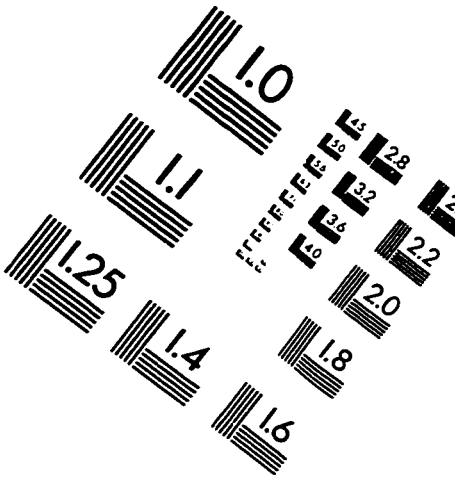

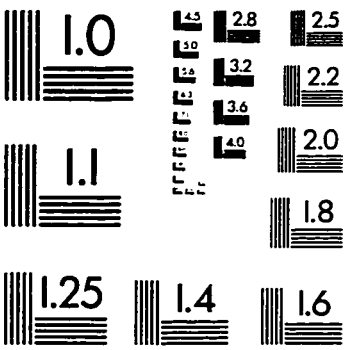

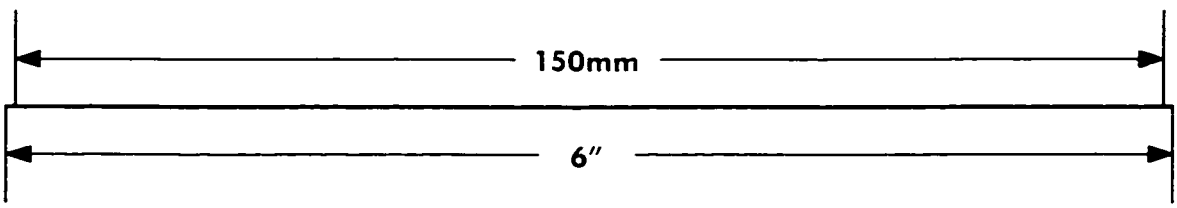

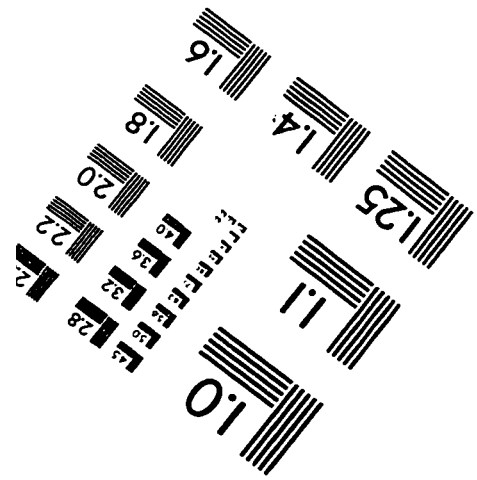

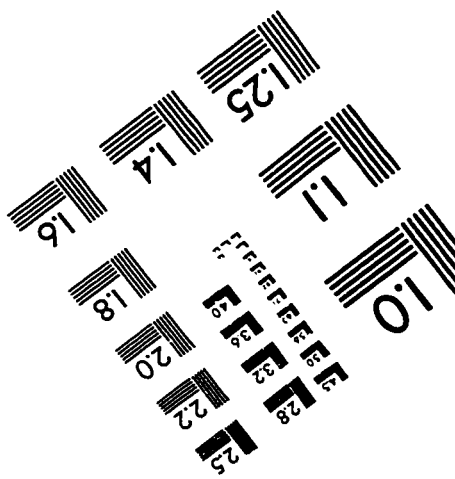

APPLIED IMAGE, Inc
1653 East Main Street
Rochester, NY 14609 USA
Phone: 716/482-0300
Fax: 716/288-5989